Silicon and phosphorus co-implantation into undoped and indium-doped GaAs substrates

N. N. Dymova

P. N. Lebedev Physical Institute, Russian Academy of Sciences, 117924 Moscow, Russia

A. E. Kunitsyn and V. V. Chaldyshev

A. F. Ioffe Physicotechnical Institute, Russian Academy of Sciences, 194021 St. Petersburg, Russia

A. V. Markov

State Institute of Rare Metals, 109017 Moscow, Russia

(Submitted June 24, 1997; accepted for publication July 14, 1997)
Fiz. Tekh. Poluprovodn. **31**, 1409–1413 (December 1997)

The electrical properties and low-temperature (4.2 K) photoluminescence of heavily doped *n*-type layers produced by silicon and silicon/phosphorus implantation into undoped and indium-doped Czochralski grown semi-insulating GaAs substrates have been investigated. It is found that Si+P co-implantation results in suppression of deep levels in the anion sublattice, an increase of donor activation efficiency, and a sharper carrier concentration profile in both types of substrates. The use of indium-doped substrates enhances radiation defect annealing, but does not change the donor activation efficiency. © *1997 American Institute of Physics.* [S1063-7826(97)00112-9]

1. INTRODUCTION

At present, ion implantation is widely used in the production of semiconductor devices. In particular, it is used to create layers with enhanced charge-carrier concentration, of both types, which are necessary for the fabrication of field-effect transistors and integrated microcircuits for various applications. The problem of obtaining layers with the maximum possible electron concentration cannot be solved simply by increasing the dose of the implanted impurity for a number of reasons. Increases in the implantation dose are accompanied by an increase in the number of radiation defects, and to anneal out these defects requires a more severe heat treatment, which is undesirable, in particular, because of the resulting deterioration of the dopant impurity profile and the additional complication of the technology of preparing high-quality layers. In the case of devices created on gallium-arsenide substrates, note should also be made of the possibility of introducing the implanted atoms into sublattices of both types. This problem is all the more urgent since the impurity most widely used to form *n*-type conductivity layers in GaAs by ion implantation is silicon, which has a low diffusion coefficient in GaAs and comparatively low atomic weight. At higher implantation dose levels, this group-IV element builds itself into not only the gallium sublattice (as the Si_{Ga} donor), but also into the arsenic sublattice (as the Si_{As} acceptor), thereby lowering the donor activation efficiency due to self-compensation. Besides, larger doses of silicon lead to the formation of deep levels in the anion sublattice at which silicon is bound with the intrinsic lattice defects.

Previously,[1,2] it was shown that co-implantation of the isovalent impurity P, together with the electrically active impurity Si in GaAs, leads to an increase in the donor activation efficiency. It is also known that introducing a small quantity of the isovalent impurity In enables one to obtain GaAs single crystals with a low dislocation density by the Czochralski method,[3] and when growing epitaxial layers leads to a decrease in the concentration of deep levels.[4,5]

In the present paper we analyze the results of the combined use of these two isovalent impurities to obtain strongly doped layers with *n*-type conductivity by means of double implantation of Si+P into indium-doped substrates of semi-insulating gallium arsenide grown by the Czochralski method. A comparison is made of the experimental data on implantation of Si and Si+P into GaAs (In) substrates and undoped GaAs substrates.

2. EXPERIMENT

Undoped and indium-doped substrates of semi-insulating GaAs(100) with thickness 300 μm and diameter 40 mm were cut from single crystals grown by the Czochralski method with liquid hermetization. The resistivity of the substrates was 4.5×10^8 and 2.4×10^7 $\Omega\cdot$cm, respectively.

The process of ion implantation was carried out at room temperature using $^{30}Si^+$ and $^{31}P^+$ ions with energies of 20, 50, and 125 keV. Thus, in order to obtain a homogeneously doped layer of 0.1 μm thickness, the impurity concentration was varied from 2.2×10^{13} to 1.6×10^{14} cm^{-2} for silicon and 1.1×10^{14} to 1.6×10^{14} cm^{-2} for phosphorus. The layers were subsequently annealed at 850 °C for 15 min in an atmosphere of hydrogen under a protective layer of Si_3N_4 of

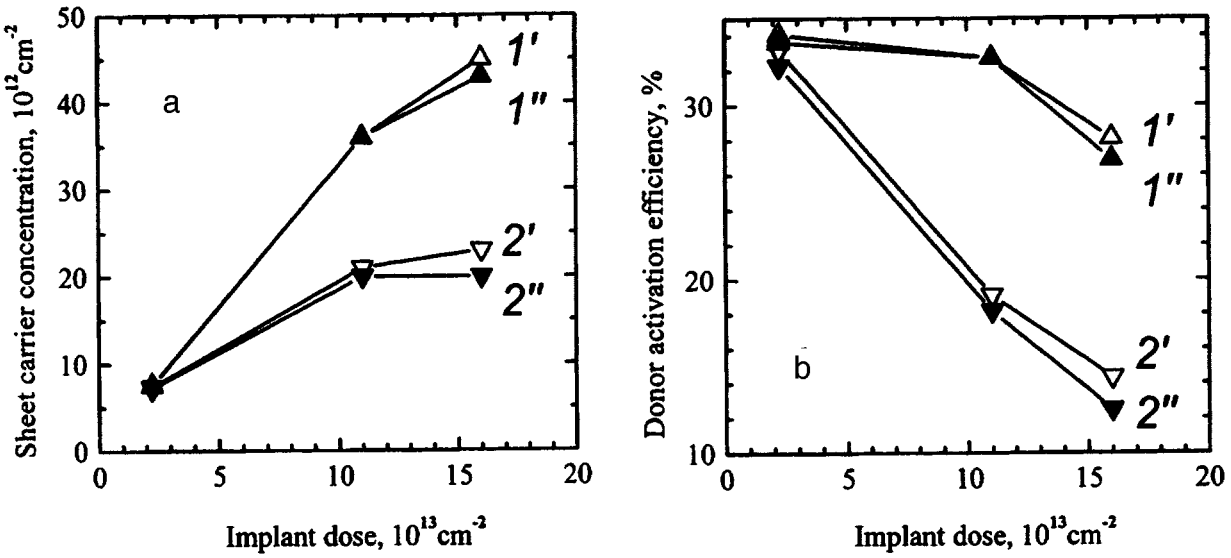

FIG. 1. Dependence of the sheet electron concentration (a) and donor activation efficiency (b) on the silicon implant dose. *1′,1″*—samples implanted with Si+P; *2′,2″*—samples implanted only with Si. Type of substrate: *1′,2′*—doped; *1″,2″*—undoped.

thickness 0.12 μm deposited on GaAs wafers pyrolytically at 700 °C.

To investigate the layers obtained as indicated above, we used low-temperature photoluminescence and electrical measurements. Measurements of the mobility and charge carrier concentration were carried out by the van der Pauw method at temperatures of 77–300 K. Profiles of the charge-carrier distribution were obtained by measuring the current–voltage characteristics employing layered etching of the samples. The photoluminescence studies were performed at 4.2 K in the spectral range 800–1200 nm. Excitation was produced by an argon laser (wavelength 514.5 nm), and an FÉU-62 cooled photomultiplier was used to record the signal.

3. RESULTS

Figure 1 shows the sheet carrier concentration (a) and donor activation efficiency (b) for all the samples as functions of the silicon implant dose. It can be seen that in all cases increasing the dose of the electrically active impurity leads to a decrease of the donor activation efficiency. However, at large doses co-implantation of silicon and phosphorus leads to an increase of the donor activation efficiency (and, consequently, the sheet electron concentration) by a factor of 1.5–2 in comparison with implanting only silicon. It can also be seen that using different types of substrates (undoped and indium-doped) has hardly any effect on these parameters.

The electron mobility measurements showed that as one goes from small implantation doses to large ones the mobility decreases from 3100 to 1800 cm^2/(V·s) in samples grown on undoped substrates, and from 3250 to 2100 cm^2/(V·s) on indium-doped substrates. In comparison with implantation of only silicon ions, co-implantation of silicon and phosphorus had no adverse effect on the charge-carrier mobility, and in some cases it increased it by 30%. In other words, despite the increased concentration of nascent radiation defects, co-implantation of the electrically active impurity Si and the isovalent impurity P does not lead to a deterioration of the crystalline perfection of the layer. It should be noted that the nonequilibrium indium distribution over the GaAs (In) single crystal prevented us from carrying out a quantitative analysis of the obtained charge-carrier mobility data as a function of the impurity implantation dose. However, a comparison of the data for the GaAs:Si and GaAs:Si+P layers leads to qualitatively the same results.

Figure 2 shows a typical profile of the charge-carrier concentration with depth in the layer, obtained by measuring the current–voltage characteristics. It can be seen that in addition to a steeper profile of the electron concentration profile, co-implantation of silicon and phosphorus leads to an increase of the maximum carrier concentration by 20–50% in comparison with single implantation.

Figure 3a shows low-temperature photoluminescence

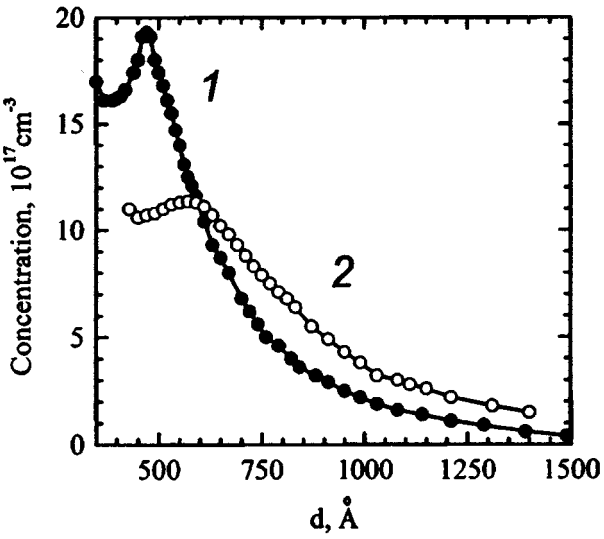

FIG. 2. Typical electron concentration profiles in GaAs:Si+P (*1*) and GaAs:Si (*2*).

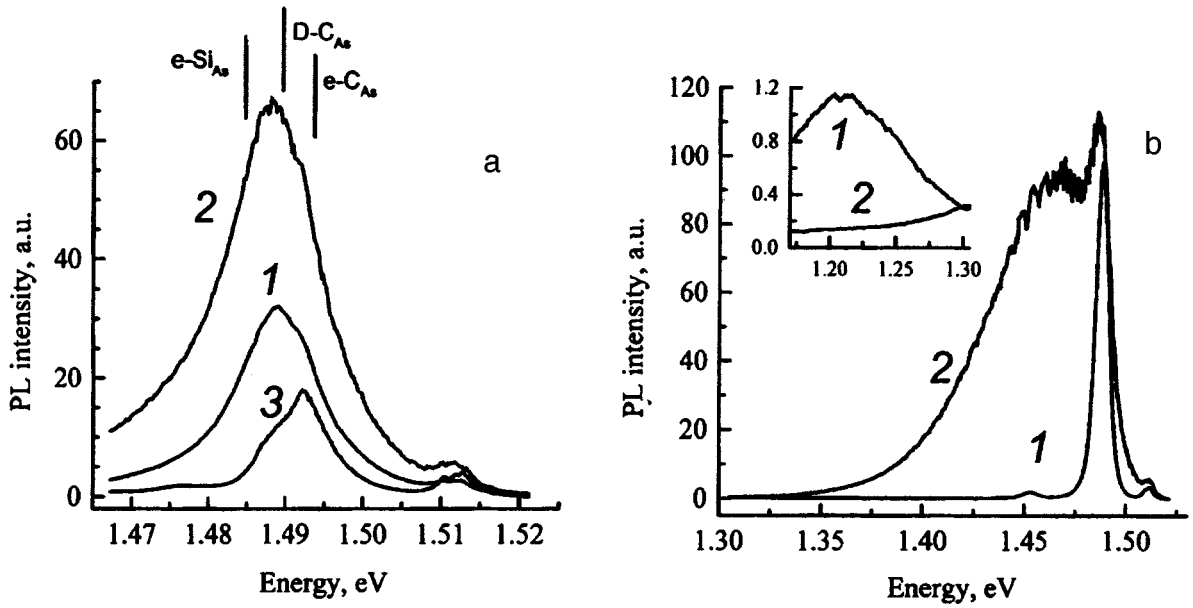

FIG. 3. Low-temperature (4.2 K) luminescence spectra of GaAs layers obtained by implantation of small (a) and large (b) doses of Si and Si+P into an undoped substrate: *1*—co-implantation, *2*—implantation of only silicon, *3*—spectrum of substrate.

spectra of samples implanted with Si and Si+P in the case of small doses of the implanted impurities. The photoluminescence spectrum of GaAs is also shown for comparison. Undoped GaAs revealed photoluminescence lines, which are associated with the interband transitions (1.512 eV), and also lines belonging to the transitions between the band and the shallow C and Ge acceptors (1.492 and 1.476 eV), accompanied by a series of phonon echoes.[6] In the case of single silicon implantation and in the case of co-implantation of Si+P the total photoluminescence intensity increases. This increase is more noticeable in the sample with single implantation. The intensity of the lines associated with the shallow acceptors is increased to a larger extent than that of the lines of the edge emission, but the maximum of the acceptor band is shifted toward longer wavelengths. While in the case of co-implantation this shift can be explained by an increase in the contribution of donor–acceptor recombination with participation of the background carbon acceptor, for single silicon implantation the greater shift of the acceptor band must be attributed to the appearance of lines associated with Si_{Ga} (Ref. 6). With increase of the dose of the implanted ions (Fig. 3b) in GaAs:Si an extraordinarily wide acceptor band with maximum at 1.45–1.47 eV, whose intensity grows with further increase of the implantation dose, appears in the spectrum. For the co-implanted samples instead of the band at 1.45–1.47 eV a weak wide line is observed in the region of

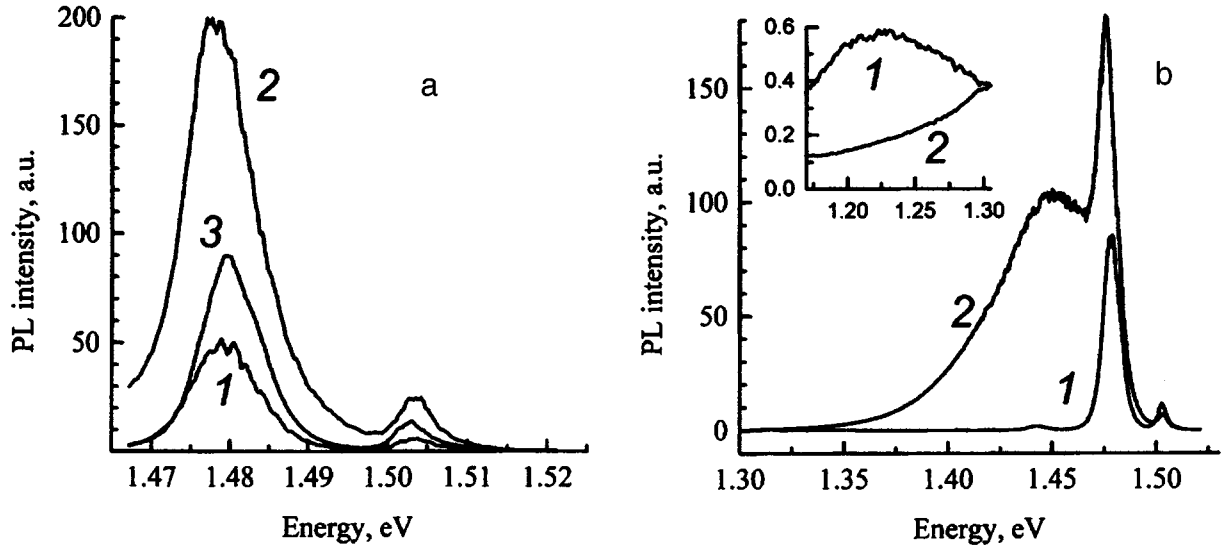

FIG. 4. Low-temperature (4.2 K) luminescence spectra of GaAs layers obtained by implantation of small (a) and large (b) doses of Si and Si+P into an indium-doped substrate: *1*—co-implantation, *2*—implantation of only silicon, *3*—spectrum of substrate.

1.2 eV, whose intensity also increases with increasing ion implantation dose.

Photoluminescence spectra of the samples prepared on the indium-doped substrates are shown in Fig. 4 for small (a) and large (b) doses. Changes caused by the difference in the implantation doses and in the choice of implanted ions have the same qualitative character as in the previous case. All lines are shifted toward longer wavelengths as a result of a decrease in the width of the band gap of the material due to the presence of indium. Note that the emission bands 1.45–1.47 eV [for GaAs (In):Si] or 1.2 eV [for GaAs (In):Si,P] are manifested at larger implantation doses than in the case of undoped substrates. The total photoluminescence intensity of samples grown on indium-doped substrates is higher at all implantation doses in comparison with samples prepared on undoped substrates. In addition, in the case of indium-doped substrates an increase of the contribution of donor–acceptor transitions is noted in comparison with the material prepared on undoped GaAs substrates.

4. DISCUSSION

The results of our study show that the effect of co-implantation of silicon and phosphorus is manifested in a similar way for samples prepared on undoped and indium-doped samples.

The photoluminescence studies showed that as the silicon implantation dose is increased, not only are Si_{Ga} donors formed in gallium arsenide, but also Si_{As} acceptors, as well as complexes responsible for the photoluminescence band centered at 1.45–1.47 eV. There is a general tendency to associate this photoluminescence band with the presence of Ga_{As}, $Ga_i - Si_{As}$, and V_{As}-Si_{As} defects in the anion sublattice.[2] In the case of co-implantation of Si+P these defects disappear, while deep centers which are associated with the V_{Ga}-Si_{Ga} complex, appear in the cation sublattice, leading to the appearance of the 1.2-eV photoluminescence line.[7] The reason for this effect may be a deviation from stoichiometry, which is caused by the ions of the isovalent impurity P and which leads to a group-V element excess and a redistribution of the amphoteric impurity Si toward a preferential creation of donor states at the gallium sites. This hypothesis is confirmed by measurements of the sheet electron concentration.

The use of indium-doped GaAs substrates leads to the suppression of deep defects formed during ion implantation. Thus, the photoluminescence studies showed that the emission bands associated with the Ga_{As}, $Ga_i - Si_{As}$, and V_{As}-Si_{As} defects in the case of single silicon implantation and with the complex V_{Ga}-Si_{Ga} in the case of co-implantation are manifested only at maximal doses of the implanted impurities. A similar phenomenon was observed earlier in epitaxial indium-doped GaAs films obtained by various methods.[4,5] It is known that indium impurity in GaAs is not electrically active. However, local lattice strains created by the indium atoms can act on such point defects as vacancies, interstitials, etc. Here the indium atoms can act on the centers of mutual annihilation of Frenkel pairs, thereby preventing the formation of complexes of the intrinsic lattice defects and silicon.

This effect should lead to an improvement of the quality of the crystal lattice and to an increase of the charge-carrier lifetime, as is confirmed by an increase in the intensity of the photoluminescence edge emission. It might be expected that a decrease in the number of nascent complexes will lead to an increase in the donor activation efficiency; however, typical values of the deep center concentrations are much lower than the silicon donor concentration and, consequently, the sheet electron concentration in the case of undoped and indium-doped substrates is nearly identical.

5. CONCLUSIONS

Experimental studies of the electrical properties of low-temperature photoluminescence of *n*-type layers, which were obtained by implanting silicon ions and silicon along with phosphorus into undoped and indium-doped, semi-insulating GaAs substrates, have shown that co-implantation increases the degree of activation of donors and provides a more sharply defined distribution profile of the dopant at high levels of implantation for both types of substrate. We found that co-implantation suppresses the formation of deep levels in the anion sublattice, and that it leads to the formation of deep defects in the gallium sublattice. These phenomena are probably attributable to the deviation from stoichiometry produced by isovalent phosphorus (P) impurity which stimulates the silicon-ion-induced formation of shallow donor states in the gallium sites. The use of GaAs substrates doped with indium during their growth has no effect on the electron concentration in the layer but is conducive to better annealing of radiation defects that are produced during ion implantation.

This study was financially supported by the Russian Fund for Fundamental Research.

[1] F. Hyuga, H. Yamazaki, K. Watanabe, and J. Osaka, Appl. Phys. Lett. **50**, 1592 (1987).
[2] V. S. Abramov, I. P. Akimchenko, V. A. Dravin, N. N. Dymova, V. V. Krasnopevtsev, V. V. Chaldyshev, and Yu. V. Shmartsev, Fiz. Tekh. Poluprovodn. **25**, 1355 (1991) [Sov. Phys. Semicond. **25**, 818 (1991)].
[3] M. G. Milvidskii, V. B. Osvenskii, S. S. Shifrin, J. Cryst. Growth **52**, 396 (1981).
[4] Yu. V. Biryulin, N. V. Ganina, M. G. Mil'vidskiĭ, V. V. Chaldyshev, and Yu. V. Shmartsev, Fiz. Tekh. Poluprovodn. **17**, 108 (1983) [Sov. Phys. Semicond. **17**, 68 (1983)].
[5] V. V. Chaldyshev, E. V. Astrova, A. A. Lebedev, I. A. Bobrovnikova, N. A. Chernov, O. M. Ivleva, L. G. Lavrentieva, I. V. Teterkina, and M. D. Vilisova, J. Cryst. Growth **146**, 246 (1995).
[6] A. A. Bergh and P. J. Dean, *Light-Emitting Diodes* (Charendon Press, Oxford, 1976).
[7] A. A. Gutkin, N. S. Averkiev, M. A. Reshchikov, and V. E. Sedov, Mater. Sci. Forum **196**, 231 (1995).

Translated by Paul F. Schippnick

Evolution of the current-voltage characteristics of photoluminescing porous silicon during chemical etching

T. Ya. Gorbach, S. V. Svechnikov, P. S. Smertenko, and P. G. Tul'chinskiĭ

Institute of Semiconductor Physics, Ukrainian National Academy of Sciences, 252650 Kiev, Ukraine

A. V. Bondarenko, S. A. Volchek, and A. M. Dorofeev*

Belorussian State University of Information Technology and Radio Electronics, 220027 Minsk, Belorus

G. Masini, G. Maiello, S. La Monica, and A. Ferrari

Dipartimento di Ingegneria Elettronica, Universita ''La Sapienza,'' Via Eudossiana, 18–00184 Roma, Itali
(Submitted August 20 1996; accepted April 22 1997)
Fiz. Tekh. Poluprovodn. **31**, 1414–1418 (December 1997)

It has been established that chemical etching of porous silicon in HF results in a large change in the current-voltage characteristics and photoluminescence parameters of the silicon. The results of the investigation can be used to increase the efficiency of electroluminescence structures In–⟨porous Si⟩–Al by increasing the injection level of minority carriers and realizing a regime of double injection and high surface recombination rate near the surface of porous silicon.
 [S1063-7826(97)00511-5]

1. INTRODUCTION

Porous silicon (PS) consists of a single-crystal Si layer in which a network of channels–voids, ranging in size from several nanometers to several microns, is formed by electrochemical treatment in hydrofluoric acid. Porous silicon, as a specific morphological form of crystalline silicon, has been known for more than 30 years. The observation of intense room-temperature photoluminescence of porous Si attracted special interest in this material.[1] The discovery of this effect stimulated intensive investigations of the electrical and optical properties of this material. It has now been established that porous Si is a semi-insulating, semiconductor material with a wider gap than that of bulk Si, which possesses a high density of deep centers whose existence and characteristics are determined by the state of the inner surface of the voids.[2–4] Electric excitation of the electronic states in porous Si, which is necessary for subsequent radiative recombination, can be achieved by charge-carrier injection. Structures with injecting contacts have been realized in light-emitting devices with liquid electrolytic and solid-phase film contacts attached to the porous Si layer.[5,6] Over the last three years, the quantum efficiency of electroluminescence structures based on porous Si has improved from 0.01% to 0.1–0.2%,[7] mainly as a result of optimization of the design and fabrication technology of injecting contacts. To further improve the parameters of such structures, the electrical characteristics of porous-Si layers and the effect of different technological factors on them must be investigated in greater depth.

2. EXPERIMENTAL PROCEDURE

The object of the investigations were In–⟨porous Si⟩–Al (In–P-Si–Al) structures. Porous-Si layers, 20 μm thick, were obtained by anodizing a (100) surface of p-type Si with resistivity 12 $\Omega\cdot$cm (KDB-12 silicon) in an electrolyte containing one part by volume of 48% HF acid and 1 part of isopropyl alcohol. The anode current density was maintained constant during the anodization process and was equal to 15 mA/cm^2. Chemically destructive treatment, during which the porous-silicon layer was etched off, was conducted in the solution HF(48%)+H_2O (1:1). An ohmic contact to the backside of the substrate was produced by depositing Al. A 0.02-cm^2 clamped In probe was used as the upper contact for measuring the current-voltage characteristics (IVCs). Such a contact is not ideal for porous Si, but it permits tracing the staged change in the layer and surface parameters of the same porous-silicon structure as it is etched off. The current-voltage characteristics of the In–P-Si–Al structures were measured on an automated tester for monitoring the static parameters of 14TKS-100 transistors. In the structure under study, the forward direction was obtained with a positive voltage applied to the Al contact and, correspondingly, the reverse direction was obtained with a negative voltage. The IVCs were analyzed in the form of the dependence of the differential slope $\alpha = d\log I/d\log u$ on the applied voltage. The parameters of the porous Si layer and the In–P-Si and P-Si–Si interfaces were determined on the basis of the theory of injection-contact phenomena in semiconductors.[8] The change produced in the morphology of porous Si by the chemical destruction of the silicon was studied in a SEM- S-806 scanning electron microscope.

The photoluminescence spectra were measured on standard equipment under excitation with a 25-mW argon laser ($\lambda = 514.5$ nm).

3. EXPERIMENTAL RESULTS AND DISCUSSION

The evolution of the current-voltage characteristics of In–P-Si–Al structures as a function of etch time t_d is shown

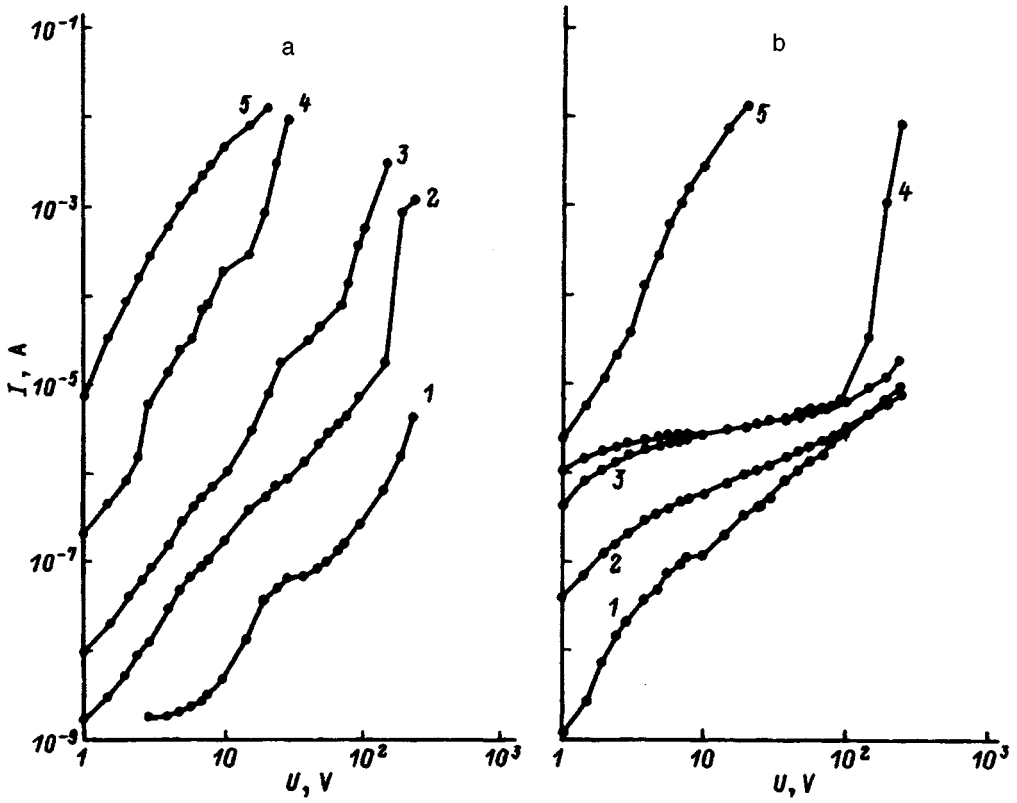

FIG. 1. Evolution of the current-voltage characteristics of a In–⟨porous Si⟩–Al structure in the forward (a) and reverse (b) directions as a function of etch time t_d, s: *1* — 0, *2* — 5, *3* — 40, *4* — 70, *5* — 110.

in Fig. 1. The results of analysis of the IVCs in the form of a dependence of the differential slope α on the applied voltage and the etch time of the porous-Si layer are presented in Fig. 2. Such an analysis makes it possible to distinguish the ohmic sections with $\alpha=1$, characteristic sections with $\alpha=2$, current sections with $\alpha>2$, sections of current saturation with $\alpha<1$, and other features of the IVCs. As follows from Fig. 1, the initial IVC in the forward direction has a small sublinear section of rectification with a bias of the order of 30 V, and sublinearity is observed in both directions at currents of the order of 10^{-7} A (Fig. 1a and 1b, curve *1*). This could be due to the formation of an oxide layer on the walls of the voids. The photoluminescence spectrum (Fig. 3, $t_d=0$) has a maximum ($\lambda_{\max}=790$ nm) and an intensity $I_{\text{fl max}}$ of the order of 0.1 of the maximum value.

Etching for 5 s removes the oxide layer. This decreases the resistance by 1.5 orders of magnitude in the forward direction and by an order of magnitude in the reverse direction (Fig. 1a and 1b, curve *2*). The intensity of the photoluminescence increases by an order of magnitude without any change in the position of the maximum (Fig. 4, $t_d=5$ s).

The quantitative and qualitative changes in the forward and reverse IVCs for etch times of the porous-Si layer from 5 to 35 s were very small: The forward currents doubled. The photoluminescence intensity had a maximum value and was constant, but the spectrum underwent a blue shift from 790 to 740 nm (Fig. 4, $5<t_d\leqslant 35$ s). Increasing the etch time by another 5 s ($t_d=40$ s) not only increased the forward and reverse currents (Fig. 1, curve *3*), but also led to the appearance of a section of current saturation on the reverse IVC ($\alpha=0.52$, Fig. 2b, curve *3*), pronounced current jumps ($\alpha=3.5$, 4.2; Fig. 2a, curve *3*) on the forward IVC, and vanishing of the quadratic section on the reverse branch (Fig. 2b, curve *3*). On the one hand, this gave rise to a decrease in the thickness of the porous-Si layer and etching off of the layer and, on the other, it attests to an improvement in the minority-current-carrier injection condtions at the In–P-Si boundary under a forward bias. At the same time, the photoluminescence intensity dropped by an order of magnitude (Fig. 3, $t_d=40$ s), but the position of $\lambda_{\max}$ changed very little.

Subsequent etching of the porous-Si layer ($40<t_d\leqslant 70$ s) produced a very small increase in the saturation current of the reverse IVCs up to 4×10^{-6} A (Fig. 1a and 1b, curves *3* and *4*) and an increase in the degree of saturation (from $\alpha=0.52$ with $t_d=40$ s up to $\alpha=0.2$ with $t_d=70$ s; see Fig. 2b, curves *3* and *4*, respectively). The currents on the forward IVC increase substantially, the IVC is not exponential, and the current jumps increase to $\alpha=6.4$. In this case, a change in the polarity of the applied voltage is accompanied by a substantial rectification; the rectification coefficient has the largest value in the range 20–30 V and reaches a value of 10^4, which produces favorable conditions for injection of two types of carriers and appearance of electroluminescence in this layer. A diode-type IVC also corresponds to a maximum blue shift ($\lambda_{\max}=680$ nm). Investigations in an electron microscope showed that the porous structure of the Si layer remains, and that the thickness of the porous-Si layer decreases to 3 μm. The latter circumstances

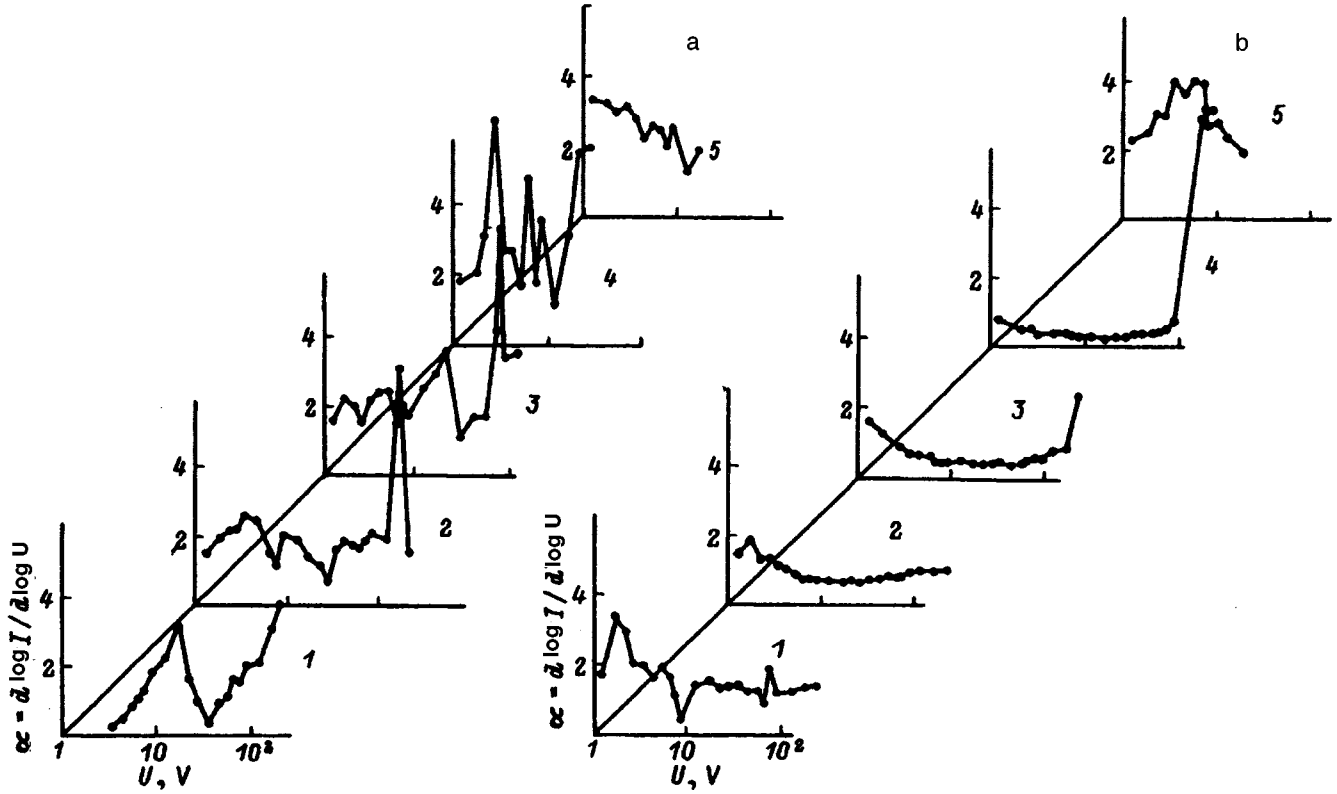

FIG. 2. Differential slope $\alpha = d \log I/d \log u$ versus applied voltage in the forward (a) and reverse (b) directions for the current-voltage characteristics shown in Fig. 1.

suggest that surface centers play a dominant role for explaining the nature of photo- and electroluminescence.

Etching for 110 s was sufficient in our case to dissolve the porous-Si layer. This is indicated by the fact that the IVCs are qualitatively the same in the case of both polarities (Figs. 1a and 1b, curve *5*). However, because of the particular shape of the Si surface, the current for the observed IVCs differs by an order of magnitude from the current in the case of structures fabricated on the basis of a Si single crystal.

The theory of injection–contact phenomena in semiconductors was used to estimate the parameters of the porous-Si layer and In–P-Si and P-Si–Si interfaces.[8–10] Figure 4 shows the following curves:

— attachment coefficient g_r of charge carriers on localized states lying above the monoenergetic center (Fig. 4a) versus etch time;

— densities N_r corresponding to the filling of localized states determined from to the current jumps versus the energy position of these states (Fig. 4b);

— surface recombination rate S_k at the In–P-Si interface (Fig. 4c) versus the etch time.

It should be noted that the parameters presented above are approximate because of the large uncertainty in both the geometric dimensions of the elements in the porous structure and in the physical parameters employed for the calculations. We used the following material constants: majority and minority charge carrier mobility $\mu_p = 380$ cm^2/(V·s) and $\mu_n = 1400$ cm^2/(V·s), respectively; majority and minority charge carrier effective masses $m_p = 0.4m_0$ and $m_n = 0.8m_0$, respectively; permittivity $\varepsilon = 12$, and absolute temperature $T = 300$ K.

Figure 4a shows that the change in the attachment coefficient of minority charge carriers ($g_r \simeq 10^5$) on upper-lying local states in the region adjoining the P-Si–Si boundary changes very little in the process of chemical etching of porous Si, while g_r in the region adjoining the In–P-Si boundary decreases by four orders of magnitude. In other words, chemical etching sharply decreases the number of shallow

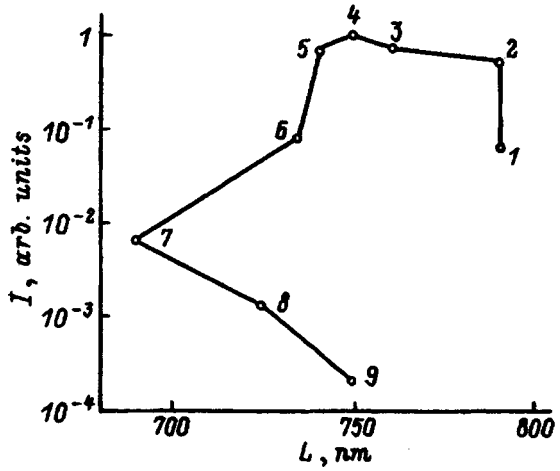

FIG. 3. Photoluminescence intensity I at the maximum and position L of the maximum of the photoluminescence spectra versus etch time t_d, s: *1* — 0, *2* — 5, *3* — 15, *4* — 25, *5* — 35, *6* — 40, *7* — 70, *8* — 80, *9* — 110.

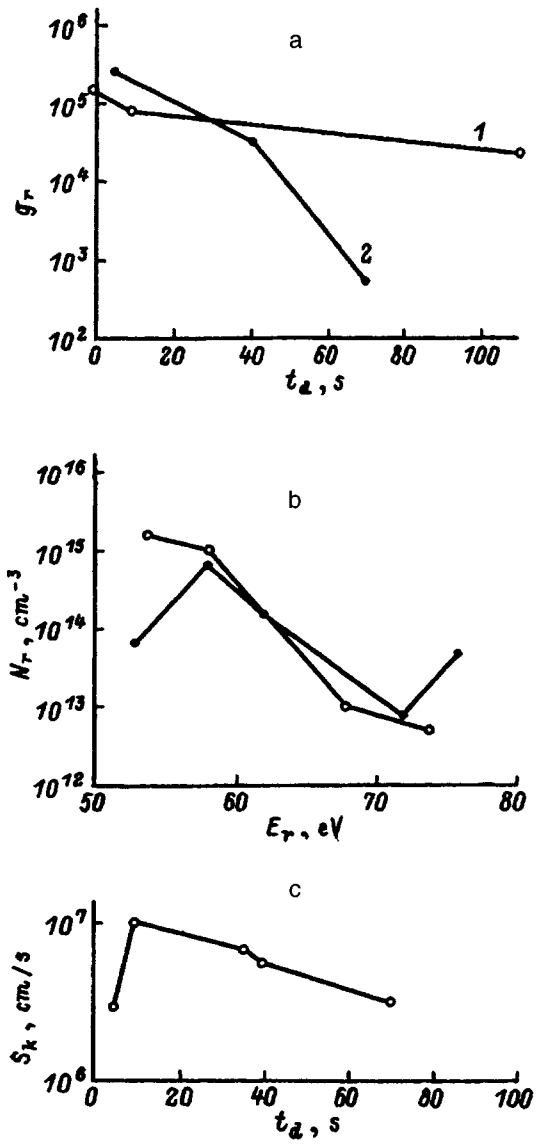

FIG. 4. Curves calculated from the experimental data: a — Charge-carrier attachment coefficient g_r versus etch time t_d; the curves *1* and *2* were determined at the P-Si–Si and In–P-Si interfaces, respectively; b — density N_r of localized states versus their energy; c — surface recombination rate S_k at the In–P-Si interface versus etch time t_d.

attachment centers on the outer boundary of the porous Si. This could promote injection of minority current carriers in the porous-Si layer and, correspondingly, an increase in the recombination, which in turn can increase the probability of radiative recombination. The energy distribution of deep recombination centers [$N_r(E_r)$ in Fig. 4b] attests to the fact that they coincide at energies ranging from 0.58 to 0.72 eV for both boundary regions of porous Si, and their density increasing by two orders of magnitude with decreasing depth. As the energy depth of the deep recombination centers decreases further to 0.52 eV, their density decreases for the region near the In–P-Si interface by more than an order of magnitude compared with Si–P-Si. It should be noted that the surface recombination rate S_k at the outer boundary (In–P-Si) (Fig. 4c) is correlated with the photoluminescence intensity (Fig. 3): The maximum values of the photoluminescence at $t_d = 15$ and 35 s corresponds to higher values of S_k, which also indicates that the skin layer of porous Si must play a dominant role for efficient photoluminescence. The contact is close in this case: For all values of t_d, chemical etching does not change the contact gap width at the In–Pi-Si boundary and the gap width is of the order of $(2 \pm 0.5) \times 10^{-8}$ cm, i.e. the screening radius in a metal.[8]

The skin layer of porous Si probably also plays a determining role in the appearance of electroluminescence in the porous Si-layers studied by us. In our view, a rectifying IVC is also necessary to obtain electroluminescence. Such an IVC can be obtained by etching the initial porous Si for 40–70 s. Furthermore, a double-injection current regime must be realized in order to obtain a sufficient recombination intensity. A discrimination factor Q, defined as the ratio of the volume charge in the zone of the experimental structure to the charge carrier density in the conduction band, in all cases was much greater than 1: it was of the order of 10^6.

In summary, chemical etching of porous Si in HF results in large changes in the IVCs, the photoluminescence spectra, and the morphology of porous Si with increasing etching. These changes can be explained by assuming that the properties of porous Si are nonuniform over the thickness. A method was proposed for increasing the probability of obtaining electroluminescence by producing the required conditions in an In–P-Si–Si–Al structure: increasing injection of minority charge carriers, realization of a double carrier-injection regime, and creation of a high surface recombination rate in the skin layer of porous Si.

A. V. Bondarenko is grateful to the G. Soros International Program for Education in the Field of the Exact Sciences for partial financial support of this work.

*Fax: (0172) 310-914; e-mail: vitaly@silicon.rei.minsk.by

[1] L. T. Canham, J. Appl. Phys. Lett. **57**, 1046 (1990).
[2] D. Stievenard and D. Deresmes, J. Appl. Phys. Lett. **67**, 1570 (1995).
[3] V. P. Bondarenko, E. A. Bondarenko, A. M. Dorofeev, V. A. Samuĭlov, and G. N. Troyanova, Vest. BGU, No. 1, 80 (1995).
[4] Z. Chen, T.-Y. Lee, and G. Bosman, J. Appl. Phys. Lett. **76**, 2499 (1994).
[5] L. T. Canham, MRS Bull. **18**(7), 22 (1993).
[6] V. P. Bondarenko, V. E. Borisenko, A. M. Dorofeev, A. A. Leshok, and G. N. Troyanova, Zarubzh. Élektron. Tekh., No. 1–3, 41 (1994). 1–3, 41 (1994).
[7] A. Loni, A. J. Simons, T. I. Cox, P. D. J. Calcot, and L. T. Canham, Electron. Lett. **31**, 1288 (1995).
[8] A. N. Zyuganov and S. V. Svechnikov, *Injection-Contact Phenomena in Semiconductors* [in Russian], Kiev, 1981.
[9] E. V. Astrova, S. V. Belov, and A. A. Lebedev, Fiz. Tverd. Tela (St. Petersburg) **38**, 702 (1996) [Phys. Solid State **38**, 388 (1996)].
[10] L. A. Golovan', A. V. Zoteev, and P. K. Kashkarov, Pis'ma Zh. Tekh. Fiz. **20**, 66 (1994) [Tech. Phys. Lett. **20**, 334 (1994)].
[11] V. V. Chistyrakov, Mikroelektronika **24**, 143 (1995).

Translated by M. E. Alferieff

Energy spectrum of oxygen-implanted lead telluride deduced from optical absorption data

A. N. Veĭs

St. Petersburg State Technical University, 195251 St. Petersburg, Russia
(Submitted December 18, 1996; accepted for publication April 22, 1997)
Fiz. Tekh. Poluprovodn. **31**, 1419–1421 (December 1997)

The thermoelectric power and optical absorption spectra of single-crystal PbTe, implanted with oxygen and vacuum annealed, have been investigated. A quasilocal level, which could be associated with oxygen, was found in the PbTe:O^+ valence band. © *1997 American Institute of Physics.* [S1063-7826(97)00611-X]

Annealing in air or in an oxygen atmosphere (so-called activation) has long been used to produce photodetectors based on lead chalcogenides.[1–4] This explains the interest in studying the characteristics of the doping effect of oxygen and the energy spectrum in activated layers. The objects of such investigations were mostly single-crystal lead sulfide films. It was established that activation diminishes the density V_{ch} of anionic vacancies and the type of conductivity in the films is inverted from *n*-type to *p*-type conductivity. These facts form the basis of two models explaining the characteristics of the doping effect of oxygen in lead chalcogenides. According to one model, the hole-type conductivity in activated films is due to lead vacancies. The other concept attributes the inversion of the type of conductivity in activated films to the acceptor action of oxygen.

The investigation of the electrical and photoelectric properties has suggested that two energy levels—recombination and attachment (see Refs. 1–4 and the work cited there) exist in the band gap of activated films. Apparently, the best substantiated assumption is that of Ref. 5, according to which both levels are associated with intercrystallite layers along which current transport in activated films occurs. However, if both levels are associated with the action of oxygen in a lead sulfide matrix,[1–4] it is difficult to understand the reason for such a strong dependence of the energy characteristics of these deep levels on the technology used to fabricate the films and the methods for activating them.

The many experimental studies performed on activated polycrystalline films, therefore, have not established either the mechanism of the doping effect of oxygen or the energy spectrum of this impurity in lead chalcogenides. In the present paper we report the latest results of the ongoing study of this problem. However, single-crystal lead telluride with a variable density of anionic vacancies was chosen in this study as the object of investigation. The density V_{ch} was decreased either by introducing intrinsic defects or by introducing thallium as an acceptor impurity (with density $N_{Tl} \leqslant 0.1$ at. %) and superstoichiometric tellurium Te_{exc} into the charge and the density was increased by ionic doping with argon with doses 10^3-10^4 μC/cm^2.

Oxygen was introduced into the experimental samples by ion implantation (ion energy —100 keV, ion current —0.5 μA/cm^2). This method makes it possible to dope single crystals with a high degree of layer-wise uniformity. The ion implantation process was conducted through prepared optical surfaces of the samples. Postimplantation annealing of the samples was performed in evacuated quartz cells for 1 h at $T=300$ °C. After implantation and annealing, the thicknesses of the experimental samples were decreased to $d=3-6$ μm by mechanical grinding and polishing of the opposite (with respect to implantation) sides. The optical absorption spectra α and the thermoelectric power S were investigated by a probe method at all stages of doping and annealing. The experiments were performed at a temperature of 96 and 300 K.

Some experimental results are shown in Fig. 1. The optical data obtained in the initial samples are characteristic of lead telluride in the absence of strong self-compensation. Among the initial samples, the spectra $\alpha(\hbar\omega)$ in *p*-type PbTe:Tl, Te_{exc} were most complicated. These spectra (curve *1* in Fig. 1), together with the components $\alpha_{\Sigma L}$, which are associated with optical transitions of electrons between the extrema L_6^+ and Σ_5 of the valence band, were observed to contain bell-shaped features α_0 which are due to the optical charge transfer on thallium impurity centers[6] (the indicated additional absorption bands are marked by arrows in Fig. 1). The energy diagram for PbTe:Tl, Te_{exc} is shown in Fig. 2. The energy levels E_i $(i=0,1,\ldots,4)$ in the diagram correspond to the bands α_i in the optical absorption spectra. The spectral dependences of the optical absorption coefficient in PbTe:Ar^+ have been studied before and are presented in Ref. 7. No bands of appreciable intensity, which provide evidence of the existence of local or quasilocal states, were observed in the spectra $\alpha(\hbar\omega)$ of the other samples.

Oxygen implantation is accompanied by inversion of the conductivity type $p \rightarrow n$. This is indicated not only by the change in the sign of the thermoelectric power, but also by the results of investigations of the optical absorption spectra. As one can see from Fig. 1 (curve *2*), characteristic bell-shaped, additional absorption bands α_1 and α_2, which are associated with singlet and doublet terms of the chalcogen vacancy, appear in these spectra.[7,8] The contribution of the nonimplanted part of the samples is manifested in the form of the bands α_0 associated with thallium.

Annealing of the oxygen-implanted samples is accompanied by reversion of the conductivity from *n*-type to *p*-type. This is indicated by a change in the sign of S and the appearance of new bands (α_3 and α_4) in the optical absorption spectra (Fig. 1, curves *3, 4*). The first of the indicated bands was also observed earlier in Ref. 6 in strongly compensated

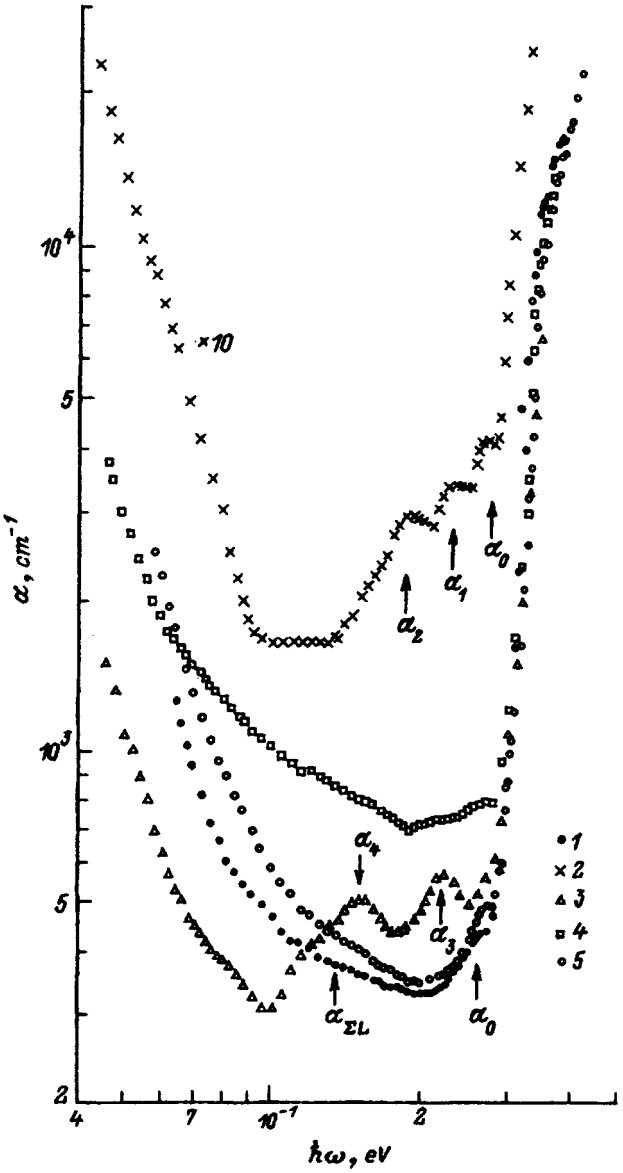

FIG. 1. Spectral dependences of the absorption coefficient in *p*-PbTe:Tl, Te_{exc} (*1, 2, 4, 5*) and *n*-PbTe doped by deviation from stoichiometry (*3*). $T=300$ K. *1*—Initial sample; *2–5*—ion-implanted samples. Impurities introduced: *2, 3*—O^+, *4*—Ar^+ and O^+, *5*—Ar^+. Implanted oxygen dose D_{O^+}, 10^3 μC.cm^2: *1, 5*—0; *2, 3*—3; *4*—2. Implanted argon dose D_{Ar^+}, 10^3 μC/cm^2: *1–3*—0; *4*—10; *5*—3. Annealing: *2*—no, *3–5*—yes.

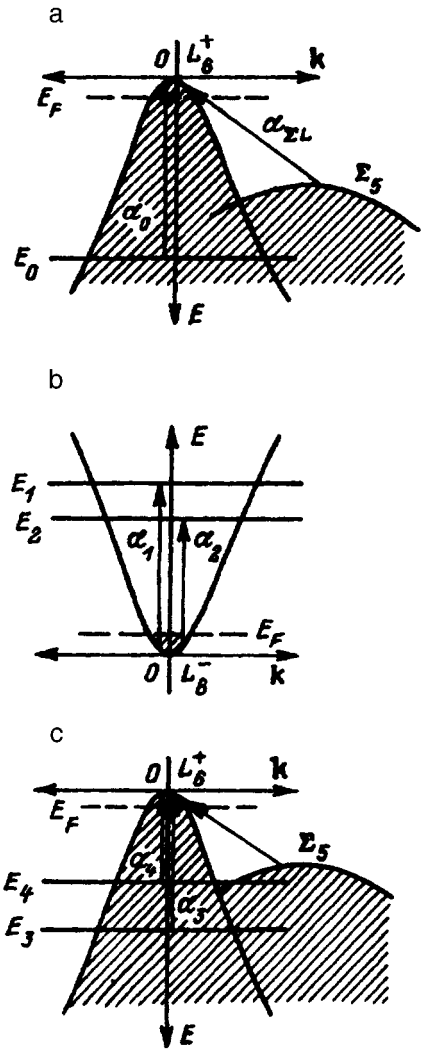

FIG. 2. Energy scheme: (a,b)—*p*-PbTe:Tl, Te_{exc} in initial state (a) and after O^+ implantation (b); c—*n*-PbTe, doped by deviation from stoichiometry, after O^+ implantation and vacuum annealing. The arrows mark optical electron transitions giving rise to additional absorption bands in the spectra $\alpha(\hbar\omega)$.

PbTe, doped with Na or Tl and superstoichiometric lead, and it was attributed to intrinsic donor-type defects, presumably V_{ch}. The second band (α_4) has no analogs in the published data and points to the existence of a new quasilocal level, which can be attributed to the effect of oxygen, in oxygen ion-doped and annealed samples.

The optical charge transfer energies at different centers, which give rise to the appearance of bell-shaped features in the spectra $\alpha(\hbar\omega)$, were determined by calculating the frequency dependences of the additional absorption coefficient. In so doing, the methods described in detail in Ref. 8 for distinguishing the bell-shaped components from the optical absorption spectra and calculating their spectral dependences were used. It was found that at $T=300$ K the optical charge transfer energy E_0 is 0.285 ± 0.007 eV at a thallium impurity center, $E_3=0.245\pm0.010$ eV for a chalcogen vacancy, and $E_4=0.180\pm0.015$ eV for a center associated with oxygen. The indicated values of E_0, E_3, and E_4 were obtained by averaging the data for seven samples, which was done by methods of mathematical statistics using the Student distribution[9] with reliability $t_S(n)=0.95$. As the temperature was lowered to 96 K, the values of E_0, E_3, and E_4 decreased to 0.22 ± 0.02, 0.175 ± 0.020, and 0.14 ± 0.02 eV, respectively. We note that the values of E_0 and E_3 determined for PbTe:O^+ correspond to the data for lead telluride doped with sodium or thallium and superstoichiometric lead.[6]

In conclusion, we shall briefly discuss some features of the experimental data which we obtained. First, it was found that the intensity of the α_4 bands increases not only with increasing implanted-ion dose, but also with increasing density of anionic vacancies in the initial samples. This result is consistent with the existing concept, according to which oxygen occupies a site in the chalcogen sublattice, healing the

vacancy. Second, the α_3 bands attributed to chalcogen vacancies are present in the optical spectra of vacuum annealed PbTe:O^+. As is well known,[10] annealing of ion-implanted lead chalcogenides under substantially less stringent conditions (25 min at $T=250$ °C) ordinarily results in aging of all radiation defects, including vacancies. This is also confirmed by the data obtained in our study. As one can see from Fig. 1 (curve *4*), there are no α_3 bands in the spectrum $\alpha(\hbar\omega)$ of *p*-type PbTe:Tl, Te_{exc} implanted with argon to a dose of 10^4 μC/cm^2 and vacuum annealed for 1 h at $T=300$ °C. The impossibility of completely removing intrinsic defects during annealing shows that oxygen is an acceptor in PbTe and is compensated for by chalcogen vacancies.

In summary, our investigations show that as a result of ion implantation and annealing, oxygen occupies chalcogen vacancies and is an acceptor in PbTe. The quasilocal level E_4 deep in the valence band is due to impurity oxygen. No other local or quasilocal states that could be due to oxygen or associates including oxygen were found in single-crystal PbTe:O^+.

I wish to thank I. O. Usov for performing the ion doping of lead telluride.

[1] R. Bube, *Photoconductivity in Solids*, Wiley, N.Y., 1960 [Russian translation, Inostr. Lit., Moscow, 1962].
[2] L. N. Neustroev and V. V. Osipov, Fiz. Tekh. Poluprovodn. **18**, 359 (1984) [Sov. Phys. Semicond. **18**, 224 (1984)].
[3] L. N. Neustroev and V. V. Osipov, Fiz. Tekh. Poluprovodn. **20**, 59 (1986) [Sov. Phys. Semicond. **20**, 34 (1986)].
[4] L. N. Neustroev and V. V. Osipov, Fiz. Tekh. Poluprovodn. **20**, 66 (1986) [Sov. Phys. Semicond. **20**, 38 (1986)].
[5] V. V. Teterkin, F. F. Sizov, N. O. Tashtanbaev, V. B. Orletskiĭ, and V. D. Foriĭ in *Abstracts of Reports at the 3rd All-Union Conference on Materials Sciences of Chalcogenide Semiconductors* [in Russian], Chernovtsy State University, Chernovtsy, 1991, Part 1, p. 88.
[6] A. N. Veĭs, V. I. Kaĭdanov, and R. Yu. Krupitskaya, Fiz. Tekh. Poluprovodn. **22**, 349 (1988) [Sov. Phys. Semicond. **22**, 215 (1988)].
[7] A. N. Veĭs Fiz. Tekh. Poluprovodn. **30**, 1144 (1996) [Semiconductors **30**, 605 (1996)].
[8] A. N. Veĭs, A. Yu. Rydanov, and N. A. Suvorova, Fiz. Tekh. Poluprovodn. **27**, 701 (1993) [Semiconductors **27**, 386 (1993)].
[9] O. N. Kassandrova and V. V. Lebedev, *Analysis of Observational Results* [in Russian], Nauka, Moscow, 1970.
[10] L. Palmetshofer, Appl. Phys. A: Solids Surf. **34**, 139 (1984).

Translated by M. E. Alferieff

Spectral, energy, and temporal characteristics of two-photon-excited fluorescence of ZnSe single crystal in the blue region of the spectrum

A. M. Agal'tsov, V. S. Gorelik, and I. A. Rakhmatullaev

P. N. Lebedev Physical Institute, Russian Academy of Sciences, 117924 Moscow, Russia
(Submitted February 17, 1996; accepted for publication May 13, 1997)
Fiz. Tekh. Poluprovodn. **31**, 1422–1424 (December 1997)

Two-photon-excited fluorescence (TPEF) spectra of a ZnSe crystal in the blue region of the spectrum have been obtained. The dependence of TPEF on the intensity of the laser radiation has been investigated. It has been established that the energy TPEF are nonlinear. The integrated laser radiation into TPEF conversion coefficient has been measured and was found to be $\sim 10^{-6}$. The TPEF spectra of ZnSe as a function of the delay time were studied. © *1997 American Institute of Physics.* [S1063-7826(97)00811-9]

There has been a rather quite large number of studies devoted to the photoluminescence of ZnSe crystals in the blue region of the spectrum.[1–3] Specifically, in Ref. 2 the luminescence spectra of ZnSe crystals excited by the third harmonic of a Nd^{3+}-activated aluminum yttrium garnet laser ($\lambda = 353.3$ nm) operating in the single-pulse or low pulse-repetition-frequency regime, were recorded.

A new method for observing fluorescence spectra in crystals has recently been developed.[4,5] The method is based on two-photon excitation of the electronic states of the crystal with periodic-pulse laser pumping. Since the crystal was transparent to the exciting laser radiation, the fluorescence radiation spectrum was recorded in a quasi-continuous regime from a comparatively large volume of the sample. In our study, we addressed the problem of obtaining the fluorescence spectra by two-photon excitation (TPE) in a ZnSe single crystal with periodic-pulse laser pumping. We also investigated the dependences of the spectra on the intensity of the exciting radiation and the delay time in the recording system.

The measurements were performed on samples of ZnSe single crystals of a cubic modification with (111) surface orientation. The yellow lasing line ($\lambda = 578.2$ mn) of a copper-vapor laser was used to excite the TPEF spectra. The average lasing power was equal to 2 W, the laser pulse duration was equal to 20 ns, and the pulse repetition frequency was equal to 8 kHz. A FS-17 light filter was placed in front of the experimental object in order to remove lines due to the discharge in the gaseous medium of the laser.

The TPEF spectra were recorded in an ''in reflection'' scheme, described in detail in Refs. 4 and 5. A BG-12 filter was placed in front of the MDR-2 monochromator slit in order to keep out the exciting radiation. The spectral resolution was equal to 0.1 nm and the temporal resolution was equal to 10 ns. The experimental investigations were performed at room temperature.

Figure 1 shows the TPEF spectra of a ZnSe single crystal. The spectra were obtained with different copper-vapor laser radiation power levels. In Ref. 2 it was shown that the main band (2.789 eV) of ZnSe at 77 K has a complicated spectrum: It splits into three components with maxima at 2.793 (E_x), 2.775 (I_1), and 2.745 eV (I^{LO}), respectively. Besides the main band, a series of peaks is observed in the low-energy region of the spectrum: 2.705 (A), 2.676 (A^{LO}), 2.645 (A^{2LO}), and 2.611 eV (A^{3LO}). It was also shown in the same work that at 300 K a band with two maxima near 2.690 and 2.610 eV is observed in the experimental ZnSe crystals. In our case (Fig. 1), the observed spectrum consisted of a wide asymmetric band in the region 460–490 nm. The curve *1* corresponds to the initial power ($P = 0.80 \times 10^7$ W/cm^2). The TPEF radiation intensity was observed to increase with the laser radiation intensity (curves *2* and *3*); furthermore, in the process, the contour became ''deformed'' with increasing relative intensity of the short-wavelength wing; the position of the maximum in the curves (*1–4*) corresponds to 475 nm.

The character of the dependence of the TPEF intensity on the power of the exciting radiation is presented in Fig. 2. This dependence corresponds to wavelength $\lambda = 475$ nm (Fig. 1, arrow). As one can see from this figure, for comparatively low powers of the exciting radiation the power dependence $I(P)$ is quadratic. As P increases ($P > 1.10 \times 10^7$ W/cm^2), this dependence is characterized by an explicit deviation from a quadratic law. This effect can be explained by a transition occurring at high pump power levels from spontaneous fluorescence to stimulated fluorescence, i.e. superfluorescence. It was established on the basis of the measurements performed that for the peak intensity of the exciting radiation, the coefficient of conversion into TPEF for 475 nm equals $\sim 10^{-8}$; for the integrated intensity of the exciting radiation, the coefficient of conversion into TPEF equals $\sim 10^{-6}$.

The TPEF spectra obtained for ZnSe with different delay times with respect to the exciting lasing pulse are presented in Fig. 3. Curve *1* was obtained with zero delay and power density $P = 2.00 \times 10^7$ W/cm^2. For a delay $t = 35$ ns (curve 1) the intensity of the TPEF signal drops sharply. The position of the maximum of the TPEF band ($\lambda = 475$ mn) shifts by 3 nm in the long-wavelength direction and corresponds to 478 nm. For delays of 80 and 100 ns, the TPEF signal decreases even more; the maximum in the spectrum shifts to 480 nm. The spectrum observed in the latter case is found to be similar to the luminescence spectrum obtained at low intensity (Fig. 1), and it is similar to the resonance fluorescence spectrum.[6]

The observed differences of the TPEF spectrum of ZnSe

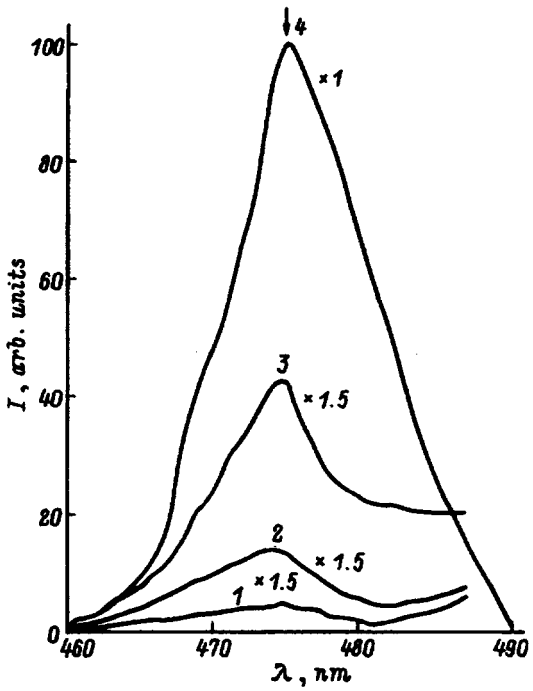

FIG. 1. TPEF spectra of a ZnSe single crystal. The spectra were obtained with different pump powers. Power density, 10^7 W/cm^2: *1*—0.8, *2*—1.1, *3*—1.5, *4*—2.

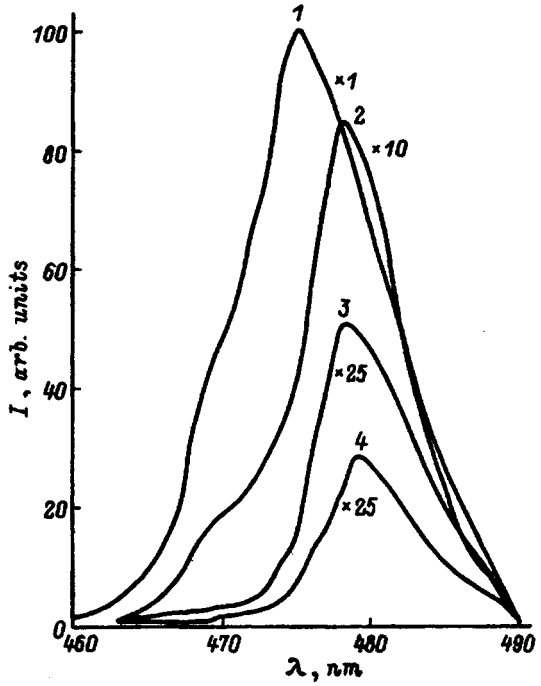

FIG. 3. TPEF spectra of a ZnSe single crystal. The spectra were obtained with different delay times, ns: *1*—0, *2*—35, *3*—80, *4*—100.

from the previously observed resonance photoluminescence spectra (Fig. 1) can be interpreted as follows. The energy of free excitons in zinc selenide is $E_x = 2.812$ eV and $A = 2.690$ eV (Fig. 1), which corresponds to wavelengths $\lambda = 440.9$ and 460.9 nm. Peaks due to the decay of excitons into a photon and one or several longitudinal optical phonons appear in such spectra (Fig. 1). As one can see from Fig. 1 (see position of the arrow), the maximum intensity in the TPEF spectrum corresponds to three-phonon repetition (A^{3LO}). The absence of components with shorter wavelengths in the TPEF spectra can be explained by the fact that these components are absorbed in the volume of the sample, while such absorption is very weak for resonance fluorescence occurring in a thin surface layer of the crystal.

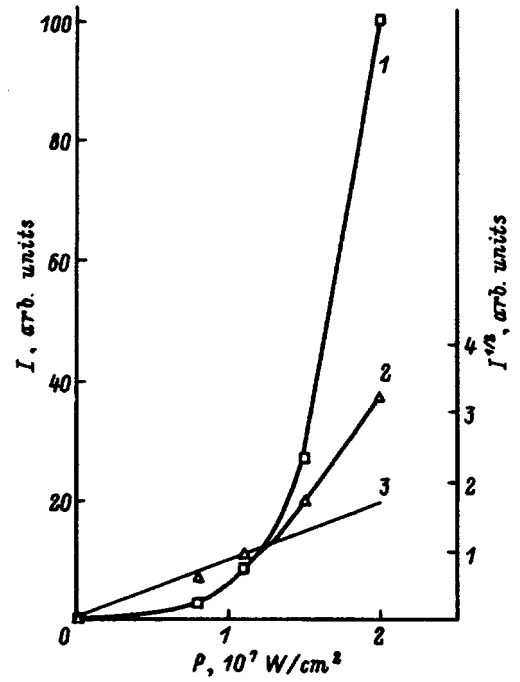

FIG. 2. TPEF intensity I (*1*) and $I^{1/2}$ (*2*) versus pump power P and the theoretical dependence corresponding to the quadratic law (*3*). The curves correspond to wavelength $\lambda = 475$ nm.

The deformation of the TPEF contour—an increase in the intensity of the short-wavelength region—with increasing exciting radiation intensity can be explained by a gradual transition from the spontaneous into induced fluorescence regime (superfluorescence). This result is confirmed by the observed dependence of the TPEF intensity on the exciting radiation density. It is evident from Fig. 2 that for $P = 1.5 \times 10^7$ W/cm^2 this dependence is characterized by an exponent greater than 2. This attests to a transition into the superfluorescence regime, since in the spontaneous TPEF regime this dependence if quadratic, i.e., $I_{\mathrm{TREF}} \sim P^2$.

The observed changes in the form of the TPEF spectra with different delay times (Fig. 3) can also be interpreted as a manifestation of superfluorescence with a high pump power density. In the case of zero delay (curve *1*), the TPEF spectrum is shifted into the short-wavelength region, since the induced emission occurs practically synchronously with the pump pulse. When the strobe pulse is shifted, the fluorescence spectrum acquires a spontaneous character, which is expressed as a deformation of the contour of the spectrum, a sharp decrease in the intensity, and a change in the position of the maximum of the TPEF band.

In summary, TPF spectra of a ZnSe single crystal in the blue region of the spectrum have been obtained by the

method of periodic-pulse–photon excitation and the dependences of the spectra on the pump power and delay time were investigated. It was established that the energy dependences of TPEF are nonlinear. The observed changes in the TPEF spectra at high pump powers are explained by the appearance of induced fluorescence.

The data obtained on the TPEF spectra of a ZnSe single crystal can be used to develop methods for analyzing the characteristics of luminophores containing zinc selenide. It is possible to investigate not only chemically pure materials but also materials of heterogeneous compounds and also structures with impurities and defects.

The stimulated TPEF effect observed by us for ZnSe crystals at room temperature opens up the possibility of producing new tunable-wavelength lasers in the blue region of the spectrum. To realize such lasers, additional investigations must be performed using optical cavities.

[1] V. S. Gorelik, K. N. Kekelidze, and K. A. Prokhorov, Kratk. Soobshch. Fiz. FIAN No. 11, 5 (1990).
[2] G. N. Ivanova, D. D. Nedeoglo, A. V. Simashkevich, and K. D. Sushkevich, Fiz. Tekh. Poluprovodn. **14**, 31 (1980) [Sov. Phys. Semicond. **14**, 17 (1980)].
[3] Koh Era and D. W. Langer, J. Lumin. **1–2**, 514 (1970).
[4] A. M. Agal'tsov, V. S. Gorelik, and T. F. Faĭzullov, Kratk. Soobshch. Fiz. FIAN, No. 2, 15 (1982).
[5] V. S. Gorelik, A. M. Agaltzov, and L. I. Zlobina, J. Mol. Struct. **266**, 121 (1992).
[6] A. N. Georgobiani and M. K. Sheĭkman [Eds.], *The Physics of* II–VI *Compounds* [in Russian], Nauka, Moscow, 1986.

Translated by M. E. Alferieff

Photoconductivity of sulfur-doped silicon near 10.6 μm

Kh. B. Siyabekov and V. T. Tulanov

Tashkent State University, 700095 Tashkent, Uzbekistan
(Submitted December 18, 1996; accepted for publication February 25, 1997)
Fiz. Tekh. Poluprovodn. **31**, 1425–1427 (December 1997)

The extrinsic photoconductivity of Si⟨S⟩ under short-wavelength (10.6 μm) illumination was investigated in the pulsed regime. It was found that sensitivity can be increased by 2–3 orders of magnitude by short-wavelength illumination. It was established that increasing the degree of compensation of the impurity levels of sulfur by γ-ray-induced acceptors decreases both the dark conductivity and the photoresponse due to pulsed illumination with a CO_2 laser. © *1997 American Institute of Physics.* [S1063-7826(97)01412-9]

The photoconductivity of sulfur-doped silicon near 10.6 μm has been studied very little. We know of only one work,[1] where the photoconductivity of Si⟨S⟩ near 10.6 μm was investigated at 5 K.

Our objective in the present work was to investigate the 10.6 μm photoconductivity of Si⟨S⟩ at liquid-nitrogen temperature under the conditions of combined excitation by light.

1. SAMPLE PREPARATION TECHNOLOGY

The starting material consisted of 1.5 mm thick and 30 mm in diameter plates of *p*-type single-crystalline boron-doped silicon with resistivity $\rho = 1600\ \Omega \cdot \mathrm{cm}$.

Sulfur diffusion was conducted at 1250 °C for 20 h followed by cooling in air at a rate of 20 deg/s.

Measurements of the emf by the mobile light-probe method revealed that an inversion layer with conductivity-type opposite to that in the bulk of the crystal formed at the surface of the sample after diffusion. This layer, which is depleted of majority carriers, was of the order of 100 μm thick.

Next, the surface inversion layers were ground off both sides of the plate and phosphorus was diffused at 1200 °C in order to deposit ohmic contacts. After phosphorus diffusion, one side of the plate was ground down by an amount greater than the diffusion penetration depth of the P impurity. Photoresistors were prepared from this series of plates. For this, samples in the form of $10 \times 5 \times 1.5$ mm^3 parallelepipeds were cut from this plate. In contrast to the photodetectors, ohmic contacts were prepared by electrolytic precipitation of nickel. The nickel contacts were separated by 5 mm. The fabrication of the photoresistors was completed by soldering nickel electrodes (thin wires).

2. EXPERIMENTAL PROCEDURE AND RESULTS

The apparatus represented by the schematic diagram in Fig. 1 was used to investigate the photoconductivity of sulfur-doped silicon in the pulsed regime.

A mirror (3) projects through a 3-mm in diameter opening (4) light from a CO_2 laser (1) onto the open surface of the sample (5). A half-transmitting silicon mirror (2) diverted part of the radiation onto a combined germanium photodetector (11) for the purpose of monitoring the shape and power of the radiation pulse. A double-beam oscillograph (6) was used to measure the current kinetics and to monitor the radiation pulse. A voltage pulse produced by a generator (7) is fed into the measuring circuit. A generator (8) synchronously triggers the laser, the oscillograph, and the power-supply generator. The measured signals in the form of the dark current and the photocurrent are taken from the load resistance (9).

A LGI-50 pulsed CO_2 laser with a longitudinal discharge, which produced a weak interference, served as the radiation source for investigation of the photoconductivity.

To obtain quantitative characteristics, it is necessary to know the temporal distribution of the laser radiation intensity. Two measurements were performed for this purpose. The energy in a radiation pulse was determined with an IMO-2M meter (13 mJ, beam diameter 9 mm) and the relative temporal distribution of the radiation was determined with a cooled germanium photodetector. The desired dependence is easily determined from these data. The results of the measurements are presented in Fig. 2a.

The instability of the laser radiation intensity did not exceed 2.5%. The measurement was performed in a special cryostat that cooled the photodetector down to 75 K.

A typical oscillogram of the photoresponse is presented in Fig. 2b. The photoresponse is virtually identical to the CO_2 laser pulse shape. The photoresponse is clearly observed against the dark-current background with excitation intensity of the order of 100 W and current ratio $(\Delta I/I_d)$ 50%.

The ohmicity of the contacts was specially checked by measuring the current–voltage characteristics (IVCs) both in the dark and under illumination. In the final variant of the technological contact-deposition regimes, in all cases a linear IVC was observed and there was no rectification.

Specially performed experiments showed that the photoresponse of the Si⟨S⟩ photodetector depends linearly on the CO_2 laser intensity at least up to 120 W/cm^2. Additional experiments, which were performed using focusing of the radiation, showed that the photoresponse remains linear when the radiation intensity increases by more than an order of magnitude.

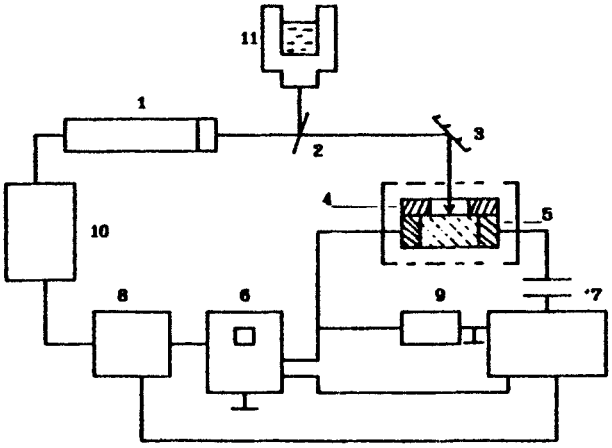

FIG. 1. Schematic diagram of the experimental apparatus for investigating photoconductivity in the pulsed regime. *1* — LG-50 CO_2 laser; *2* — half-transmitting silicon plate; *3* — mirror; *4* — opening; *5* — sample; *6* — oscillograph; *7* — control generator; *8* — delay-line generator; *9* — load resistance; *10* — power supply; *11* — germanium photodector.

3. EXTRINSIC PHOTOCONDUCTIVITY INDUCED IN SI⟨S⟩ BY "SHORT-WAVELENGTH" ILLUMINATION

The impurity photoconductivity induced in Si⟨S⟩ by short-wavelength illumination was investigated on the experimental apparatus described above. The samples were illuminated with an intensity-regulatable incandescent lamp either directly or through germanium or silicon filters. A CO_2 laser with a peak power of 160 W served as the source of the 10.6 μm radiation.

The experiments performed show that the dark current and the photocurrent are linear functions of the illumination intensity, so that the current ratio is the same in all experimental illumination ranges.

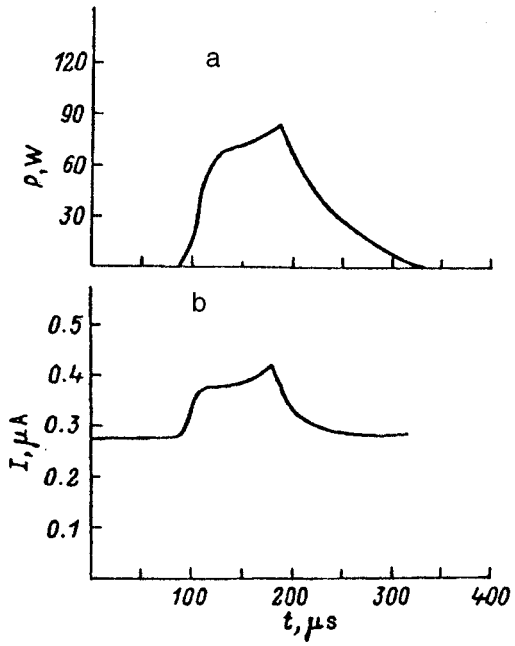

FIG. 2. Oscillogram of the CO_2-laser pulses (a) and of photoresponse of the photodetector under CO_2-laser illumination.

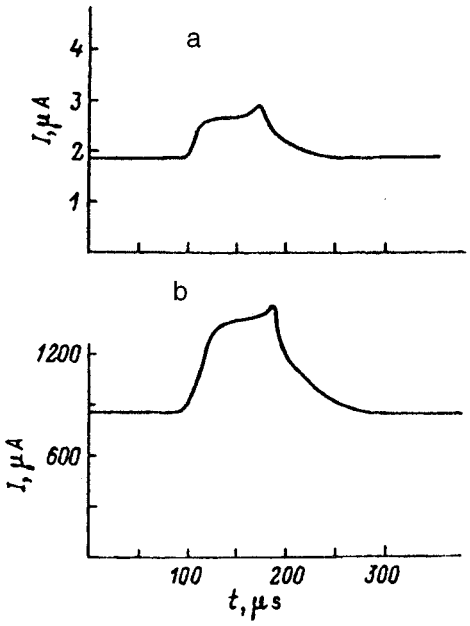

FIG. 3. Oscillogram of the photocurrent in Si⟨S⟩ under pulsed illumination with a CO_2-laser: a — no illumination; b — with illumination.

Figure 3 displays oscillograms of the photocurrents in the sample under illumination with a pulsed CO_2 laser. It is evident from the figure that as the dark current is increased up to 600 μA by means of constant equilibrium illumination, the photocurrent is observed to increase by a factor of 400, i.e. the photosensitivity near 10.6 μm increases substantially.

4. EFFECT OF THE DEGREE OF COMPENSATION OF THE SULFUR IMPURITY LEVELS IN SILICON ON THE 10.6 μM PHOTOCONDUCTIVITY

A widely used method of compensation of impurity levels in silicon is irradiation with γ rays. Irradiation with γ rays produces a series of donor and acceptor levels in the band gap.[2] Since sulfur produces in silicon a series of donor levels in the top half of the band gap[3] and irradiation with γ rays produces donor levels in the bottom half of the band gap, donor levels cannot be manifested in any way in the 10.6 μm photoconductivity. Only the acceptor levels can have an effect, decreasing the degree of filling of the sulfur-induced donor levels and the free-electron density in the conduction band.

Samples with resistivity 80 $\Omega\cdot$cm were investigated. The samples were produced by diffusing sulfur into crucibleless *p*-type silicon with initial resistivity 1600 $\Omega\cdot$cm. The samples were shaped in the form of $10\times8\times1$ mm^3 parallelepipeds. Two nickel contacts separated by 7 mm were deposited electrochemically on one large-area face. Just as in the preceding case, a LGI-50 pulsed CO_2 laser with pulse duration 150 μs and pulse energy 13 mJ served as the radiation source. A constant voltage of 10 V was applied to the sample. The dark current and photoresponse were measured similarly. ^{60}Co with a flux of 1.7×10^{12} photons/cm$^2\cdot$s served as the γ-ray source.

TABLE I.

Sample No.	I_d, A	ΔI, A	$\varkappa=\Delta I/I_d$	t, h
	6×10^{-4}	2.5×10^{-6}	4×10^{-3}	0
11	10^{-6}	5×10^{-7}	5×10^{-1}	3
	10^{-8}	2.5×10^{-8}	2.5	21
13	10^{-3}	3×10^{-5}	3×10^{-2}	0
	10^{-6}	1.5×10^{-7}	1.5×10^{-1}	9

The values of the dark photocurrent (I_d), the photocurrent (ΔI), and their ratio ($\varkappa$) are given in Table I as functions of the γ-irradiation time (Δt) for two samples.

It is evident that as the irradiation time increases, i.e., the degree of compensation increases, the dark current and the photocurrent decrease, while the current ratio increases by two orders of magnitude.

A similar investigation was also performed in Ref. 4 , where it was shown by means of theoretical calculations that at least two energy levels in the band gap in silicon participate in the 10.6 μm photoconductivity of Si⟨S⟩.

In summary, the observation of 10.6 μm photosensitivity of sulfur-doped silicon at liquid-nitrogen temperature gives good prerequisites for producing based on this material an ionization-type semiconductor image converter[5] for recording optical information in the range of CO_2-laser radiation.

We wish to thank V. B. Shuman and E. G. Guk for kindly providing the Si⟨S⟩ samples and G. B. Gorlin for assisting in the technical implementation of the experiments.

[1] N. Selar, Infrared Phys. **167**, 435 (1976).
[2] V. S. Vavilov, I. P. Kekelidze, and L. S. Smirnov, *Effect of Radiation on Semiconductors* [in Russian], Nauka, Moscow, 1988.
[3] A. A. Lebedev, A. T. Mamadalimov, and Sh. Makhkamov, Fiz. Tekh. Poluprovodn. **8**, 262 (1974) [Sov. Phys. Semicond. **8**, 169 (1974)].
[4] G. B. Gorlin, V. T. Tulanov, and Kh. B. Siyabekov, Zh. Tekh. Fiz. **67**, 142 (1997) [Tech. Phys. **42**, 1239 (1997)].
[5] Yu. A. Astrov, A. A. Lebedev, A. T. Mamadalimov, Sh. S. Kasymov, and L. G. Paritskiĭ, Deposited in All-Union Institute of Scientific and Technical Information, No. 2463-75 (1975).

Translated by M. E. Alferieff

Effect of different types of surface treatment on the photoelectric and optical properties of CdTe

A. Baĭdullaeva, A. I. Vlasenko, and P. E. Mozol'

Institute of Semiconductor Physics, Ukrainian National Academy of Sciences, 252650 Kiev, Ukraine
(Submitted June 10, 1996; accepted for publication April 29, 1997)
Fiz. Tekh. Poluprovodn. **31**, 1428–1430 (December 1997)

The photoconductivity and light absorption spectra of p-type CdTe single crystals subjected to different treatments have been investigated. It is shown that the photoconductivity and edge absorption in mechanically polished and plastically deformed crystals are determined by the damaged layer. The role of dislocations in the formation of the edge absorption and the photoconductivity spectrum is determined. © *1997 American Institute of Physics.* [S1063-7826(97)01611-6]

High-resistance CdTe single crystals have, in addition to the standard applications for nuclear radiation detectors, photodetectors, infrared filters, and other optical components, applications as a substrate material for epitaxial growth of $Cd_xHg_{1-x}Te$ films. In this connection, stringent requirements are imposed on the degree of structural perfection of the surface, surface treatment quality, and the method for monitoring its state. In particular, a large slope of the absorption edge, good transmission in the transparency range of the material, a prescribed degree of compensation, and resistance to external actions and degradation are important for optical and photoelectric components. This is often determined by the surface treatment quality and the structural perfection of the surface layers. The treatment quality can be improved by using nonabrasive methods of polishing, which are based on chemical dissolution of the semiconductor and performed under special hydrodynamic conditions.[1] Data obtained by the standard structural diagnostics methods, for example, reflection electron diffraction, show that there is no damaged layer in the usual understanding of this term. However, it is of interest to determine other possible imperfections in the surface region of the crystal that can potentially degrade the quality of epitaxial layers: elastic stress fields, products of chemical treatment that are bound on the surface, and so on.

Existing methods for analyzing and monitoring the degree of structural perfection of a material, probing with electrons and ions, x-ray spectroscopy, Auger spectroscopy, and mass spectroscopy, electron microscopy, infrared reflective adsorption spectroscopy, and other expensive and laborious methods are not always applicable for rapid monitoring of a material. Considering the high sensitivity of the optical and photoelectric properties of semiconductor materials to the degree of their structural perfection and the easy accessibility of these measuring means for purposes of rapid analysis, in the present work we investigated the effect of different forms of surface treatments of CdTe on the optical and photoelectric properties.

1. EXPERIMENTAL PROCEDURE

The p-type CdTe samples with carrier density $\sim 10^{15}$ cm^{-3} and dimensions $1\times 2\times 5$ mm were cut out in a manner so that the wide face (the working face) had [111] orientation and the lateral faces were formed by natural cleavage along the [110] and [101] cleavage planes. To obtain ohmic contacts, a copper layer, to which indium contacts were soldered, was deposited chemically on two freshly cleaved end faces. The working face of the samples was subjected to different types of treatment, including mechanical polishing to produce a structurally damaged layer, layerwise removal of the damaged layer by chemical-dynamic polishing and free etching, as well as chemical treatment for the purpose of removing the etch products. To determine the thickness of the removed material in a layerwise investigation of the damaged layer, a section of the surface was protected with a chemically resistant lacquer and the height of the step formed after etching was measured in a MIII-4 interferometer.

The spectral dependences of the photoconductivity (PC) and transmission were measured on an apparatus assembled on the basis of a MDR-3 monochromator. In the process of removing the damaged layer, the dislocation structure was revealed by treatment in a selective etchant consisting of a 50% CrO_3 solution and HF in a 1:2 volume ratio.

The effect of volume structural imperfections on the transmission and PC spectra was also investigated. Imperfections were introduced by pressing in a diamond indentor with prick density ~ 500 cm^{-2} (the average distance between indentations was equal to 400 μm). For this purpose, a PMT-3 microhardness meter was used: The load on the indentor was equal to 8 gf and the indentations were about 3 μm deep. Prior to indentation, the surface imperfections introduced during the preceding measurements were completely removed by polishing etching to a large depth (200–300 μm).

2. RESULTS AND DISCUSSION

Figures 1 and 2 show, respectively, the photoconductivity and absorption (k) spectra of a p-CdTe crystal with a

 1063-7826/97/121234-03$10.00

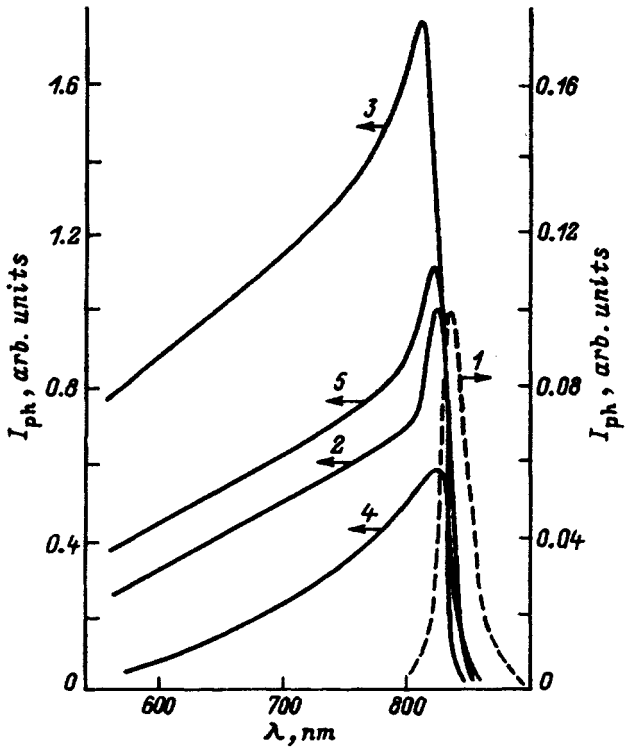

FIG. 1. Photoconductivity spectra I_{ph} of p-type CdTe crystals with different types of surface treatment: *1*—Mechanical polishing (1-μm grain size); *2*, *3*—free chemical etching to depths of 20 and 100 μm, respectively; *4*—indentation; *5*—chemical-dynamical etching to a depth $\sim$200 μm.

(111) working surface and the monitored damaged layer, introduced with different types of treatment as well as by plastic deformation of the sample surface with an indentor. A selective PC band is observed in the initial, mechanically polished sample with a 1-μm grain diameter (Fig. 1, curve *1*).

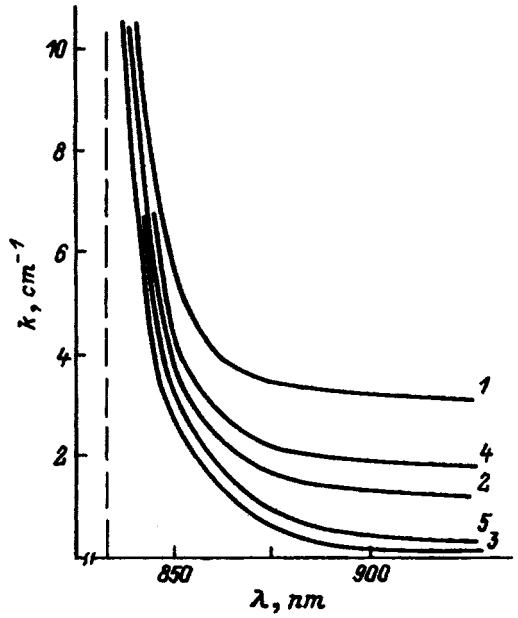

FIG. 2. Optical absorption spectra of p-type CdTe crystals with different types of surface treatment. The numbers on the curves correspond to Fig. 1. The dashed line indicates the positions of the absorption edge in CdTe.

Measurements of the Auger spectra showed that after the damaged layer was removed by chemical polishing of the crystal, the crystal surface is enriched with superstoichiometric tellurium, in agreement with measurements of the Raman scattering spectra from a CdTe surface obtained by chemical-dynamic treatment.[2] The Te film was washed off in a 1-n solution of KOH in methanol.[3] When the 20-μm damaged layer is removed by chemical etching and the Te film is washed off, a PC band appears in the region of the fundamental absorption (the selective PC band is not observed and the photosensitivity increases) (Fig. 1, curve *2*). The light-absorption coefficient in the transparency range of the crystal decreases (Fig. 2, curve *2*). These changes are observed up to 100-μm grains (Figs. 1 and 2, curve *3*). Further removal of the layer by chemical-dynamic polishing does not change the form of the spectrum or the magnitude of the PC and absorption, indicating absence of a damaged layer.

Indentations on the same sample decreased the PC in the entire region of the spectrum and increased light absorption in the transparency range of the crystal (Figs. 1 and 2, curve *4*). Subsequent chemical or chemical-dynamic polishing results in effects similar to those described above; i.e., when a $\sim$200-μm-thick damaged layer produced by indentation is removed, the photoelectric and optical properties of the crystal are restored (Figs. 1 and 2, curve *5*).

Layerwise etching showed that the PC and absorption changed when an up to 200-μm-thick layer was etched off the treated surface. This is much greater than the light absorption depth in the region of the fundamental absorption edge (for CdTe $k\sim10^4$ cm^{-1}). An increase in light absorption in the transparency range of the crystal is observed in the same layer. This increase in absorption passes into the exponential fundamental absorption edge shifted, relative to the edge in the undeformed crystal, into the long-wavelength side of the spectrum, which is characteristic of a material with local stresses produced in the lattice by the introduction of intrinsic and extrinsic defects. For $k\simeq10$ cm^{-1} the shift is $\Delta E=0.33$ eV, in good agreement with the calculations performed in Refs. 4 and 5, where the effect of the density of the introduced dislocations on the photoconductivity and light-absorption spectra was studied. The absorption coefficient of mechanically polished and indented samples in the transparency range of the crystal equals 3 and 2 cm^{-1}, respectively (Fig. 2, curves *1* and *4*). For crystals without a damaged layer $k\simeq0.2$ cm^{-1} (Fig. 2, curve *5*). For this reason, the additional light absorption in the transparency range of the crystal could be due to deformation of the crystal by dislocations, which appear when a damaged layer is produced near the surface of the crystal.

When the damaged layer is removed, the absorption coefficient decreases and at the same time the PC in the region of the fundamental absorption edge increases and the selective band vanishes. As we showed in Ref. 6, the selective character of the PC is due to light absorption in donor-acceptor (DA) pairs. Transfer of excitation energy from a DA pair to sensitized centers can be achieved by Auger interaction, when the excitation energy of a DA pair goes into excitation of an electron from the sensitized center into the conduction band. For this reason, the vanishing of the selec-

tive PC band after the damaged layer is removed, even in an indented crystal, can be explained by a decrease in the concentration of intrinsic defects which form triple associates DA pair+sensitized center. Dislocations are sinks for acceptor-type defects.[7]

In summary, the investigation of the character of the photoconductivity and optical absorption spectra with different treatments of CdTe crystals yields information about the state and degree of structural perfection of the surface of the samples.

[1] G. V. Idenbaum, R. P. Baronenkova, and N. M. Boĭnykh, Fiz. Khim. Obrab. Mater. No. 2, 55 (1971).

[2] V. V. Artamonov, M. Ya. Valakh, V. V. Strel'chuk, P. E. Mozol', and A. Baĭdullaeva, Zh. Prikl. Spektrosk. **48**, 990 (1988).

[3] P. M. Amirtharaj and Fred. I. Pollack, Appl. Phys. Lett. **45**, 789 (1984).

[4] A. V. Bazhenov and Yu. A. Osipyan, Fiz. Tverd. Tela (Leningrad) **22**, 931 (1980) [*sic*].

[5] A. V. Bazhenov and L. L. Krasil'nikov, Fiz. Tverd. Tela (Leningrad) **26**, 590 (1984) [Sov. Phys. Solid State **26**, 356 (1984)].

[6] A. Baĭdullaeva, V. V. Dyakin, V. V. Koval', P. E. Mozol', and E. A. Sal'kov, Fiz. Tekh. Poluprovodn. **20**, 398 (1986) [Sov. Phys. Semicond. **20**, 252 (1986)].

[7] A. Baĭdullaeva, N. E. Korsynskaya, P. E. Mozol' *et al.*, Fiz. Tekh. Poluprovodn. **26**, 801 (1992) [Sov. Phys. Semicond. **26**, 450 (1992)].

Translated by M. E. Alferieff

Properties of *p*-PbTe (Ga) based diode structures

B. A. Akimov, E. V. Bogdanov, V. A. Bogoyavlenskiĭ, L. I. Ryabova, and V. I. Shtanov

M. V. Lomonosov Moscow State University, 119899 Moscow, Russia
(Submitted April 1 1997; accepted May 15 1997)
Fiz. Tekh. Poluprovodn. **31**, 1431–1435 (December 1997)

Single crystals of *p*-PbTe(Ga) with gallium density too low for complete compensation of uncontrollable impurities and intrinsic lattice defects and realization of Fermi level (FL) pinning were investigated for the purpose of producing diode structures In contact–[*p*-PbTe(Ga)]–Pt contact. It was found that the properties of the structures obtained have a number of features that distinguish them from In–[*p*-PbTe] Schottky barriers. The current-voltage characteristics (IVCs) of the experimental structures are not described by the standard relation of the Schottky theory not only in the region of reverse bias but also in the region of direct bias. Residual photoconductivity (PC) is observed under illumination with a thermal radiation source in the temperature range $T<80$ K; after the illumination is switched off, the IVCs are linear. Under constant illumination a photo-emf appears and the branches of the IVCs in the region of reverse biases rectify. The experimental results are discussed on the basis of the assumption that regions with *n*-type conductivity form and FL stabilizes near the nonohmic contact as a result of band bending. It has not been ruled out that *n*-PbTe(Ga) regions are initially present in the sample, but they are not manifested under ohmic contact conditions. [S1063-7826(97)01811-5]

1. INTRODUCTION

Investigations of gallium-doped lead telluride have concentrated, as a rule, on samples in which the amount of Ga introduced was sufficient for complete compensation of the uncontrollable impurities and intrinsic defects. Interest in such samples is due mainly to the pinning of the Fermi level (FL) inside the band gap, the low electron densities, and the appearance of persistent photoconductivity at temperatures below 80 K.[1] However, samples with a low Ga content that exhibit *p*-type conductivity are also an interesting object of investigation, since they possess a number of properties which are uncharacteristic of nondoped *p*-PbTe. Investigation of the galvanomagnetic characteristics of such samples have led to the suggestion that the samples consist of structures which contain, together with *p*-type undercompensated regions, high-resistance *n*-type regions. The samples exhibit a weak photosensitivity, and under illumination inversion of the type of conductivity is observed.[2] Nonetheless, it has not been ruled out that the impurity level in *p*-PbTe(Ga) samples exists in the entire volume of the sample, but since the amount of gallium is too low for pinning of the FL, the impurity centers are completely empty. An argument in favor of this assumption is that the *p*-PbTe(Ga) samples can be transferred into a high-resistance *n*-type state by irradiation with radiation that generates donor-type defects which changes the degree of compensation of the sample.[3] Therefore, the study of the properties of *p*-PbTe(Ga) can shed light on the mechanism leading to the formation of a high-resistance state in PbTe(Ga). On the other hand, it was of interest to analyze the possibility of using *p*-PbTe(Ga) to create diode structures, since the condition for pinning of the FL can be realized and a qualitatively new type of nonohmic content can be formed in the near-contact region depleted of the majority charge carriers (holes).

2. EXPERIMENTAL SAMPLES

PbTe(Ga) single crystals were grown by vapor–liquid–crystal (VLC) mechanism in small temperature gradients between the vaporization zones using a procedure similar to that described in Refs. 4 and 5 . The amount of gallium and the character of its distribution in the volume of the crystal, the charge-carrier density, and the type of conductivity in the ingots grown were varied by varying the temperature regime of growth. Since the concentration of gallium telluride in the melt is much higher than in the growing crystal, excess impurity from the crystallization front is displaced into the volume of the layer of melt in the crystallization zone. If the velocity of the crystallization front is higher than the rate of equalization of the gallium telluride concentration by diffusion from the crystallization front into the volume of the melt and establishment of equilibrium in the volume of the melt as a result of mass transfer from the vapor phase, then melt is trapped by the growing crystal and inclusions of a second phase are formed. These inclusions occupy energetically stressed regions in the volume of the crystal. When the microstructures of the samples grown by the standard VLC method or Bridgman's method is investigated, these microinclusions are easily revealed.[6] During crystal growth in small temperature gradients with gallium telluride concentrations much lower than the maximum possible solubility, it can be expected that the dissolution process will lead to virtually complete vanishing of the growth inclusions in a large part of the crystal volume or even to depletion of growth inclusions in regions with excess internal energy (small-angle boundaries, grain boundaries, and blocks).

The study of the structure of the obtained crystals by secondary-ion mass spectroscopy (Cameca IMS 4F) showed that regions along small-angle boundaries, depleted of gallium compared with regions inside the blocks, do indeed

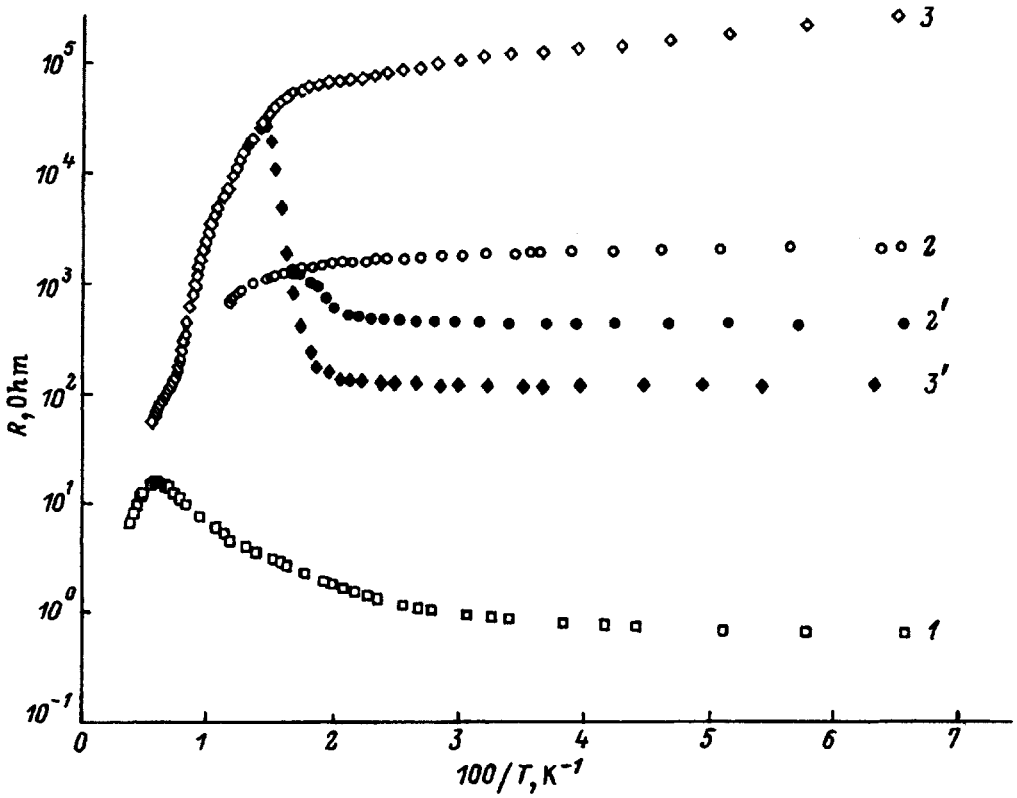

FIG. 1. Temperature dependences of the resistance R of p-PbTe(Ga) with ohmic (Pt) contacts (*1*) and of the structure In contact–[p-PbTe(Ga)]–Pt contact with a direct bias in the current-stabilized regime $I=0.075$ mA (*2*, *2′*) and with a reverse bias in the voltage-stabilized regime $U=-0.1$ V (*3*, *3′*). Curves *1–3* were obtained under screening conditions and curves *2′*, *3′* were obtained under illumination.

exist in the sample studied in this work. However, isolated inclusions of a gallium-enriched second phase are clearly seen inside the gallium-depleted regions. There are noticeably fewer such inclusions in the regions inside blocks.

The crystals were cut perpendicular to the growth axis using a circular saw with an inner cutting edge mounted on a ring. The damaged layer was removed by grinding and chemical-mechanical polishing. Two types of contacts were attached to the samples. Contacts using the alloy 95%In +4%Ag+1%Au were soldered with a microsoldering tool. These contacts to the n-type samples are ohmic and they produce a Schottky barrier with p-type samples. The contact of the second type is a 40 μm in diameter spark-welded platinum wire. It was shown experimentally that contacts of this type are ohmic to p- and n-type PbTe(Ga). All experimental data presented below refer to samples with p-type conductivity (according to thermal probe data at room temperature).

The measurements were performed in a chamber screening the sample from the background illumination. A miniature incandescent lamp with a maximum power of $\sim$30 mW was used as the radiation source.

3. EXPERIMENTAL RESULTS

The temperature dependence obtained for the resistance R of a p-PbTe(Ga) sample with platinum contacts in a potential scheme is shown in Fig. 1 (curve *1*). At a temperature $T\sim160$ K a sharp inflection is observed in the curve, and R drops continuously at low temperatures. In the case of illumination with a thermal source at $T=4.2$ K the conductivity of the sample increased very little ($\sim$5% of the magnitude of the signal). The other curves shown in Fig. 1 were all obtained from measurements on the structures Pt contact–[p-PbTe(Ga)]–In under a direct bias in a stabilized current regime with $I=0.075$ mA (plus on the In contact, curves *2* and *2′*) and with a reverse bias in the voltage-stabilized regime $U=-0.1$ V (curves *3* and *3′*). The curves *2* and *3* were measured under conditions when the sample was screened from the background illumination, and the curves *2′* and *3′* were obtained under illumination with a thermal radiation source. An activation section is observed on curve *2* at high temperatures. The activation energy E_a, determined using the relation $R\sim\exp(E_a/kT)$, was found to be $\sim$110 meV. The same activation energies were obtained for the temperature dependences of the resistance, which were measured with reverse biases $-U=0.2$, 0.3, and 0.4 eV. Under illumination conditions the resistance of the structure decreases and the relative photoconductivity (PC) signal in the region of reverse biases is much higher than the corresponding signal in regions with direct biases. After the source of illumination is switched off, at low temperatures a residual photoconductivity is observed. The onset temperature of the persistent PC is $T_c\sim80$ K.

Figure 2a shows a family of current-voltage characteristics (IVCs) of a structure at different temperatures. The reverse branches of the IVCs for temperatures below 62 K are not shown in the figure. The currents corresponding to $-U=0.1$ V do not exceed 2 μA in this case. A characteristic feature of the IVCs obtained is their pronounced nonlinearity. However, the form of the IVCs is not described by the relation $I=I_s(\exp(qU/kT)-1)$, known for Schottky contacts, not only in the region of reverse biases but also for direct

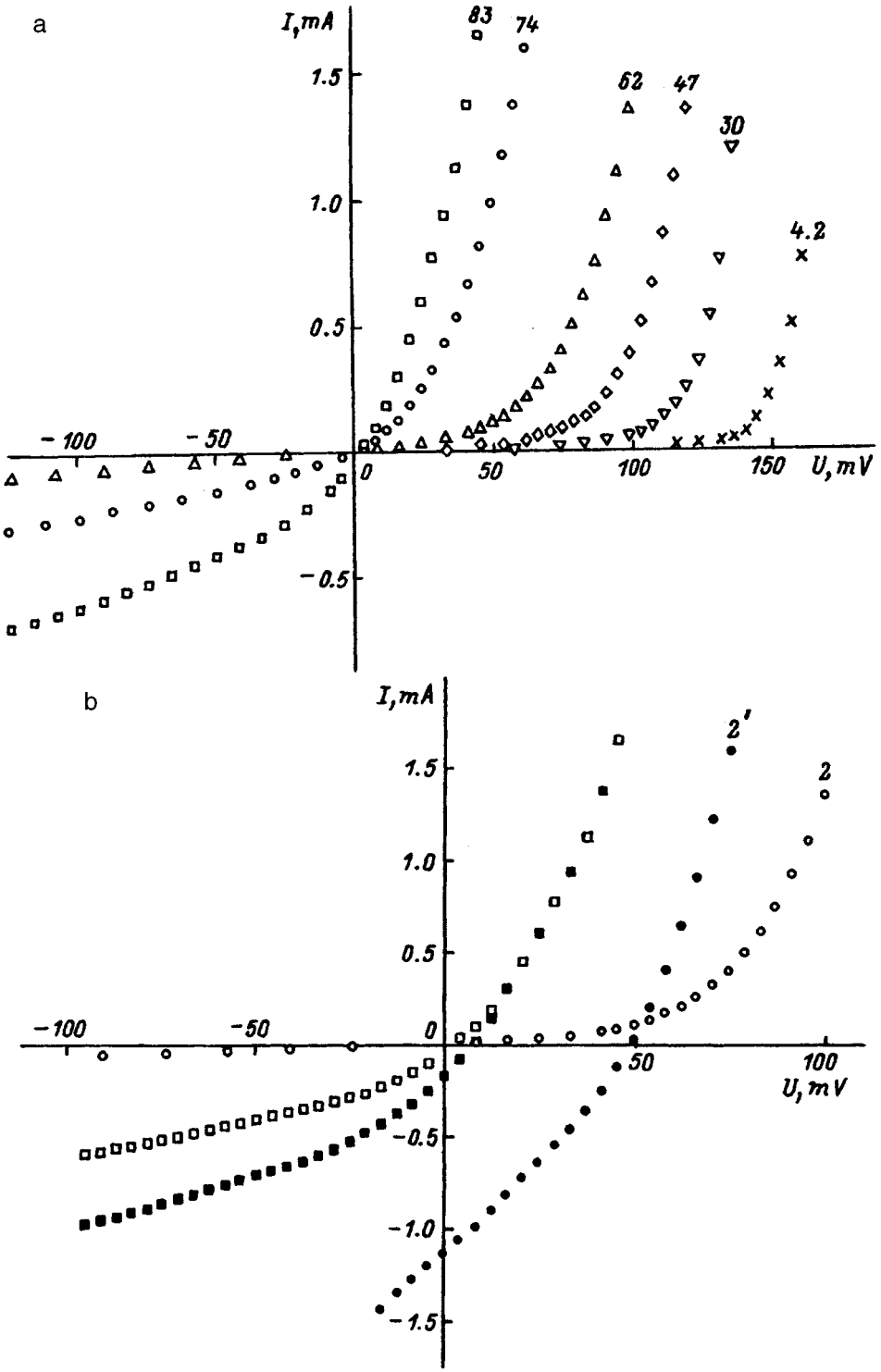

FIG. 2. Current-voltage characteristics of the structure In contact–[*p*-PbTe(Ga)]–Pt contact. a — under screening conditions, the numbers on the curves are the temperature *T*, K. b — *1*, *1′* — $T=85$ K; *2*, *2′* — $T=60$ K; curves *1*, *2* were obtained under screening conditions and curves *2*, *2′* were obtained with illumination switched on.

biases. For example, the presence of sections of weak current growth, which are replaced by rapid growth in I for $U>0.1$ V, on the direct branch is characteristic of the low-temperature IVCs.

A qualitative change occurs in the form of the IVC under illumination with a thermal source (Fig. 2b). Curves *1* and *2* were obtained under screening conditions and curves *1′* and *2′* were obtained with the illumination source switched on. At $T=4.2$ K, after the illumination with a thermal source is switched off, the IVCs under residual conductivity conditions (with the illumination switched off) transform into linear ohmic characteristics.

4. DISCUSSION

Analysis of the experimental data obtained reveals the following most characteristic features. The diode theory does not describe the dark IVCs. Under continuous illumination conditions the reverse branches of the IVCs rectify. Under residual conductivity conditions the nonohmicity vanishes

completely at low temperatures. It should be noted that the IVCs of the structures which we studied are qualitatively different from the IVCs of Cu- and In–p-PbTe contacts which were described in the literature.[7] For this reason, to describe all the experimental data obtained it is necessary to take into consideration both the characteristic features of the Schottky barrier arising at the In–p-PbTe(Ga) contact and the structure of the sample itself.

The presence of persistent PC at low temperatures is characteristic of the high-resistance p-PbTe(Ga) samples. This phenomenon is essentially not observed in the experimental p-type samples with ohmic contacts. Therefore, the regions responsible for the existence of residual PC either are present initially in the sample, but do not make a large contribution to the conductivity under conditions when ohmic contacts are present, or they are formed in the contact region as a result of strong band bending during the formation of the nonohmic contact. It cannot be ruled out that both possibilities are realized simultaneously. Let us assume that under doping with gallium the impurity level located in p-PbTe(Ga) $\sim$75 meV below the conduction band bottom is also present in samples with gallium density N_{Ga} that is too low for complete compensation of uncontrollable impurities and electrically active, intrinsic lattice defects N_i. Then, in p-PbTe(Ga) this level is completely empty and the hole density is determined by the difference $N_i - N_{\mathrm{Ga}}$. In this case, when the band bending near the contact is so large that the impurity level is below the FL, the unoccupied states at this level become filled with electrons and conductivity inversion can be observed in the region of band bending. This situation is very likely, since estimates of the height φ_B of the potential barrier arising on the contact give, in order of magnitude, $\sim$110 meV. The estimates of φ_B were made according to the temperature dependences of the voltage in the region of reverse biases and from the voltage cutoff in the region of direct biases at low temperatures. Since the band gap in PbTe in the limit $T \to 0$ K equals 190 meV, it is very likely that a high-resistance n-PbTe(Ga) interlayer forms in the contact region. On the other hand, considering the investigations of the real structure of the experimental samples, p-type regions can be represented as narrow channels, corresponding to gallium-depleted regions, on small-angle boundaries. At the same time, intrablock volumes consist of high-resistance n-PbTe(Ga). The structure seemingly consists of two interpenetrating substructures, one of which possesses electronic conductivity and other hole conductivity. In this case the temperature dependences of the resistance of the structure can be described by an equivalent circuit consisting of two samples connected in parallel, the p-type sample having a high integral resistance at high temperatures on account of the narrowness of the percolation channels. The resistance, therefore, is initially observed to increase upon cooling under the conditions of the measurements performed with the aid of ohmic contacts (Fig. 1, curve *1*), but as the resistance of the n-regions increases and that of the p-regions decreases, an inflection is observed in the temperature dependence $R(T)$. In structures with an indium contact, the character of the current flow along p-type regions will be determined by the Schottky barrier on the contact and in n-type regions it will be determined by the activation of extrinsic conductivity. Indeed, the activation energy of the conductivity, determined from the temperature dependences of the resistance of the structure in ac measurements in the temperature range $T > 77$ K, is virtually identical to the activation energy for high-resistance n-PbTe(Ga) ($E_a \sim 75$ meV).

The contribution of the high-resistance n-type regions to the conductivity may be very large and even dominant, both in the region of reverse biases and for low direct biases. The n-type regions are responsible for the high photosensitivity of the structure and for the residual photoconductivity. Rectification of the IVCs in the region of reverse biases is due to the change in the carrier density in the photosensitive n-type regions. After the illumination is switched off, the ohmic IVCs are completely determined by the conductivity of the n-type regions. The displacement of the IVC relative to the origin of the coordinates when the illumination is switched off is due to the effect of the nonohmic contact on which a photo-emf arises. Nonetheless, it is necessary to take into account the fact that the treatment of the structure as an equivalent circuit consisting of two resistances is extremely simplified, permitting only a qualitative description of the conduction process. In reality, regions with different types of conductivity are not ideally insulated, and they are separated by barriers whose height can be different as a result of fluctuations in the dopant distribution.

It is important to note that the properties of structures based on p-PbTe(Ga), which we investigated, are characteristic not only of samples synthesized by the procedure described above, but also of p-PbTe(Ga) single crystals grown under different conditions (for example, by using the vapor–crystal mechanism and the Czochralski method).[2] Diode structures based on such crystals possess nonlinear IVCs, but their photosensitivity in the region of reverse biases is much lower.

We wish to thank A. Trifonov for investigating the real structure of the crystals.

This work was sponsored by the Russian Fund for Fundamental Research (Grants Nos. 96-02-16275 and 96-02-18325).

[1] B. A. Akimov, A. V. Dmitriev, D. R. Khokhlov, and L. I. Ryabova, Phys. Status Solidi A **137**, 9 (1993).
[2] S. A. Belokon', L. N. Vereshchagina, I. I. Ivanchik, L. I. Ryabova, and D. R. Khokhlov, Fiz. Tekh. Poluprovodn. **26**, 264 (1992) [Sov. Phys. Semicond. **26**, 148 (1992)].
[3] E. P. Skipetrov, A. N. Nekrasova, D. V. Pelekhov, L. I. Ryabova, and V. I. Sidorov, Fiz. Tekh. Poluprovodn. **28**, 1626 (1994) [Semiconductors **28**, 906 (1994)].
[4] Z. G. Yanenko, V. I. Shtanov, and V. P. Zlomanov, Izv. Akad. Nauk SSSR, Neorg. Mater. **26**, 437 (1990).
[5] V. P. Zlomanov, V. I. Shtanov, and Z. G. Yanenko, Inventor's Certificate SSSR No. 1526872, September 15, 1989.
[6] A. B. Gas'kov, N. G. Lisina, V. P. Zlomanov, and A. V. Novoselova, Dokl. Akad. Nauk SSSR **261**, 95 (1981) [Sov. Phys. Dokl. **26**, 56 (1981)].
[7] F. F. Sizov, A. A. Sava, V. V. Teterkin, S. G. Bunchuk, and S. A. Belokon' Izv. Akad. Nauk SSSR, Neorg. Mater. **26**, 1193 (1990).

Translated by M. E. Alferieff

Annihilation of nonradiative recombination centers in GaAs/AlGaAs multiquantum well structures as a result of exposure to plasma

K. S. Zhuravlev,* V. A. Kolosanov, and I. I. Marahovka

Institute of Semiconductor Physics, Siberian Branch of the Russian Academy of Sciences, 630090 Novosibirsk, Russia

M. Holland

Department of Electronics and Electrical Engineering, University of Glasgow, Glasgow G12 8QQ, United Kingdom

(Submitted October 24, 1996; accepted for publication February 25, 1997)
Fiz. Tekh. Poluprovodn. **31**, 1436–1439 (December 1997)

The effect of exposure to a low-energy plasma (CF_4, Ar, Kr) on the photoluminescence properties of GaAs/AlGaAs multiquantum well structures is examined. It is shown that the photoluminescence of the quantum wells in the surface region is quenched after plasma exposure and the depth of this region increases with increase of exposure time. The photoluminescence intensity from the quantum wells located beyond this region increases. We associate these changes in the photoluminescence intensity with the effect of plasma-induced nonequilibrium point defects diffusing with anomalous rapidity into the depth of the structure. © *1997 American Institute of Physics.* [S1063-7826(97)00612-1]

Low-energy plasma processing is widely used in the preparation of low-dimensional structures and III–V-based semiconductor devices. During processing the ions of the plasma bombard the surface of the structures and modify the electronic and optical properties of the surface region of the structures.[1–4] In Refs. 5 and 6 it was established that plasma processing degrades photoluminescence in the surface region of *n*-GaAs layers and GaAs/AlGaAs quantum-well structures. In the present paper we investigate the effect of plasma processing on the photoluminescence properties of GaAs/AlGaAs quantum-well structures. It is shown that plasma exposure is followed not only by quenching of photoluminescence of the surface quantum wells, but also a rapid rise in photoluminescence of the quantum wells located a distance of several tens of nanometers from the surface.

Quantum-well structures were grown on GaAs (100) substrates by molecular-beam epitaxy. They consisted of a GaAs buffer layer of thickness 1.0 μm, an $Al_{0.3}Ga_{0.7}As$ layer of thickness 0.5 μm, and an array of quantum wells of various width, located within the first 200 nm from the surface. The structures were covered by a GaAs layer of thickness 10 nm. The B357 structure contained six quantum wells of width 2.2, 2.8, 3.4, 4.2, 5.6, and 8.5 nm, separated by barriers ($Al_{0.3}Ga_{0.7}As$) of width 24 nm; inside the 0.5-μm-thick $Al_{0.3}Ga_{0.7}As$ layer a short-period AlAs/GaAs superlattice was grown to prevent diffusion of impurities and point defects into the structure from the substrate.[7] The E138 structure contained five quantum wells of width 2.5, 3.1, 3.8, 5.2, and 8.5 nm with barriers ($Al_{0.3}Ga_{0.7}As$) of width 22 nm; in this structure the short-period superlattice was not grown in the $Al_{0.3}Ga_{0.7}As$ layer. The structures were processed in CF_4 plasma, which is usually used to remove SiO_2 and Si_3N_4 films in the preparation of semiconductor devices, and also in Ar or Kr plasma. The plasma power density was set equal to 0.5 W/cm^2, and the self-bias voltage was set to 400 V, and the pressure—to 0.07 Torr. In order to avoid heating the structures during prolonged plasma exposure, the discharge was extinguished every 120 s and the samples cooled. Photoluminescence was excited by a He–Ne-laser with power density 20 W/cm^2. The photoluminescence spectra were analyzed with an SDL-I monochromator and recorded with an FÉU-83 cooled photomultiplier working in the photon counting regime. During the measurements the samples were placed in an optical dewar with liquid nitrogen.

Figure 1 shows photoluminescence spectra of the B357 structure before and after plasma exposure. The photoluminescence peak with maximum at 1.507 eV is associated with the interband transition in the GaAs layer. The remaining six peaks correspond to transitions between the first electronic level and the first heavy-hole level ($1ehh$) in the quantum wells. In the initial structure the photoluminescence intensity of the quantum wells of width 2.2, 2.8, 3.4, 4.2, and 5.6 nm was high and roughly the same, which testifies to the small rate of nonradiative recombination in these quantum wells. The quantum well most removed from the surface (at 8.5-nm depth) had substantially lower photoluminescence intensity. After exposure in CF_4 plasma for 60 s the photoluminescence of the quantum well closest to the surface disappeared completely and the photoluminescence of the quantum wells at 3.4, 4.2, and 5.6 nm did not change, while the photoluminescence of the quantum well at 8.5 nm grew by a factor of more than 10 to the level of the remaining quantum wells. In the E138 structure, specially grown without a short-period AlAs/GaAs superlattice, the photoluminescence intensity of the quantum wells was low. After exposure to CF_4 plasma the photoluminescence intensity of all the quantum wells located more than 80 nm from the surface grew, as can be seen

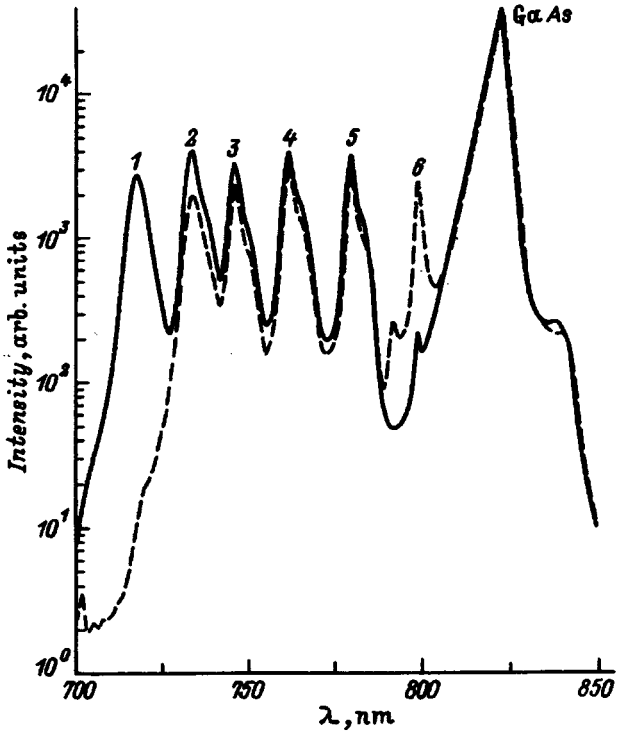

FIG. 1. Photoluminescence spectra of structure B357 before (solid line) and after (dashed line) exposure of the structure to CF_4 plasma for 60 s. $T=77$ K. Peaks *1–6* correspond to quantum wells with width 2.2, 2.8, 3.4, 4.2, 5.6, and 8.5 nm.

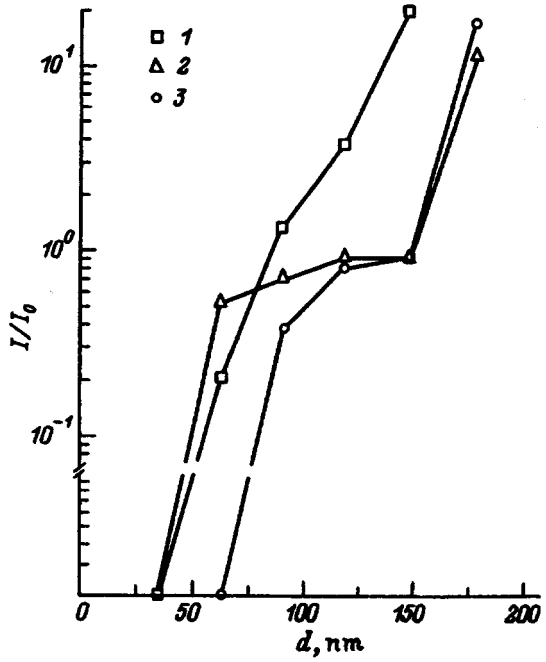

FIG. 3. Normalized photoluminescence intensity (I/I_0) of the structures B357 and E138 after exposure to plasma for 60 s versus the standoff distance from the surface of the structures to the quantum wells (d). *1*—E138, exposure in Ar, *2*—B357, exposure in Ar, *3*—B357, exposure in CF_4.

from Fig. 2, but to a different degree and to different final levels. Similar changes were also observed in the photoluminescence spectra in argon and krypton plasmas.

For these two structures Fig. 3 plots the photoluminescence intensity of the quantum wells after plasma exposure (I), normalized to the photoluminescence intensity of the quantum wells in the original sample (I_0), as a function of distance from the surface to the corresponding quantum well (d). The normalized photoluminescence intensity reflects changes in the concentration of the nonradiative recombination centers (NRC) in the quantum wells. As a reference for comparison, we used the photoluminescence spectrum of the GaAs layer, which is located at an adequate distance from the surface of the structure and which was not damaged during plasma processing. It can be seen from the figure that the normalized photoluminescence intensity grew most strongly in the quantum wells located at large distances from the surface, which testifies to the greater decrease of the NRC concentration in these quantum wells.

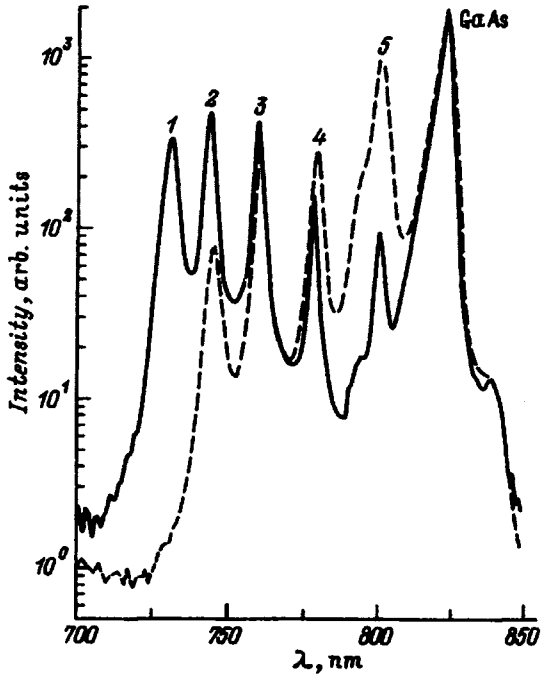

FIG. 2. Photoluminescence spectra of structure E138 before (solid line) and after (dashed line) exposure of the structure to CF_4 plasma for 60 s. $T=77$ K. Peaks *1–5* correspond to quantum wells with width 2.5, 3.1, 3.8, 5.2, and 8.5 nm.

The photoluminescence of the structures varied with the plasma exposure time. Figure 4 shows photoluminescence spectra, and Fig. 5 plots the normalized photoluminescence intensity, of the quantum wells of the E138 structure for different exposure times in CF_4 plasma. It is clear from these figures that as the exposure time was increased, the region in which the photoluminescence intensity fell broadened, and beyond the limits of this region the photoluminescence intensity grew insignificantly.

The data show that after plasma exposure two layers are formed in the structure, differing in their photoluminescence properties. In the first (the skin) layer photoluminescence of the quantum wells is quenched, while in the second (a deeper) layer the photoluminescence intensity of the quantum wells (weakly luminescing in the initial structures) grows. Increasing the plasma exposure time has an insignificant effect on the luminescence properties of the second layer. Changes in the photoluminescence intensity after

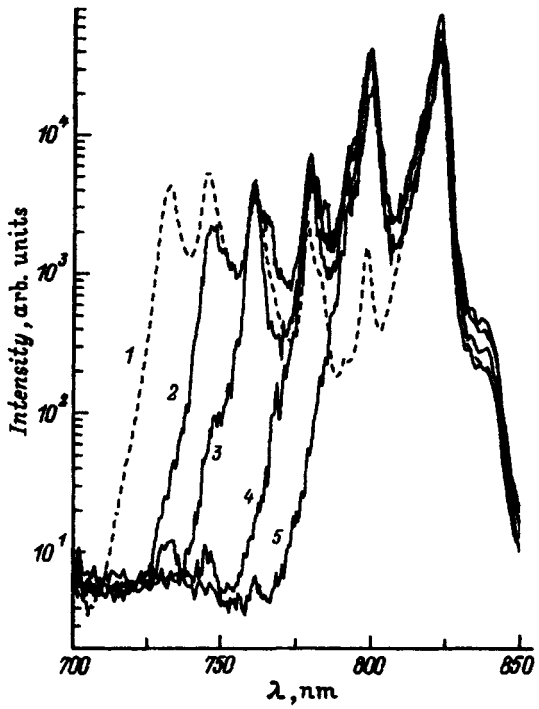

FIG. 4. Photoluminescence spectra of the structure E138 after different exposure times in CF_4 plasma, t_e, s: *1*—0, *2*—60, *3*—120, *4*—240, *5*—360. $T=77$ K.

plasma exposure of the structures show hardly any dependence on the nature of the plasma-forming gas—CF_4, Ar, and Kr, and consequently they bear no relation to the elements of the plasma introduced into the structure. We believe that the changes in the photoluminescence intensity are caused by nonequilibrium point defects which are formed in the surface region of the structures during plasma processing and diffuse with anomalous rapidity in the excited crystal,[8] with the diffusion coefficient of the one type of defect being at least an order of magnitude greater than that of the other. Our data show that the depth of the first damaged layer (l) is proportional to the square root of the exposure time, thus $l=(Dt)^{1/2}$, where D is the diffusion coefficient of the nonequilibrium defects ($d\simeq 10^{-12}$ cm^2/s) and t is the exposure time. It is likely that photoluminescence in the surface region is quenched by nonequilibrium vacancies, which are nonradiative recombination centers, while the photoluminescence intensity of the deeper quantum wells grows as a result of annihilation of vacancies introduced during growth by nonequilibrium interstitial atoms. If this assumption is valid, then the curves in Fig. 3 describe the distribution with thickness of the structures of the vacancies introduced during plasma processing ($d<80$ nm) and during growth ($d\geqslant 80$ nm). The small changes in the photoluminescence intensity of some of the quantum wells (weakly luminescing in the original structures) after plasma exposure can be explained by the fact that the low photoluminescence intensity of these quantum wells is determined not by point defects of the lattice but by nonradiative recombination centers associated with chemical impurities with which the nonequilibrium interstitial atoms interact only weakly.

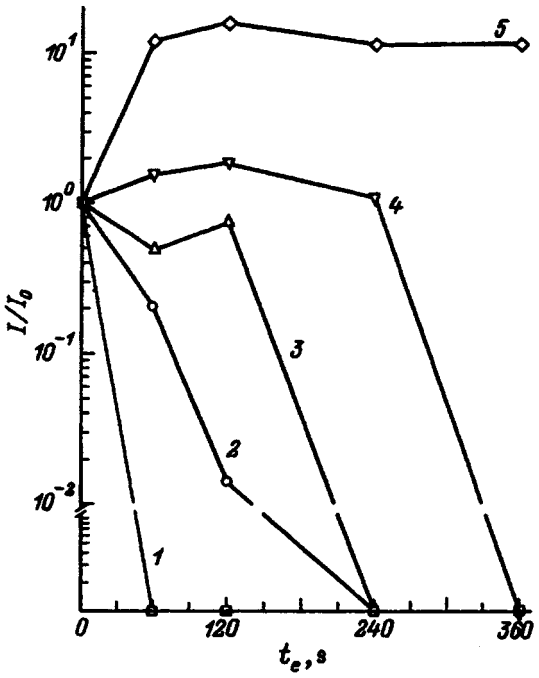

FIG. 5. Normalized photoluminescence intensity (I/I_0) of quantum wells of the structure E138 versus exposure time in CF_4 plasma, t_e. Dependences *1*–*5* correspond to quantum wells with width 2.5, 3.1, 3.8, 5.2, and 8.5 nm.

In summary, we have examined the effect of plasma processing on the photoluminescence properties of GaAs/AlGaAs quantum-well structures. We have shown that plasma processing leads to quenching of the photoluminescence of the quantum wells located in the surface region of the structure, and that the depth of this region increases with increase of the plasma exposure time. Beyond the limits of this region, the photoluminescence of the quantum wells grows after exposure to plasma. We believe that these changes in the photoluminescence intensity are caused by nonequilibrium point defects arising in the structures during plasma processing.

We thank M. R. Baklanov and L. A. Nenasheva for performing the plasma processing, and S. I. Chikichev for fruitful discussions of the results of this work.

*E-mail: Zhur@ispht.nsk.su Fax: 007-(383-2)-35-17-71

[1] A. V. Murel', A. P. Kasatkin, and V. M. Kogan, Izv. Ross. Akad. Nauk, Ser. Fiz. **56**, 161 (1992).
[2] W. Beinstingl, R. Christanell, J. Smoliner, C. Wirner, E. Gornik, G. Weimann, and W. Schlapp, Appl. Phys. Lett. **57**, 177 (1990).
[3] G. Juang, J. K. Hsu, I. S. Yen, and H. S. Shiau, J. Appl. Phys. **72**, 684 (1992).
[4] O. J. Glembocki, B. E. Taylor, and E. A. Dobisz, J. Vac. Sci. Technol. B **9**, 3546 (1991).
[5] H. W. Wong, D. L. Green, T. Y. Liu, D. G. Lishan, M. Bellis, E. L. Hu, P. M. Petroff, P. O. Holtz, and J. L. Mertz, J. Vac. Sci. Technol. B **6**, 1906 (1988).
[6] K. S. Zhuravlev, V. A. Kolosanov, V. G. Plyukhin, and T. S. Shamirzaev, Zh. Tekh. Fiz. **64**, 185 (1994) [Tech. Phys. **39**, 733 (1994)].
[7] P. M. Petroff, R. C. Miller, A. C. Gossard, and W. Wiegmann, Appl. Phys. Lett. **44**, 217 (1984).
[8] M. Lanno and J. Bourgoin, *Point Defects in Semiconductors* (Springer-Verlag, New York, 1981). p. 236.

Translated by Paul F. Schippnick

Photoluminescence of localized exitons in coherently strained ZnS–ZnSe/GaAs(001) quantum wells

V. V. Tishchenko, N. V. Bondar, and M. S. Brodyn

Institute of Physics, Ukrainian Academy of Sciences, 252022 Kiev, Ukraine

A. V. Kovalenko

Dnepropetrovsk State University, 320625 Dnepropetrovsk, Ukraine

(Submitted February 8, 1996; accepted for publication June 3, 1997)
Fiz. Tekh. Poluprovodn. **31**, 1440–1442 (December 1997)

The low-temperature photoluminescence (PL) of ZnS–ZnSe heterostructures grown in the form of single quantum wells (QW) by the non-conventional technology of photo-assisted vapor phase epitaxy has been investigated. It is shown that the inhomogeneity of the quantum wells can be explained in terms of a model based on disordering of the heterointerfaces. It is found that the mobility edge which separates the localized states from the delocalized states is 6 meV below the heavy-exciton ground state in the quantum wells with a nominal width $L_z = 11$ Å. © *1997 American Institute of Physics.* [S1063-7826(97)00812-0]

1. Superlattices and quantum wells based on the semiconductors ZnS and ZnSe are considered to be very promising for building lasers emitting in the blue-green region of the spectrum as well as various optoelectronic devices, including bistable elements.[1] The active region of such structures is provided by ZnSe layers in which an electron–hole gas is localized, bounded on either side by a potential barrier created by ZnS.

The characteristics of such a structure are determined mainly by the properties of the heterojunction separating the two chemically distinct materials of the quantum well. The simplest and most reliable means of estimating the quality of the heterojunction is to study its exciton photoluminescence, whose spectral shape and band widths are very sensitive to deviations of the heterojunctions from planarity.[2] The results of numerous studies based mainly on the technology of molecular-beam epitaxy (MBE) and metallo-organic chemical vapor deposition (MOCVD) have shown that disordering of the heterojunction causes inhomogeneous broadening of the exciton photoluminescence bands.[2–5] In the highest-quality structures the amplitude (δL_z) of the fluctuations of the thickness of the quantum wells (L_z) arising as a result of this disordering does not exceed one atomic monolayer.

In the present paper we analyze the exciton photoluminescence spectra of isolated ZnS–ZnSe quantum wells, grown by the relatively simple, cheap, and flexible method called PAVPE. The results obtained by this method indicate the formation of a tail of the density of localized states (LS), whose energy length is determined by the δL_z-dependent change in the energy of the exciton ground state. Analysis of the behavior of the photoluminescence bands, measured in different regions in the quantum-well plane as a function of the excitation power density (I_{exc}) and temperature (T) made it possible to determine the energy $E_c = 2.991$ eV corresponding to the mobility edge in the system of localized states.

2. We examined isolated quantum wells of ZnS (54 Å)–ZnSe (11 Å), grown on GaAs (001) substrates in a horizontal quartz reactor. The design of the reactor enables one to achieve a significant temperature gradient in the growth zone (25 °C/cm), which was established at low temperatures in the vicinity of 200 °C. As the starting materials we used only high-purity ZnS and ZnSe powders. A description of the details of the growth process can be found in Ref. 6. The obtained structures are coherently strained by virtue of the fact that the thicknesses of the corresponding layers are less than their critical values (~100 Å) for the appearance of lattice-mismatch dislocations. As a result, small δL_z do not cause any deformations in the quantum-well plane.

At the commencement of the experiment the samples were placed in a helium cryostat with regulated temperature T. Luminescence was excited by a continuous He–Cd laser beam with a wavelength of 325 nm and power equal to 10 mW. The photoluminescence was analyzed with a DFS-12 spectrometer linked up with a CAMAC system and a personal computer, and was recorded by an FEU-79 photomultiplier in the photon counting regime.

3. Curve *a* in Fig. 1 is the spectrum of the photoluminescence integrated over the surface of the sample (excitation spot diameter $d = 2$ mm of the order of the linear dimensions of the sample) and is typical of the investigated quantum wells in the region of their intrinsic absorption edge. The excitonic nature of the observed emission is confirmed by low-temperature measurements of the reflection, whose spectral dependence is shown by curve *e*. The spectra are shifted toward higher energies relative to their position known for bulk ZnSe. The short-wavelength shift (~188 meV) due to effects of the quantum well acting in one direction and elastic compression deformation arising due to lattice-mismatch between ZnSe/ZnS and GaAs. The deformation contribution to the observed shift is not greater than 5% (Ref. 7).

The position of the dominant photoluminescence band in spectrum *a* in Fig. 1 (energy of the maximum $E_m = 2.980$ eV corresponding to the wavelength 415.9 nm) varies insignificantly from sample to sample, and the band itself is asymmetric with pronounced steps whose nonequivalence allows one to reject the hypothesis that its limbs are formed as a

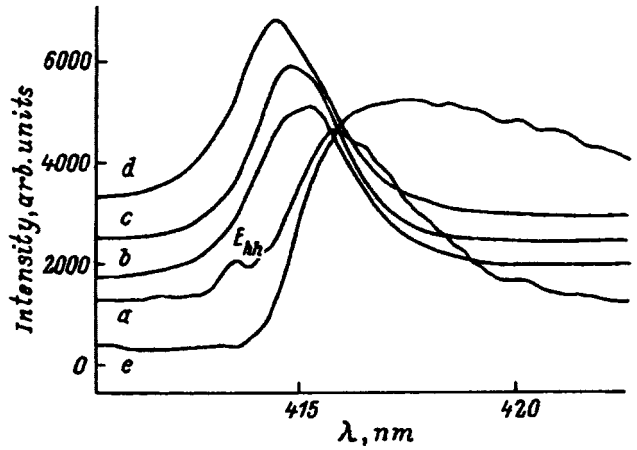

FIG. 1. Total (a) and local (b)–(d) photoluminescence and reflection (e) of ZnS–ZnSe quantum wells at $T=4.5$ K. Spectra $b-d$ were measured at different positions of the excitation spot on the surface of the sample. I_{exc} is 400 times larger for cases $-d$ than for case a. The spectra are shifted along the intensity axis for clarity.

result of transitions in which phonons participate. At the same time, the dependence of E_m on the position of the excitation spot (diameter $d=100$ μm) on the surface of the sample (spectra b, c, and d) provides a basis for linking the appearance of steps with the absence of homogeneity of the quantum wells.

Figures 2 and 3 plot the energy of the maximum, E_m, for different regions in the quantum-well plane as a function of I_{exc} and T. As a rule, with growth of I_{exc}, the photoluminescence peak is shifted toward higher energies, tending toward its limiting position at 2.991 eV. Here the degree of asymmetry of the band is increased due to growth of the length of its low-energy limb. A similar behavior is also observed for variation of T. However, there are segments of the surface for which $E_m=2.991$ eV$=$const for any I_{exc} and T within the investigated intervals. In this case, the asymmetry of the photoluminescence band is virtually independent of I_{exc}, and when T is increased is even slightly, it is restored due to quenching of the low-energy limb.

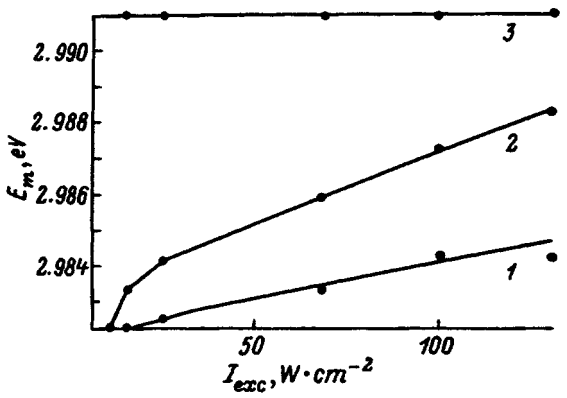

FIG. 2. Energy position (E_m) of the photoluminescence maximum plotted versus excitation intensity (E_{exc}). Curves *1–3* correspond to cases $b-d$ in Fig. 1. The points are the experimental data, the solid lines are drawn through the points.

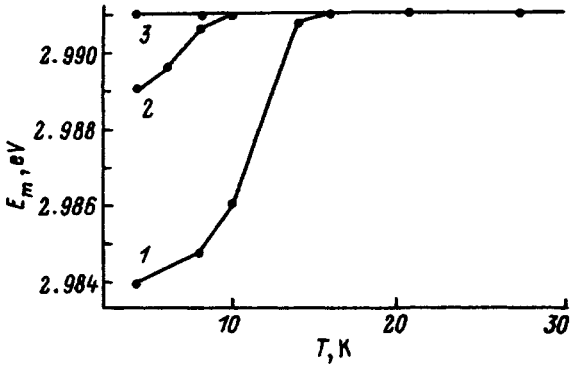

FIG. 3. Energy position (E_m) of the photoluminescence maximum plotted versus temperature (T). Curves *1–3* correspond to cases $b-d$ in Fig. 1. The points are the experimental data, the solid lines are drawn through the points.

The above results can be interpreted directly in terms of the model of excitons localized in a random potential arising as a result of the disorder at the heterojunction between the ZnS and ZnSe layers. This disorder, on the scale of the Bohr radius of the exciton (a_B), and the corresponding fluctuations of the width of the quantum wells unavoidably lead to the appearance of a two-dimensional well potential and the associated tail in the density of localized states, where the occupancy of this tail is described by Fermi–Dirac statistics.[8] The applicability of Fermi–Dirac statistics to excitons, which at sufficient separation behave like bosons, reflects the fact that by virtue of the internal structure of the considered quasiparticles, each individual potential well that arises can localize no more than one exciton in the case in which its characteristic spatial dimension (R_s) is comparable with a_B.

In light of the discussion above, the dependences plotted in Fig. 2 reflect the effect of an increase (decrease) in the absolute value of the chemical potential of the degenerate system of localized excitons with increase (decrease) of its density. It is clear that at sufficient excitation intensities I_{exc} the chemical potential can reach the mobility edge, which with further growth of excitation causes the delocalized states to be filled and, as a result, stabilizes the photoluminescence peak near E_c. The reason for such a stabilization resides in the transition to statistics with a quasiparticle distribution function which is independent of the quasiparticle density. The excitation level of the quantum wells necessary for this to occur, in contrast to the case with bulk crystals, is completely achievable in practice, due to the two-dimensional nature of the considered system.

From Fig. 2 we find that in our case E_c is equal to 2.991 eV. We can also state that the width of the photoluminescence band (35–40 meV at the 0.1 level) indicates that δL_z corresponds to one atomic monolayer.

The key question remains as to how E_c relates to the free exciton level. To obtain an answer to this question, it is necessary to compare photoluminescence with its excitation spectrum and/or with reflection data. In the absence of measurements on photoluminescence excitation, we turn our attention to the existence in the vicinity of the minimum of the

reflection curve of a weak photoluminescence peak (2.997 eV/413.5 Å), which is distinctly observable only in the surface-integrated spectrum and denoted as E_{hh} in Fig. 1a. To within the longitudinal–transverse splitting energy (1.5 meV for ZnSe; Ref. 9) the reflection minimum defines the exciton resonance frequency.[10] Therefore, we believe that the E_{hh} peak is a result of emission of free excitons in the regions of quantum wells having nominal width $L_z = 11$ Å (excitation over almost the entire surface of the sample and the small densities achievable as a result favor the observation of E_{hh}). Hence it follows that in the investigated samples the mobility edge is located 6 meV below the ground state energy of the hh exciton in a quantum well with $L_z = 11$ Å (the lh exciton level is located 200 meV above it[7]).

The question arises as to the nature of the delocalized states that form the emission in the interval between E_c and E_{hh} (this interval contains, for example, the entire low-energy limb of spectrum d in Fig. 1). Studies that have appeared in recent years show that these are exciton states in those quantum-well regions for which $R_s < a_B$ (Ref. 11). Inside each such region the excitons move freely and undergo scattering only at its boundaries.[12] On this basis, spectrum d corresponds to regions of the surface for which predominantly $R_s < a_B$.

Thus, we may speak of the inhomogeneity of our quantum wells both in the sense of disordering of the heterojunction and in the sense of inhomogeneity of the surface distribution function of R_s. This latter circumstance appears to be due to the transverse inhomogeneity of the PAVPE hydrogen fluxes delivering chemical reagents to the GaAs surface.

In conclusion, we note that the localized-states model enabled us to uniquely link the observed temperature dependence of the photoluminescence with activation of the localized excitons and transition of some of them to the delocalized states at $T = 15$ K. Here the abrupt dependence of E_m on T observed in such a small temperature interval is due to the exponentially fast variation of the density of localized states about the chemical potential (Ref. 8).

We are indebted to Prof. C. Klingshirn for fruitful discussions. The incorporation of PAVPE technology became possible thanks to cooperation with Dr. P. Lilley within the scope of NATO Linkage Project 071302.

This work was supported by INTAS Program 94-324 and also by the Ukrainian Foundation for Basic Research (Project No. 2.4/86).

[1] R. A. Reynolds, J. Vac. Sci. Technol. A **7**, 269 (1989).
[2] P. S. Kop'ev, I. N. Ural'tsev, D. R. Yakovlev, Al. L. Éfros, and A. V. Vinokurova, Fiz. Tekh. Poluprovod. **22**, 424 (1988) [Sov. Phys. Semicond. **22**, 259 (1988)].
[3] H. Kalt, J. Collet, S. D. Baranovskii, Rosari Saleh, P. Thomas, Le Si Dang, and J. Cibert, Phys. Rev. B **45**, 4253 (1992).
[4] T. Taguchi, Y. Kawakami, and Y. Yamado, Physica B **191**, 23 (1993).
[5] N. N. Ledentsov, S. V. Ivanov, V. M. Maksimov, I. V. Sedova, I. G. Tabatadze, and P. S. Kop'ev, Fiz. Tekh. Poluprovodn. **29**, 65 (1995) [Semiconductors **29**, 34 (1995)].
[6] A. V. Kovalenko and V. V. Tishchenko, Jpn. J. Appl. Phys. **34**, Suppl. 34-1,209 (1995).
[7] V. V. Tishchenko, Y. S. Partis, E. Anastassakis, and N. V. Bondar, Solid State Commun. **96**, 793 (1995).
[8] J. A. Kash, M. Zachau, E. E. Mendez, J. M. Hong, and T. Fukuzawa, Phys. Rev. Lett. **66**, 2247 (1991).
[9] S. Rudin and T. L. Reinecke, Phys. Rev. B **42**, 11 218 (1990).
[10] E. Tossati and G. Harbeke, Nuovo Cimento B **22**, 87 (1974).
[11] B. M. Askinadze, E. Cohen, Azra Ron, and L. Pfeiffer, Phys. Rev. B **47**, 10 613 (1993).
[12] H. Stolz, D. Schwarze, and W. von der Osten, Superlattices Microstruct. **6**, 271 (1989).

Translated by Paul F. Schippnick

Macroscopic, local, volume, charge-carrier states in quasi-zero-dimensional structures

S. I. Pokutniĭ

Ukrainian State Marine University, 327025 Nikolaev, Ukraine
(Submitted August 7, 1996; accepted for publication May 20, 1997)
Fiz. Tekh. Poluprovodn. **31**, 1443–1448 (December 1997)

A theory of size-quantization of charge carriers in a small semiconductor crystal under conditions where the polarization interaction plays a large role is constructed. The charge-carrier spectrum in a small microcrystal and its dependence on the radius of the microcrystal, the charge-carrier effective mass, and the relative permittivity are investigated. It is shown that the appearance of local states is of a threshold nature depending on the size of the microcrystal.
 [S1063-7826(97)01911-X]

The optical properties of quasi-one-dimensional structures, consisting of spherical semiconductor microcrystals (SMCs) with dimensions $a \simeq 1-10^2$ nm, dispersed in different transparent dielectric media have been widely investigated in recent years.[1–4] Such heterophase systems are a new object for the investigation of the quantum-well effects in semiconductors.

The strong nonlinearities of the optical characteristics and the short lifetimes of photoexcited charge carriers in quasi-zero-dimensional structures[1–4] make such nonuniform systems promising materials for producing new components for nonlinear optoelectronics (specifically, components that control optical signals).[3,4]

In the quasi-zero-dimensional structures studied, the microcrystal sizes a are comparable to the characteristic quasiparticle sizes in semiconductors. Under these conditions, the interface of a SCM can give rise to size-quantization of the quasiparticle energy spectrum of the microcrystal due to the purely spatial limitation of the region of quantization[5–7] and the polarization interaction of charge carriers with the SCM surface.[8–13] The optical properties of quasi-zero-dimensional structures are largely determined by the energy spectrum of charge carriers localized by electrostatic image forces near the interface between two different dielectric media.[8–13]

In Refs. 5 and 6 it was found that the structure of the absorption and luminescence spectra of the SMCs investigated was determined by size-quantization of the energy spectrum of free quasiparticles. The effect of the polarization interaction on the spectra of the charge carriers and on the spectra of large-radius excitons near a spherical interface between two different dielectric media was studied in Refs. 8–19.

In Refs. 20–23, the photoionization of CdS single crystals, grown in a silicate glass matrix, and CdS and TiO_2 SMCs placed in water solutions was investigated experimentally. It was established that a nonequilbrium electron produced by radiation corresponding to interband excitation leaves the volume of the SMC and is captured in a trap in the matrix. As a result, an excess charge carrier (hole) remains in the volume of the SMC.

In Ref. 8, a simple model of a quasi-zero-dimensional structure was used to analyze the conditions of charge-carrier localization near a spherical interface between two dielectric media. This model consists of a spherical SMC with radius a and permittivity ε_2, dispersed in a dielectric medium with permittivity ε_1. A quasiparticle with charge e and effective mass m moves in the crystal. As a result, an analytical expression was obtained for the polarization interaction $U(r,a)$, which arises in such a medium, between the charge carriers and a surface charge induced at the spherical interface between the two media with different permittivities. The interaction $U(r,a)$ depends on the relative permittivity $\varepsilon = \varepsilon_1/\varepsilon_2$; r is the distance of the charge carrier from the center of the microcrystal. For charge carriers moving near SMCs, there are two possibilities: 1) The polarization interaction results in attraction of the charge carriers to the surface of the SMC (for $\varepsilon < 1$—to the outer surface of the SMC and for $\varepsilon > 1$—to the inner surface of the SMC) and, correspondingly, in the formation of external surface[8–10] or internal surface[8,11] states; 2) for $\varepsilon < 1$ the polarization interaction gives rise to repulsion of charge carriers from the inner surface of the SMC and the appearance of local volume states (LVSs) in the SMC.[12,13]

In Ref. 8 it was also shown that as the radius a of the SMC decreases, a quantum-well effect, which impedes charge-carrier localization as a result of a relative decrease in the contribution of the potential energy compared with kinetic energy, appears. The smallest critical size a_c of a SMC, for which a local state appears is close to the average distance b_i (from the center of the SMC) of ground-state charge carriers above a flat interface

$$a_c \simeq b_i = 6\left|\frac{\varepsilon_2+\varepsilon_1}{\varepsilon_2-\varepsilon_1}\right| a_B^{(i)}, \tag{1}$$

where $a_B^{(i)} = \varepsilon_i \hbar^2/m_i e^2$ is the Bohr radius in a medium with permittivity ε_i and effective mass m_i $(i=1,2)$.

Since the expressions for the polarization potential $U(r,a)$ were obtained in Ref. 8 on the basis of macroscopic electrostatics, the above-indicated, local, charge-carrier states arising in the field of this potential are of a macroscopic character and for them $b_i \geqslant d$ (d is a distance of the order of the interatomic distance).

Until now, the effect of the boundary of a SMC on the spectrum of its single-particle states has not been studied adequately. In Refs. 12 and 13, the spectrum of LVSs was obtained only for the case of low-lying, oscillator-type states with arbitrary relative permittivity $\varepsilon < 1$. To compensate for this omission in the theory we will find the spectrum of LVS

for the charge carriers by using the WKB method with arbitrary values of the parameters of the quasi-zero-dimensional structure but for the case in which the difference in the permittivities of the adjoining media is large ($\varepsilon_2 \gg \varepsilon_1$ or $\varepsilon \ll 1$).

1. WKB CALCULATION OF THE SPECTRUM OF LOCAL VOLUME STATES

The expression for the polarization interaction potential $U(r,a)$ for a charge carrier interacting with the surface charge induced on a spherical interface between two different dielectric media (self-action potential) assumes the form for $\varepsilon \ll 1$ (Refs. 8 and 12)

$$U(x,S) = \frac{1}{S_2(1-x^2)} + \frac{\varepsilon_2}{S_2\varepsilon_1}. \tag{2}$$

Here and below, energy is measured in units of the Bohr energy in the $i=2$ medium:

$$Ry^{(2)} = \hbar^2/2m_2(a_B^{(2)})^2$$

and dimensionless lengths are used: $0 \leqslant x = r/a \leqslant 1$ and $S_2 = a/a_B^{(2)}$. The potential energy of the charge carriers in the volume of a small SMC

$$V_l(x,S_2) = U(x,S_2) + \frac{L^2}{S_2^2x^2} = \frac{1}{S_2(1-x^2)} + \frac{1}{S_2\varepsilon} + \frac{L^2}{S_2^2x_2} \tag{3}$$

has a minimum value

$$V_l^{\min}(S_2) = V_l(x=x_0,S_2) = \frac{1}{S_2}\left[\frac{1}{\varepsilon} + 4\left(\frac{(1-2\varepsilon)L^2}{2S_2}\right)^{1/2} + \frac{(1+\varepsilon)L^2}{2S_2}\right] \tag{4}$$

at the point $x=x_0$, where

$$x_0^2 = \left(\frac{1+2\varepsilon}{2}\right)^{1/2}\left(\frac{L^2}{S_2}\right)^{1/2} < 1. \tag{5}$$

The term $L^2/S_2^2x^2$ in the expression (3) determines the centrifugal energy of the charge carrier, and $L^2 = l(l+1)$, where l is the orbital angular momentum quantum number. According to the expression (5), the states are well-localized at the center of the SMC only if $(L^2/S_2)^{1/2} \ll 1$.

Just as in the case $\varepsilon < 1$, (Ref. 12 and 13), the formation of LVS is of a threshold character and is possible only in sufficiently large SMC, whose radius S_2 exceeds a critical value S_c.

Yost–Pais criterion[24]

$$S_2^2\int_0^1 U(x,S_2)(1-x)dx \geqslant (2l+1) \tag{6}$$

for charge-carrier states with radial quantum number $n_r=0$ and arbitrary l gives for the critical radius S_c of the SMC the expression

$$S_c = (2l+1)[\ln 2 + (1/2\varepsilon)]^{-1}. \tag{7}$$

The criterion (6) is only a necessary condition for the appearance of a bound state, and therefore it can underestimate S_c.

For small SMC radii $S_2 \ll S_c$, the charge-carrier states will be delocalized, since the kinetic (and centrifugal) energy ($\sim S_2^{-2}x^{-2}$) makes the dominant contribution. The charge-carrier spectrum $E_{nl}(S_2)$ (n is the principal quantum number) will coincide with the continuous (or quasidiscrete) spectrum

$$E_{nl}(S_2) = \varphi_{nl}^2/S_2^2, \tag{8}$$

which corresponds to ''free'' motion of charge carriers in an impenetrable spherical well [φ_{nl} are the roots of the Bessel function $J_{l+1/2}(\varphi_{nl})=0$].

For large SMC radii $S_2 \gg S_c$, states lying below the continuous spectrum can arise in the potential well $V_l(x,S_2)$ (3). In what follows, we shall term such low-lying, charge-carrier states LVSs. The size of the localization region of such states in the potential well (3) must be quite small compared with the radius S_2 of the SMC itself.

We shall use the WKB method to investigate the spectrum $E_{nl}(S_2)$ of local volume states for arbitrary values of the parameters of problem S_2, n, and l. The quantization rule can be represented in the form

$$\frac{2}{\pi}(1-u_1/u_2)(u_1)^{-1/2} \times \int_0^1 \frac{dzz^2\sqrt{1-z^2}}{[(u_2-1)/(1-u_1/u_2)+z^2]\sqrt{1-(1-u_1/u_2)z^2}} = \sqrt{\frac{2N^2}{3S}}. \tag{9}$$

Here $N = n_r + 1/2$ (Ref. 25). The variable

$$z^2 = 1 - (u_2^{-1} - u_2^{-1}x^2 - u_1u_2^{-1})/(1-u_1u_2^{-1}),$$

and $u_{1,2}$, which are associated with the turning points $x_{1,2}$ in the potential (3) by the expression $u_{1,2} = 1 - x_{1,2}^2$, are determined by the relations

$$\lambda_{Nl}(S) = \frac{6}{S_2}\left(\frac{1-u_1}{u_1} + \frac{L^2}{6S_2(1-u_1)}\right),$$

$$\frac{u_1}{u_2} = u_1 + \frac{L^2u_1^2}{6S_2(1-u_1)} \leqslant 1. \tag{10}$$

We shall measure the charge-carrier energy from the minimum value $V_l^{\min}(S_2)$ (4) of the energy. For this reason, in Eq. (10) we have

$$\lambda_{NL}(S_2) = E_{Nl}(S_2) - V_l^{\min}(S_2). \tag{11}$$

The quantity $(u_1/u_2)(u_1)$ (10) equals 1 for $u_1 = u_1^0 = [1 + (L^2/6S_2)]^{-1}$. Therefore, to satisfy the inequality $u_1/u_2 \leqslant 1$, it is necessary that

$$0 \leqslant u_1 \leqslant u_1^0 = \left[1 + \left(\frac{L^2}{6S_2}\right)\right]^{-1}. \tag{12}$$

If the following condition is satisfied:

$$1 - \frac{u_1}{u_2} = 1 - u_1 - \frac{L^2u_1^2}{6S_2(1-u_1)} \ll 1, \tag{13}$$

and assuming in the integrand in Eq. (9)

$$\sqrt{1-(1-u_1/u_2)z^2}\simeq 1,$$

we write the quantization rule (9) in the form

$$(1-u_1/u_2)u_1^{-1/2}\left[\frac{1}{2}+\frac{(u_2^{-1}-1)}{1-u_1/u_2}\times\left(1-\sqrt{1+\frac{1-u_1/u_2}{u_2^{-1}-1}}\right)\right]=\sqrt{\frac{2N^2}{3S}}. \tag{14}$$

We shall consider the case where

$$\frac{1-u_1/u_2}{u_2^{-1}-1}=\frac{6S_2(1-u_1)^2}{L^2u_1}-u_1\ll 1. \tag{15}$$

First, we assume

$$u_1\leqslant u_1^0\simeq 1-\sqrt{L^2/6S_2}<1. \tag{16}$$

As one can easily see, the solution of Eq. (14) is

$$u_1\simeq 1\sqrt{\frac{L^2}{6S_2}}\left(1+\sqrt{\frac{N}{L}}\right)^2. \tag{17}$$

The requirement that the relations (13), (15), and (16) hold simultaneously leads to the condition

$$2\sqrt{\frac{N}{L}}\ll 1\ll\sqrt{\frac{6S_2}{L^2}}. \tag{18}$$

The condition (18) holds for charge-carrier states with large orbital angular momentum quantum numbers L (such that $2\sqrt{N/L}\ll 1$). In this case, the charge carriers undergo motion in a SMC with large radii S_2 (such that $\sqrt{6S_2/L^2}\gg 1$).

The spectrum $\lambda_{Nl}(S_2)$ (11) with Eq. (17) in the range of parameters of the problem (S_2,N,L), which is determined by the condition (18), has the form

$$\lambda_{Nl}(S_2)=\omega_l(S_2)\left(\frac{1}{2}+\frac{N}{L}\right),$$

$$\omega_l(S_2)=4\sqrt{6}(L/S_2^{3/2}),\ \frac{N}{L}\ll 1. \tag{19}$$

The first term, which is proportional to $(L/S_2^{3/2})$, makes the main contribution to the spectrum $\lambda_{Nl}(S_2)$ (19) of local volume states. The second term in Eq. (19) is only a small correction (of the order of $N/S_2^{3/2}$). The spectrum $\lambda_{Nl}(S_2)$ (19) is an oscillator-type spectrum with the frequency $\omega_l(S_2)$ of charge-carrier oscillations.

We assume as before, that the conditions (13) and (15) hold, but now

$$u_1<u_1^0\simeq\sqrt{\frac{6S_2}{L^2}}<u_2\ll 1. \tag{20}$$

The solution of Eq. (14) under this condition is

$$u_1=\sqrt{\frac{6S_2}{L^2}}\sqrt{1-4\left(\frac{N}{L}\right)^{1/2}\left(\frac{L^2}{6S^2}\right)}. \tag{21}$$

The requirement that the conditions (13), (15), and (20) hold simultaneously reduces to the inequalities

$$\left(\frac{16N}{L}\right)^{2/3}\ll\left(\frac{6S_2}{L^2}\right)^{1/2}\ll 1. \tag{22}$$

The spectrum $\lambda_{Nl}(S_2)$ (11) of local volume states, with allowance for Eq. (21) in the range of parameters of the problem which are determined by the conditions (22), is

$$\lambda_{Nl}(S_2)=\frac{L^2}{S_2^2}\left[1+\left(\frac{6S_2}{L^2}\right)^{1/2}\right]. \tag{23}$$

It should be noted that the spectrum $\lambda_{Nl}(S_2)$ (23) is determined mainly by a dependence of the form $\lambda_{Nl}(S_2)\sim L^2/S_2^2$, which is a particular case of the S_2 dependence of the spectrum $\lambda_{Nl}(S_2)$ (8). The latter spectrum is characteristic of charge carriers executing a finite motion in a spherical potential well with impenetrable walls. The second term makes only a small correction to the spectrum (23).

Let us examine the case where the conditions (13) and (16), as well as the condition

$$\left(\frac{1-u_1u_2^{-1}}{u_2^{-1}-1}\right)^{1/2}\gg 1, \tag{24}$$

hold. Then Eq. (14) has the solution

$$u_1=1-\sqrt{\frac{2N^2}{3S_2}}\left(1+\sqrt{1+\frac{L^2}{4N^2}}\right). \tag{25}$$

The requirement that the inequalities (13), (16), and (24) hold simultaneously reduces to the conditions

$$1\ll 1\frac{N}{L}\ll\sqrt{\frac{6S_2}{L^2}}, \tag{26}$$

which are satisfied for states with large quantum numbers N $(2N/L\gg 1)$ for large microcrystal sizes S_2 $(\sqrt{6S_2/L^2}\gg 1)$. In the range of parameters (S_2,N,L), which is determined by the inequalities (26), the spectrum $\lambda_{Nl}(S_2)$ (11) with Eq. (25) is of an oscillator form

$$\lambda_{Nl}(S_2)=\omega_l(S_2)\left(\frac{1}{2}+\frac{L}{N}\right),$$

$$\omega_l(S_2)=4\sqrt{6}(N/S_2^{3/2}),\quad L/N\ll 1, \tag{27}$$

with charge-carrier oscillation frequency $\omega_l(S_2)$.

It should be underscored that Eqs. (19), (23), and (27) are particular cases of the more general formulas (10), which describe an oscillator-type spectrum of the low-lying local volume states of the charge carriers.

Let us consider the case

$$\frac{u_1}{u_2}=u_1+\frac{L^2u_1^2}{6S_2(1-u_1)}\ll 1. \tag{28}$$

Assuming that in the integrand in Eq. (9) $\sqrt{1-(1-u_1u_2^{-1})z^2}\simeq\sqrt{1-z^2}$, the quantization rule (9) can be reduced to the expression

$$u_1^{-1/2}(1-u_1/u_2)\left[1-\sqrt{\frac{u_2^{-1}-1}{1-u_1/u_2}}\tan^{-1}\sqrt{\frac{1-u_1/u_2}{u_2^{-1}-1}}\right]=\frac{\pi}{2}\sqrt{\frac{2N}{3S_2}}. \tag{29}$$

Let the condition

$$\sqrt{\frac{1-u_1/u_2}{u_2^{-1}-1}}=u_1^{1/2}\sqrt{\frac{6S_2}{L^2}\left(\frac{1-u_1}{u_1}\right)^2}-1\ll\frac{1}{2} \tag{30}$$

hold, in addition to the inequalities (28). Expanding the expression (29) in a series in powers of the parameter (30) and retaining the first two terms of the expansion, we obtain for u_1

$$u_1=\left(\frac{6S_2}{L_2}\right)^{2/3}\left(\frac{2}{3\pi^2}\frac{S_2}{N^2}\right)^{1/3}\ll 1. \tag{31}$$

The inequalities (28) and (30) together reduce to the condition

$$\frac{1}{\sqrt{3}}\left(\frac{6S}{L^2}\right)^{1/2}<\left(\frac{3\pi N}{L}\right)^{2/3}\ll\frac{1}{\sqrt{3}}, \tag{32}$$

which holds for states with large values of the orbital angular momentum quantum number L such that

$$\sqrt{6S_2/L^2}\ll 1 \quad \text{and} \quad (3\pi N/L)^{2/3}\ll 1.$$

In the region of parameters (S_2, N, and L) determined by the conditions (31) and (32), the charge carriers move in the potential $U(u_1,S_2)\sim(L^2/6S_2)(1+u_1)$. Since this potential is a linear function of the variable u_1, $U(u_1,S_2)\sim u_1$, the spectrum $\lambda_{Nl}(S)$ (11) of the local volume states is, taking into account Eq. (31),

$$\lambda_{Nl}(S)=\frac{L^2}{S^2}\left[1+\left(\frac{3\pi N}{L}\right)^{2/3}\right],\ \left(\frac{3\pi N}{L}\right)^{2/3}\ll 1 \tag{33}$$

and has the same dependence on the quantum numbers N and L, i.e., $\lambda_{Nl}(S)\sim(N/L)^{2/3}$, as in the case of the charge carriers moving in a central field of the form $U(u_1)\sim u_1$.[26]

If the inequality

$$\sqrt{\frac{1-u_1/u_2}{u_2^{-1}-1}}=u_1^{1/2}\sqrt{\frac{6S}{L^2}\left(\frac{1-u_1}{u_1}\right)-1}\gg 1 \tag{34}$$

holds, in addition to the inequalities (28), then the substitution

$$\tan^{-1}\sqrt{\frac{1-u_1u_2^{-1}}{u_2^{-1}-1}}\approx\frac{\pi}{2}$$

can be made in Eq. (29).

In this case

$$u_1=\frac{4}{\pi^2}\left(\frac{6S}{L^2}\right)\left(1+\frac{2N}{L}\right)^{-2}\ll 1. \tag{35}$$

The requirement that the conditions (28) and (34) hold together reduces to the inequalities

$$\pi^2\left(\frac{1}{2}+\frac{N}{L}\right)^2\gg 1\gg\frac{4}{\pi^2}\left(\frac{6S}{L^2}\right)\left(1+\frac{2N}{L}\right)^{-2}. \tag{36}$$

In the region (36) the spectrum $\lambda_{Nl}(S)$ (11) of the local volume states is, taking into account Eq. (35),

$$\lambda_{Nl}(S_2)=\frac{\pi^2N^2}{S^2}\left(1+\frac{N}{L}\right)+\frac{L^2}{S_2^2};\frac{N}{L}\ll 1. \tag{37}$$

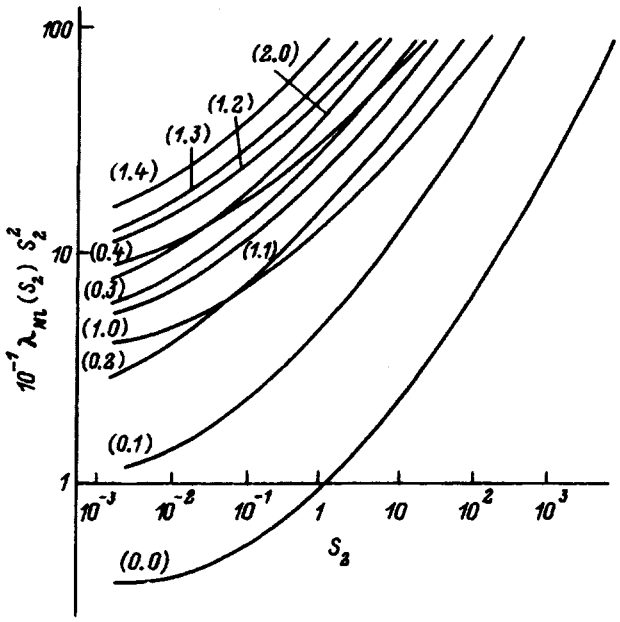

FIG. 1. Spectrum $\lambda_{Nl}(S_2)$ of local volume states as a function of the radius S_2 of a small semiconductor microcrystal. The numbers on the curves represent the states (n_r,l).

In other words, it takes on the same form as the spectrum of a particle undergoing a finite motion in a spherical potential well (8) of infinite depth.

Using the quantization rule (9), we obtain above the spectrum $\lambda_{Nl}(S_2)$ (11) of local volume states under the conditions (18), (22), (26), (32), and (36) for the parameters N, l, and S_2. Evidently, for $S_2\ll S_c\simeq 1$ (just as in the case of the outer and inner surface states[8–11]) the spectra $\lambda_{Nl}(S_2)$ (23), (33), and (37) of the local volume states are the spectrum $\lambda_{Nl}(S_2)\sim S_2^{-2}$ of a particle executing a finite motion in an infinitely deep spherical well. In the other limiting case, determined by the conditions (18) and (26), $S_2\gg S_c\simeq 1$, the spectra (19) and (27) of the local volume states are of an oscillator character $\lambda_{Nl}(S_2)\sim S_2^{-3/2}$ (Refs. 12 and 13).

Thus, for arbitrary parameters (S_2, N, l) of the problem the WKB charge-carrier spectrum $\lambda_{Nl}(S_2)$ (11) in the volume of a small semiconductor microcrystal of radius S_2 assumes the form $\lambda_{Nl}(S_2)\sim S_2^{-j(S_2)}$. The parameter $j(S_2)=2$ for $S_2\ll 1$ and for $S_2\gg 1$ $j(S_2)=3/2$, the same value as in the case of the low-lying local volume states.[12,13]

The numerical calculations of $\lambda_{Nl}(S_2)$ [Eqs. (9)–(11)], which are presented in Fig. 1, also confirm the dependence $\lambda_{Nl}(S_2)\sim S_2^{-j(S_2)}$. The figure presents the spectra $\lambda_{Nl}(S_2)$ (11) of local volume states with the quantum numbers $n_r=0$, 1, 2, 3, and 4 and $l=0$, 1, 2, 3, and 4 as a function of the size S_2 of microcrystals with radii ranging from $S_2=10^{-3}$ up to $S_2=10^3$. It follows from the computational results presented above that the effect of the boundary of a microcrystal on the spectrum of charge carriers moving in infinitely deep spherical well of radius S_2 reduces to quantum-well effects associated with purely spatial limitation of the region of quantization only for microcrystals of sizes $S_2\leqslant 10^{-2}$. For microcrystals with radii $S_2\geqslant 10^{-1}$ the charge-carrier spectrum $\lambda_{Nl}(S_2)$ (11) is determined mainly by the polarization

interaction of the charge with the spherical interface between two dielectric media. For large microcrystals with $S_2 \geqslant 10^2$ the charge-carrier spectrum is of an oscillator character $\lambda_{Nl}(S_2) \sim S_2^{-3/2}$.

The interband absorption spectra of cadmium sulfide ($\varepsilon_2 \approx 9.3$) SMCs with size a ranging from 15 to 300 Å dispersed in a transparent dielectric matrix ($\varepsilon_1 \approx 1.5$) were investigated experimentally in Ref. 6. It was found that the structure of the luminescence and absorption spectra of the SMCs is determined by size-quantization of the electron energy spectrum. In the range of SMC sizes $a \leqslant 40$ Å, in Ref. 6 an electron energy spectrum $E(a)$, whose dependence on the SMC radius a was different from the size-quantization form Eq. (8), was observed. The electron spectrum $E(a)$, obtained under the experimental conditions of Ref. 6, is described qualitatively by a function of the form $E_{1/2,0} = f(a^{-1}, a^{-3/2})$, determined by Eqs. (11), (4), and (27).

The dependence of the electron spectrum in quantum-well cadmium sulfide SMCs on the SMC radius a was investigated theoretically in Refs. 27–29. The calculations of the electron energy spectrum performed in Refs. 27–29, which allow for degeneracy of the valence band in the cadmium sulfide SMC under the experimental conditions of Ref. 6, show a small deviation (of the order of 6%) from the electron spectrum $E_{1/2,0}(a)$ described by Eqs. (11), (4), and (27).

In summary, our disregard of the corrections due to the degeneracy of the valence band in a small SMC, for the electron spectrum $E_{1/2,0}(a)$ given by Eqs. (11), (4), and (27) has apparently been justified.

We thank V. M. Agranovich and N. A. Efremov for a discussion of the results.

[1] A. Ekimov and Al. Efros, Phys. Status Solidi B **150**, 627 (1988).
[2] V. Gribkovskii, V. Zyulkov, and A. Kazachenko, Phys. Status Solidi B **150**, 641 (1988).
[3] U. Woggon and F. Henneberder, Phys. Status Solidi B **150**, 641 (1988).
[4] N. R. Kulish, V. P. Kunets, and M. P. Lisitsa, Ukr. Fiz. Zh. **35**, 200 (1990).
[5] A. I. Ekimov and A. A. Onushchenko, JETP Lett. **34**, 345 (1981).
[6] A. I. Ekimov and A. A. Onushchenko, JETP Lett. **40**, 1136 (1984).
[7] Al. A. Éfros and A. L. Éfros, Fiz. Tekh. Poluprovodn. **16**, 1209 (1982) [Sov. Phys. Semicond. **16**, 772 (1982)].
[8] N. A. Efremov and S. I. Pokutniĭ, Fiz. Tverd. Tela (Leningrad) **27**, 48 (1985) [Sov. Phys. Solid State **27**, 27 (1985)].
[9] N. A. Efremov and S. I. Pokutniĭ, Fiz. Tverd. Tela (Leningrad) **32**, 2921 (1990) [Sov. Phys. Solid State **32**, 1697 (1990)].
[10] N. A. Efremov and S. I. Pokutniĭ, Fiz. Tverd. Tela (Leningrad) **33**, 2845 (1991) [Sov. Phys. Solid State **33**, 1607 (1991)].
[11] S. I. Pokutnyi and N. A. Efremov, Phys. Status Solidi B **165**, 109 (1991).
[12] S. I. Pokutnyi, Phys. Status Solidi B **172**, 573 (1992).
[13] S. I. Pokutniĭ, Fiz. Tverd. Tela (St. Petersburg) **35**, 257 (1993) [Sov. Phys. Solid State **35**, 129 (1993)].
[14] N. A. Efremov and S. I. Pokutniĭ, Fiz. Tverd. Tela (Leningrad) **32**, 1637 (1990) [Sov. Phys. Solid State **32**, 955 (1990)].
[15] S. I. Pokutniĭ, Fiz. Tekh. Poluprovod. **25**, 628 (1991) [Sov. Phys. Semicond. **25**, 381 (1991)].
[16] S. I. Pokutniĭ, Fiz. Tverd. Tela (Leningrad) **34**, 2386 (1992) [Sov. Phys. Solid State **34**, 1278 (1992)].
[17] S. I. Pokutniĭ, Fiz. Tekh. Poluprovodn. **30**, 1952 (1996) [Semiconductors **30**, 1015 (1996)].
[18] S. I. Pokutnyi, Phys. Lett. A **168**, 433 (1992).
[19] S. I. Pokutnyi, Phys. Status Solidi B **173**, 607 (1992).
[20] V. Ya. Grabovskiĭ, Ya. Ya. Dzenis, and A. I. Ekimov, Fiz. Tverd. Tela (Leningrad) **31**, 272 (1989) [Sov. Phys. Solid State **31**, 149 (1989)].
[21] D. Chepic, A. Efros, and A. Ekimov, J. Lumin. **47**, 113 (1990).
[22] T. Kutzynski and J. Thomas, Chem. Phys. Lett. **88**, 445 (1982).
[23] D. Duoghong and J. Ransden, J. Am. Chem. Soc. **104**, 2977 (1982).
[24] A. I. Byaz', Ya. B. Zal'dovich, and A. M. Perelomov, *Scattering, Reactions, and Decay in Nonrelativistic Quantum Mechanics* [in Russian], Nauka, Moscow, 1971.
[25] L. D. Landau and E. M. Lifshitz, *Quantum Mechanics*, Pergamon Press, N. Y. [Russian original, Nauka, Moscow, 1974].
[26] S. Flügge, *Practical Quantum Mechanics*, Springer-Verlag, Berlin, 1971 [Russian translation, Nauka, Moscow, 1973, Vol. 1].
[27] G. V. Grigoryan, A. V. Rodina, and A. L. Efros, Fiz. Tverd. Tela (Leningrad) **32**, 3512 (1990) [Sov. Phys. Solid State **32**, 2037 (1990)].
[28] T. Richard, P. Lefebvre, and H. Mathieu, Phys. Rev. B **53**, 7287 (1996).
[29] Al. L. Efros, M. Rosen, and M. Kuno, Phys. Rev. B **54**, 4843 (1996).

Translated by M. E. Alferieff

Metastability and relaxation processes in hydrogenated amorphous silicon

B. G. Budaguan, A. A. Aĭvazov, M. N. Meĭtin, and A. Yu. Sazonov

Moscow Institute of Electronic Engineering (Technical University), 103498 Moscow, Russia

A. E. Berdnikov and A. A. Popov

Institute of Microelectronics, Russian Academy of Sciences, 150007 Yaroslavl, Russia
(Submitted January 14, 1997; accepted for publication February 13, 1997)
Fiz. Tekh. Poluprovodn. **31**, 1449–1454 (December 1997)

The kinetics of structural relaxation in hydrogenated amorphous silicon (*a*-Si:H) deposited by various methods is investigated by differential scanning calorimetry. The experimental results are used to analyze the nature of the metastable states in *a*-Si:H and to investigate the relationship between structural relaxation and light-induced metastability (the Staebler-Wronski effect). © *1997 American Institute of Physics.* [S1063-7826(97)02311-9]

INTRODUCTION

Hydrogenated amorphous silicon (*a*-Si:H) is currently used in the fabrication of photosensitive devices (photodetectors, sensors, and solar cells). However, more universal application of this material is deterred by the low stability of its electronic properties as a result of relaxation processes.[1]

Another obstacle to the full-scale manufacture of instruments utilizing *a*-Si:H is the low rate of deposition of device-quality material (1–2 Å/s). Any increase in the deposition rate produces microstructural inhomogeneities, which lead to structural relaxation and degradation of the electronic properties. However, the role of microstructural inhomogeneity remains as enigmatic as ever, but even material obtained in a setting with optimal technological parameters is known to contain microstructural inhomogeneities (microvoids, columns, and clustered hydrogen).[2–4]

Several authors have employed differential scanning calorimetry (DSC, Refs. 5–8) and differential thermal analysis (DTA, Ref. 9) to investigate processes in the structure of disordered alloys of tetrahedral semiconductors. The efficacy of these methods has been demonstrated in an analysis of relaxation processes in the temperature range 100 –300 °C (Refs. 5,6, and 9 and hydrogen effusion at $T>300$ °C (Refs. 5–9). At the same time, there are still unanswered questions concerning the nature of the low-temperature exothermic heat-flow process and the sign (exothermic or endothermic) of the high-temperature heat-flow process. It has been shown that the difference in the sign of the high-temperature process in the alloys *a*-Ge:H and *a*-CSiGe:H is attributable to differences in the DSC procedure and apparatus used for the analysis.[7] On the other hand, difficulties are encountered in the quantitative analysis of these results[8] owing to the simultaneous occurrence of several processes in the same temperature range (endothermic hydrogen effusion and exothermic structural transformation).[5,7]

Here we report a DSC investigation of the kinetics of structural relaxation in *a*-Si:H deposited by various techniques. The experimental results are used to analyze the nature of the metastable states in *a*-Si:H; pursuant to this objective, the relationship between structural relaxation and light-induced metastability (the Staebler-Wronski effect) is investigated in *a*-Si:H films prepared by plasma-chemical deposition from the gaseous phase with various technological parameters.

EXPERIMENTAL

Hydrogenated amorphous silicon films were prepared by dissociating mixtures ($10\%SiH_4+90\%H_2$) and ($5\%SiH_4+95\%He$) in a high-frequency (13.56 MHz) glow discharge at a specific discharge power of 0.3 W/cm^2 with a substrate temperature in the range 200–310 °C. Fast-grown *a*-Si:H films were obtained by deposition from pure monosilane in a low-frequency glow discharge (excitation frequency 55 kHz) at a power of 200 W, a substrate temperature of 225 °C, and a pressure in the range 55–95 Pa. After deposition the films were subjected to a 0.5-h anneal at a temperature of 240 °C and pressure of 10^{-3} Pa to eliminate unmanageable impurities (O, N, and C), whose concentrations were monitored by Auger analysis according to the film thickness.

The films were deposited on substrates of Corning 7059 glass for measurements of the Staebler–Wronski effect and also on silicon single-crystal substrates for DSC and infrared spectroscopy. For the DSC measurements a sample of mass 10 mg was prepared in powder form by scraping the films mechanically from the substrate and transferring the powder into sealed aluminum cells.

Quantitative DSC measurements were performed by the heat-flow method on a Du Pont DSC 910 microcalorimeter at a constant heating rate of 5–50 °C/min in the temperature range from 20 °C to 570 °C in an argon atmosphere. Each analysis was preceded by recording of the heating curve for the empty cell, and the resulting plot then served as the baseline.

The IR transmission spectra of the *a*-Si:H films were measured on a SPECORD M-80 dual-beam spectrometer. The 630-cm^{-1} band was used to calculate the bound hydrogen concentration.[10] The structural inhomogeneity of the

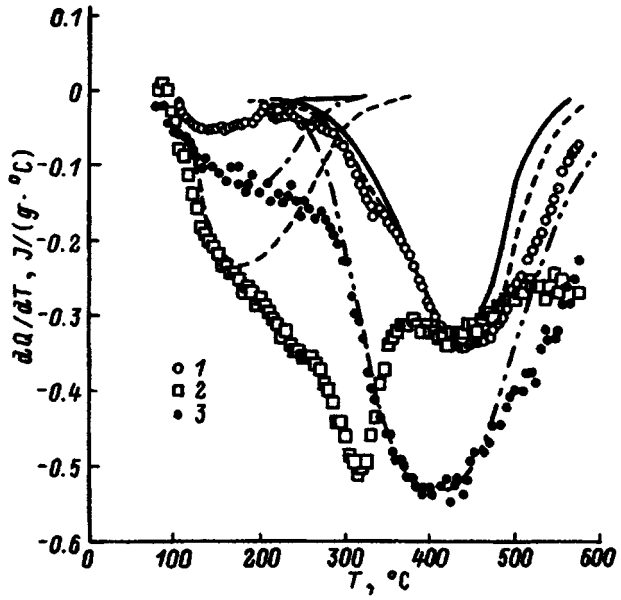

FIG. 1. Differential scanning calorimetry curves for *a*-Si:H films prepared by the glow-discharge dissociation of mixtures: *1*) [SiH_4+H_2], 13.56 MHz; *2*) [SiH_4+He], 13.56 MHz; *3*) [SiH_4], 55 kHz. The curves are plotted from modeling of the low-temperature and high-temperature exothermic transitions.

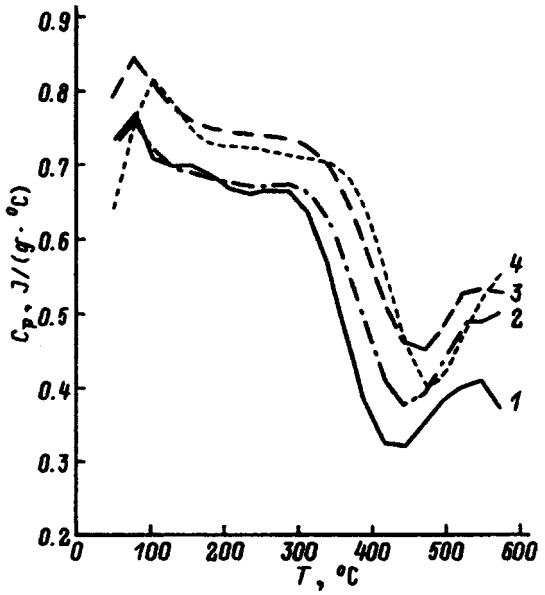

FIG. 2. DSC curves for *a*-Si:H films deposited from a gaseous mixture 10%H_4+90%H_2 at various heating rates: *1*) 5 °C/min; *2*) 10 °C/min; *3*) 20 °C/min; *4*) 50 °C/min.

films was estimated by means of the microstructure parameter

$$R=\frac{I_{2100}}{I_{2000}+I_{2100}},$$

where I_{2000} and I_{2100} are the absorption intensity integrals in the 2000-cm^{-1} and 2100-cm^{-1} bands.

The Staebler–Wronski effect was measured on structures with coplanar aluminum electrodes deposited on the surface of an *a*-Si:H film and subjected to a 0.5-h anneal at 200 °C. The linearity of the current-voltage characteristics of the samples confirmed that the measurement results were not influenced by the contacts and surface band bending. The samples were illuminated with a He-Ne laser ($\lambda=633$ nm), and the intensity of the incident beam was 10^{17}photons/(cm·s). The applied electric field was 10 V/cm. The defect generation kinetics was measured at temperatures of 80–150 °C in a two-hour radiation exposure.

RESULTS

The DSC curves for *a*-Si:H films annealed with various parameters are shown in Fig. 1. The curves clearly exhibit a low-temperature exothermic transition (LTT) beginning at 100 °C. At higher temperatures we observe two high-temperature exothermic transitions (HTTs) at 320 °C and 420 °C for *a*-Si:H films deposited from helium-diluted monosilane and one HTT near 420 °C for all other *a*-Si:H films.

Figure 2 shows the DSC curves for *a*-Si:H deposited from a gaseous mixture (90%H_2+10%SiH_4) at various heating rates: 5 °C/min, 10 °C/min, 20 °C/min, and 50 °C/min. All the curves contain a relatively weak LTT in the temperature interval 120–280 °C and a strong HTT at 420–430 °C. An increase in the heating rate raises the temperature at which the transition begins (see Table I), attesting to its kinetic nature. The total heat liberated in the region of the LTT increases slightly with the heating rate, consistent with the heating-rate dependence of the DSC signal. The decrease in the total heat in the region of the HTT is associated with the shift of this region toward temperatures exceeding the measurement limit of our equipment.

The DSC curves for *a*-Si:H deposited from a gaseous mixture (5%SiH_4+95%He) at a heating rate of 10 °C/min are shown in Fig. 3. The baseline has been subtracted from the curves. The curves exhibit the following characteristics distinct from those in Fig. 2: a) the LTT is uniformly distributed in the temperature range above 100 °C; b) two HTT peaks exist at 315 °C and 420 °C.

DISCUSSION AND MODEL

At temperatures above 100 °C the low-temperature exothermic transition is detected earlier in different alloys: *a*-SiGe:H (Ref. 5), *a*-Si:H (Ref. 8), *a*-SiC:H (Ref. 6), *a*-SiGe:H and *a*-CSiGe:H (Ref. 7), and *a*-$Si_{1-x}N_x$:H (Ref. 9), and also in nonhydrogenated *a*-Si and *a*-Ge (Ref. 5). In all these cases the samples were characterized by

TABLE I. Heating-rate dependence of the temperature T_{st} of the start of thermal effects and their total heats of reaction Q in *a*-Si:H films deposited from a gaseous mixture (10%H_4+90%H_2).

Heating rate, °C/min	T_{st}, °C		Q, J/g	
	Type of effect			
	LTT	HTT	LTT	HTT
5	80	310	18.2	84.6
10	90	325	18.3	65.7
20	100	350	24	62.0
50	115	375	24.9	58.0

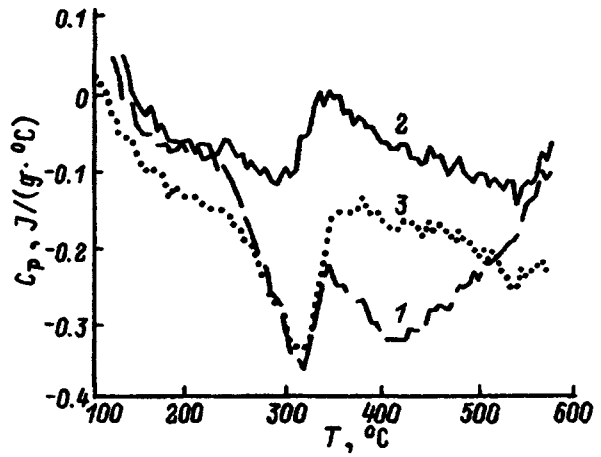

FIG. 3. DSC curves for *a*-Si:H films deposited from a gaseous mixture 5%SiH_4+95%He at various substrate temperatures: *1*) T_s=20 °; *2*) 175 °C; *3*) 305 °C.

structural inhomogeneity and, in some cases, by a distinct island structure observed with the aid of a transmission electron microscope (TEM).[5,9]

The structural inhomogeneity of our investigated films deposited from hydrogen-diluted monosilane has also been detected previously in the TEM.[9] It has been shown in the literature that the inhomogeneities (microscopic voids, etc.) originate from secondary reactions in the plasma and from the dominant role of SiH_2 radicals in the film growth process.[11] It has also been shown[12] that the microstructure of films deposited from monosilane weakly diluted with helium is inhomogeneous as well. Finally, the structural inhomogeneity of *a*-Si:H films deposited from these mixtures is corroborated by the high value of the parameter *R* (Table II) obtained from IR spectroscopy data. Consequently, the presence of the LTT on the DSC curves of our samples is also attributable to the structural inhomogeneity of the films.

A distinctive feature of this kind of microstructure is a high fraction of internal boundaries containing weak Si–Si bonds and hydrogen clusters of the SiH_2 or SiH type.[5,9] According to our calculations, the density of weak Si–Si bonds situated at internal boundaries is $(4\pm1)\times10^{20}$ cm^{-3} in *a*-Si:H films deposited from hydrogen-diluted monosilane.[9] It has also been shown in the same paper that relaxation of the weak Si–Si bonds induces LTT. Analogous results have been obtained for *a*-$Si_{1-x}N_x$:H (Ref. 9) and for porous Si (Ref. 13). The low-temperature exothermic transition is therefore a property of a large class of disordered materials, and its onset is attributable to the existence of nonequilibrium weak Si–Si bonds in the inhomogeneous film.

TABLE II. Hydrogen concentration N_H, microstructure parameter *R*, temperature T_{st} of the start of thermal effects, and total heat of reaction *Q* of the latter in *a*-Si:H deposited from H_2- and He-diluted SiH_4 (heating rate 10 °C/min.

Diluent gas	N_H, at.%	*R*	T_{st}, °C			*Q*, J/g		
			Type of effect					
			LTT	HTT		LTT	HTT	
				1	2		1	2
H_2	14.0	0.25	90	–	325	18.3	–	65.7
He	16.4	0.56	130	240	345	7.0	26.2	58.4
He	7.2	0.20	140	240	345	5.2	7.9	19.2
He	7.7	0.19	115	240	360	13.2	28.9	43.1

The high-temperature exothermic transition has been observed in amorphous Si and Ge alloys in the temperature range corresponding to hydrogen effusion, as confirmed by gas evolution experiments.[5,14] We have calculated the activation energy of this process in *a*-Si:H films deposited from hydrogen-diluted monosilane according to the equation[15]

$$\frac{d[\ln(r_h/T_{\max}^2)]}{d(1/T_{\max})}=-\frac{E}{R}, \tag{1}$$

where r_h is the heating rate, $T_{\max}$ is the temperature at which the effect is a maximum, *R* is the universal gas constant, and *E* is the activation energy. For our calculations we have separated out the region of the HTT of the DSC curves in Fig. 1 and subtracted the baselines. The activation energy is 1.68 eV, which is in line with the activation energy of diffusion-controlled hydrogen effusion (1.5 eV) from undoped *a*-Si:H (Ref. 14). Consequently, the temperature of the peak of the HTT and temperature of its onset characterize the hydrogen-bonding configurations in the film.[5,14]

Two exothermic peaks are discerned on the DSC curves for *a*-Si:H films deposited from He-diluted monosilane (Fig. 3): at 315 °C and at 420 °C, confirming the presence of different hydrogen microstructures in these films. Hydrogen effusion is an endothermic process,[16] but we have observed an exothermic process in our experiments. This contradiction is explained by the exothermic structural transformation of the silicon matrix in the same temperature interval after the liberation of hydrogen.[1,3] Consequently, the heat-flow process observed in *a*-Si:H is actually a superposition of exothermic and endothermic reactions accompanying the effusion of hydrogen from this material.

We now use the foregoing results, which demonstrate the relationship between microstructure and relaxation processes, to investigate the nature of the metastability in *a*-Si:H. The investigation is based on the following assumptions: a) the onset of the LTT is associated with the establishment of equilibrium between weak Si–Si bonds and dangling bonds; b) the LTT is observed in the same temperature interval as the Staebler–Wronski effect. The equilibrium between weak Si–Si bonds and dangling bonds in the presence of free charge carriers is analyzed in accordance with the mechanism[17]

$$e+h+(\mathrm{Si-Si})_{\mathrm{weak}}\Leftrightarrow 2D^0, \tag{2}$$

where *e* denotes an electron, *h* is a hole, $(Si–Si)_{weak}$ is a silicon weak bond, and D^0 is a neutral defect (silicon dangling bond).

This reaction is assumed to be responsible for the onset of the light-induced effect and the thermal effect in undoped *a*-Si:H, including the generation and annealing of defects. Making use of the fact that the reaction (2) is also the cause of structural relaxation, we construct a model of the LTT on the DSC curves to calculate the kinetic parameters of the given process.

According to existing models,[17,18] the annealing kinetics of metastable defects obeys a stretched exponential law:

$$[N_s(t)-N_s(\infty)]/[N_s(0)-N_s(\infty)]=\exp[-(t/\tau)^{\beta}],$$
$$T=\text{const}, \tag{3}$$

where $N_s(t)$, $N_s(0)$, and $N_s(\infty)$ are the densities of metastable defects at any time t, at the initial time, and in the equilibrium state, and τ is a characteristic time constant. The dispersion parameter $\beta=T/T_0$, where $T_0=600$ K (Ref. 17).

We assume that the total heat released in the LTT is governed by the heat of reaction Q_s of the process (2) and the variation of the density of metastable defects $\Delta N_{s0}(T)=[N_s(0)-N_s(\infty)]$ at $T=\text{const}$:

$$Q(T)\sim Q_s\Delta N_{s0}(T). \tag{4}$$

The elementary increment of the heat of reaction $dQ(T)$ for a change of temperature dT is determined by the heating rate $v=dT/dt$ and the differential $d\Delta N_{s0}(T)$, which is controlled by the metastable annealing kinetics; accordingly, it follows from (4) that

$$dQ(T)/dT\sim d\Delta N_{s0}(T)/dT. \tag{5}$$

Consequently, this approach enables us to describe the contribution of relaxation processes to the exothermic DSC heat-flow process, which can be used to model the LTT on the DSC curves. The quantity $d\Delta N_{s0}(T)$ can be estimated from the iteration

$$\langle d\Delta N_{s0}(T_1)\rangle=N_1-N_0$$

and

$$N_1-N_\infty=(N_0-N_\infty)\exp[-(dt/\tau_1)^{\beta_1}], \tag{6}$$

where N_0 is the initial density of metastable defects at the temperature T^*, N_1 is the density of metastable defects, τ_1 is the relaxation time at the temperature $T_1=T^*+dT$, and $\beta_1=T_1/T_0$. The equilibrium defect density N_∞ at a given temperature is determined from the law of effective masses in application to the reaction (2) [Eq. (5) in Ref. 17] and is expressed as follows in darkness (the prevailing condition of our DSC investigations):

$$N_\infty/(N_t-N_\infty)=4\ \exp(-F/kT), \tag{7}$$

where N_t is the density of weak Si–Si bonds prior to their conversion into defects, and $F=2(E_d-E_\tau)=0.8$ eV characterizes the energy difference between the defect (E_d) and weak-bond (E_τ) states.

The density of metastable defects N_i at temperature T_i is described by the equation

$$N_{i+1}-N_\infty=(N_i-N_\infty)\exp(-(dt/\tau_i)^{\beta_i}), \tag{8}$$

where $\tau_i=\tau_0\exp(E_\tau/kT_i)$, and $\beta_i=T_i/T_0$. To model the LTT, we use the time constant $\tau_0=10^{-10}$ s corresponding to the dispersive diffusion of hydrogen. It is evident that the activation energy E_τ governs the position of the heat-flow peak. The given model therefore exhibits the correlation between thermal effects and the relaxation kinetic parameters.

We have used the same approach to model the HTT, treating it as the result of structural relaxation after hydrogen effusion.[9] The total DSC spectrum is therefore conceived as the superposition of LTT and HTT contributions. Model curves of various films are shown in Fig. 1 together with experimental data. It should be noted that the HTT calculations give $E_\tau=0.7$ eV, which is far below the value calculated from the experimental results. This disparity implies that the HTT cannot be fully described by the given model, because the latter disregards hydrogen effusion *per se*.

The results of measurements of the Staebler–Wronski effect [the time dependences of the photoconductivity $\sigma_{\text{ph}}(t)$ and the dark conductivity $\sigma_d(t)$] for *a*-Si:H films deposited with various parameters has been least-squares fitted to a curve described by a stretched exponential law,[19] and from this fit we determine the parameters of the generation kinetics of metastable defects:

$$[\sigma(t)-\sigma(\infty)]/[\sigma(0)-\sigma(\infty)]=\exp[-(t/\tau)^{\beta}], \tag{9}$$

where $\sigma(t)$, $\sigma(0)$, and $\sigma(\infty)$ denote the conductivities at time t and in the initial and equilibrium states, respectively, τ is a characteristic time, and β is the dispersion parameter. The characteristic time τ is thermally activated:

$$\tau=\tau_0\exp(E_\tau/kT), \tag{10}$$

where E_τ is the activation energy of the characteristic defect-generation time. Taking into account the fact that the reaction (2) is the cause of the Staebler–Wronski effect (equilibrium shifts toward higher defect densities under the influence of light-induced excess free carriers), we calculate the annealing activation energy E_τ^{ann} according to Ref. 17 as $E_\tau^{\text{ann}}+F=F_g+E_\tau^{\text{gen}}$, where E_g is the width of the band gap, and E_τ^{gen} is the generation activation energy.

The activation energies of generation E_τ^{gen} and annealing E_τ^{ann} of metastable defects and the activation energy $\langle E_\tau^{\text{ann}}\rangle$ obtained from modeling the LTT on the DSC curves for *a*-Si:H films deposited with various parameters are summarized in Table III. Also shown in the table are the film growth rate r_g, the total hydrogen concentration N_{H}, the microstructure parameter R, and the photosensitivity $\sigma_{\text{ph}}/\sigma_d$ measured at the wavelength $\lambda=633$ nm ($T=300$ K). It follows from the table that all the samples have good photosensitivities, regardless of the degree of microstructural inhomogeneity (the parameter R). Moreover, the activation energies correlate with the parameter R and with the total hydrogen concentration N_{H} for each type of deposition process.

Figure 4 shows the dependence of the activation energy on the microstructure parameter R. It is clear that the values of E_τ^{ann} calculated from measurements of the Staebler-Wronski effect are close to the corresponding values of $\langle E_\tau^{\text{ann}}\rangle$ estimated from the DSC data. This result and the dependence of the variations of these parameters on R illustrate the general nature of the annealing of light-induced defects and the LTT. The reaction (2) can therefore be used to describe the generation of light-induced defects (the Staebler–Wronski effect) and the thermal effect corresponding to the relaxation process on the DSC curves. It is evident from Fig. 4 that the reaction kinetics (5) is controlled by the hydrogen microstructure. An increase in R leads to an increase in the activation energy as a result of the slowing of hydrogen diffusion.[19] The high stability of films deposited from He-diluted monosilane at $T_s=300$ °C in a 55-kHz discharge is

TABLE III. Hydrogen concentration N_H, microstructure parameter R, parameters of generation and annealing of metastable defects, and photosensitivity of *a*-Si:H films deposited with various parameters.

Preparation conditions	r_g, Å	N_H, at.%	R	E_τ^{gen}, eV (SWE)	E_τ^{ann}, eV (SWE)	$\langle E_\tau^{ann}\rangle$, eV (LTT)	σ_{ph}/σ_d, $T=300$ K
H_2-diluted	2.0	14.0	0.25	0.088	1.138	0.960	1×10^4
He-diluted	2.0	7.2	0.20	0.034	0.964	0.990	8×10^3
He-diluted	1.0	11.0	0.39	0.155	1.235	1.198	1×10^3
55 kHz	11.3	12.3	0.16	0.086	1.046	0.950	6×10^3
55 kHz	10.1	16.4	0.26	0.107	1.057	0.965	1×10^4
55 kHz	10.0	26.6	0.30	0.141	1.071	1.010	8×10^3

Note: SWE) Staebler–Wronski effect; LTT) low-temperature exothermic transition.

presumably associated with the formation of SiH_2 or clusters of the SiH type at internal grain boundaries of microscopic voids, voids, etc., which act as trapping centers for the dispersive diffusion of hydrogen. In this case an increase in the microstructure parameter R has the effect of slowing hydrogen diffusion and of increasing the activation energy of the characteristic time. It is also important to note that films deposited in a glow discharge at 55 kHz and at high growth rates have good optoelectronic properties and high photoconductivity.

CONCLUSIONS

We have shown that:

• differential scanning calorimetry (DSC) is an effective method for the display of structural inhomogeneity in disordered materials;

• the low-temperature exothermic transition is caused by the relaxation of weak Si–Si bonds;

• the high-temperature exothermic transition is caused by hydrogen effusion and subsequent microstructural relaxation.

This analysis can be used to characterize the hydrogen microstructure and degree of disorder of the silicon matrix.

We have proposed a method for calculating the parameters of the structural relaxation kinetics from DSC data.

A combined analysis of DSC and the Staebler–Wronski effect has disclosed that the generation of light-induced defects and the LTT on the DSC curves are of a common nature and are described by a reaction between silicon weak bonds and dangling bonds. The rate of this reaction in both directions is controlled by the hydrogen microstructure, and its magnitude diminishes as the microstructure parameter R increases.

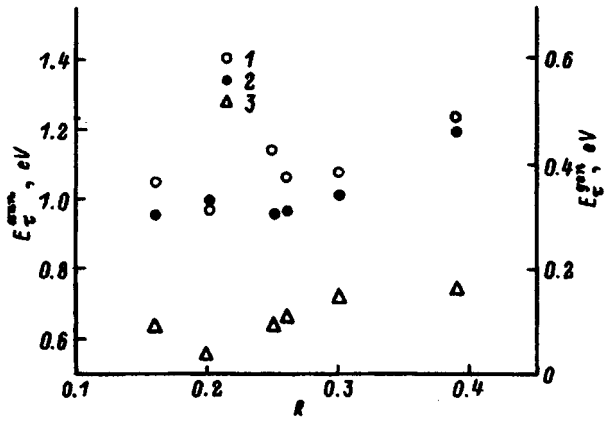

FIG. 4. Activation energies of the characteristic defect generation and annealing times versus microstructure parameter R for the investigated samples. 1) E_τ^{ann} 2) $\langle E_\tau^{ann}\rangle$ 3) E_τ^{gen}.

This work has received financial support from the International Association for the Promotion of Cooperation with Scientists from the Independent States of the Former Soviet Union (INTAS Project 94-4352) and also under the auspices of grants from the Ministry of General and Professional Education of the Russian Federation: Grant No. 670 in Electronics and Radio Engineering and Grant No. 85 GR-96 in Fundamental Problems of Electrical Engineering and Electric Power Engineering.

[1] S. R. Wronski, Solid State Technol. **31**, 113 (1988).
[2] J. B. Boyce, S. E. Ready, M. Stutzmann, and R. E. Norberg, J. Non-Cryst. Solids **114**, 211 (1989).
[3] S. M. Lee, S. J. Jones, Yu.-M. Li, W. A. Turner, and W. Paul, Philos. Mag. B **61**, 547 (1989).
[4] P. Roca i Cabarrocas, Z. Djebbour, J. P. Kleider, C. Longeaud, D. Mencaraglia, J. Sib, I. Bouizem, M. L. Theye, G. Sardin, and J. P. Stoquert, J. Phys. I **2**, 1979 (1992).
[5] W. Paul, S. J. Jones, and W. A. Turner, Philos. Mag. B **63**, 247 (1991).
[6] F. Demichelis, C. F. Pirri, E. Tresso, V. Rigato, and G. DellaMea, J. Non-Cryst. Solids **128**, 133 (1991).
[7] L. Battezzati, F. Demichelis, C. F. Pirri, and E. Tresso, Physica B **176**, 73 (1992).
[8] N. Sridhar, D. D. L. Chung, W. A. Anderson, and J. Coleman, in *Amorphous Silicon Technology-1995*, edited by M. Hack; E. A. Schiff *et al.*, Mater. Res. Soc. Symp. Proc. **377**, 319 (1995).
[9] A. A. Aivazov, B. G. Budaguan, and A. Yu. Sazonov, Physica B **193**, 195 (1994).
[10] M. Cardona, Phys. Status Solidi B **118**, 463 (1983).
[11] A. Canillas, J. Campmany, J. L. Andujar, and E. Bertran, Thin Solid Films **228**, 109 (1993).
[12] J. C. Knights, K. A. Lujan, M. P. Rosenblum, R. A. Street, D. K. Biegelsen, and J. A. Reimer, Appl. Phys. Lett. **38**, 331 (1981).
[13] B. G. Budaguan, A. A. Aivazov, and A. Yu. Sazonov, in *Amorphous Silicon Technology-1996*, edited by M. Hack *et al.*, Mater. Res. Soc. Symp. Proc. **420**, 635 (1996).
[14] W. Beyer and H. Wagner, J. Appl. Phys. **53**, 8745 (1982).
[15] H. E. Kissinger, Anal. Chem. **32**, 1702 (1957).
[16] S. J. Jones, S. M. Lee, W. A. Turner, and W. Paul, Mater. Res. Soc. Symp. Proc. **149**, 45 (1989).
[17] G. Schumm, Appl. Phys. Lett. **66**, 2706 (1995).
[18] B. G. Budaguan, O. N. Stanovov, and M. N. Meytin, J. Non-Cryst. Solids **163**, 297 (1993).
[19] J. Kakalios and W. B. Jackson, in *Amorphous Silicon and Related Materials*, edited by H. Fritszsche (World Scientific, New Jersey, 1988), p. 207.

Translated by James S. Wood

Light-induced processes in *a*-Si:H films at elevated temperatures

I. A. Kurova, É. V. Larina, N. N. Ormont, and D. V. Senashenko

Physics Department, M. V. Lomonosov Moscow State University, 119899 Moscow, Russia
(Submitted October 14, 1996; accepted for publication April 1, 1997)
Fiz. Tekh. Poluprovodn. **31**, 1455–1459 (December 1997)

At temperatures $T>120$ °C the kinetics of the dark conductivity (σ_d) of undoped and boron-doped *a*-Si:H films during and after the cessation of illumination is observed to be nonmonotonic, with fast and slow processes of variation of σ_d of opposite sign. A fast or slow σ_d relaxation process described by a stretched exponential function can be isolated by varying the duration and intensity of illumination or the film temperature. The nonmonotonic relaxation of σ_d is described by a sum of two stretched exponentials, whose parameters τ and β depend on the film characteristics and on the temperature, exposure time, and intensity of illumination. The nature of the nonmonotonic relaxation is discussed. © *1997 American Institute of Physics.* [S1063-7826(97)02411-3]

The formation and relaxation of light-induced metastable (LIM) states in *a*-Si:H have been investigated in many papers.[1–3] The investigations have been carried out primarily in the vicinity of room or liquid-nitrogen temperatures, where the dark conductivity (σ_d) and the photoconductivity (σ_{ph}) have been observed to decrease monotonically in undoped and doped *n*-type films after the cessation of illumination. It has been established that these variations are attributable to the formation of neutral, metastable dangling bonds.[1] An increase in σ_d has been observed[4,5] in boron-doped, *p*-type films, but it vanished when the temperature was raised to 80 °C. It has been shown that this phenomenon is mainly due to optical charge transfer from local states in the oxide layer or at its boundary with the film and also, as a result of this process, the formation of a subsurface accumulation layer of elevated *p*-type conductivity in the film. Nonmonotonic relaxation of σ_d has been observed in later studies[6,7] in boron- and phosphorous-doped films after illumination at elevated temperatures; σ_d increased rapidly to values above the equilibrium level σ_{d0} and then gradually decreased to the equilibrium value. It has been established that the relaxation processes are bulk processes.[7] The authors of the papers assumed that the rapid rise of σ_d is caused by the annealing of light-induced dangling bonds, and the slow decline of σ_d is caused by the deactivation of light-induced, electrically active impurities. However, detailed studies of the laws and nature of the nonmonotonic relaxation of σ_d were not carried out in the cited work.

Here we report an investigation of undoped and boron-doped *a*-Si:H films. All the films were grown at the State Scientific-Research and Design Institute of the Rare Metal Industry (GIREDMET, Moscow) by deposition in an rf discharge plasma, and doping was implemented from the gaseous phase. The characteristics of the investigated films are given in Table I. The boron concentration in the investigated films was determined by secondary ion spectroscopy.

The kinetic behavior of σ_d during and after the cessation of illumination of the films at elevated temperatures $T>120$ °C was investigated. The light source was a halogen lamp, and the intensity of illumination of the films was varied by means of neutral filters. At the start of each test the films were annealed for one hour at $T_a=190$ °C and were then slowly cooled down to the temperature at which their illumination and the measurements were to be performed.

Figure 1 shows the kinetics of the normalized dark conductivity $\sigma_d(t)/\sigma_{d0}$ for film No. 4 during and after illumination at various intensities and at various temperatures. We see that the time variation of σ_d during exposure is nonmonotonic (curves *1*); σ_d decreases at first and then increases. The postillumination σ_d relaxation curves depend on the illumination time t_{ill}. If t_{ill} is short, i.e., corresponds to the descending part of the $\sigma_d(t_{ill})$ curve *1*, the relaxation of $\sigma_d(t)$ is monotonic (curve *2*), and the logarithm of the ratio $\sigma_d(t)/\sigma_{d0}$ is described by the stretched exponential function

$$\log[\sigma_d(t)/\sigma_{d0}]=A\ \exp[-(t/\tau)^{\beta}]. \tag{1}$$

If the illumination time is increased to values corresponding to the ascending part of the $\sigma_d(t_{ill})$ curve, the postillumination relaxation of σ_d is nonmonotonic (curve *3*). It encompasses two processes: the rapid rise of σ_d to values above σ_{d0}, and the slow decay of σ_d to the equilibrium value. It is also evident from Fig. 1 (curve *4*) that a slow σ_d relaxation process can be isolated by raising the temperature during illumination of the film. The abatement of the first process can be attributed to a decrease in the density of LIM states responsible for the first process, owing to an increase in their annealing rate when the temperature is increased.

The investigations show that a slow σ_d relaxation process can also be isolated by decreasing the intensity of illumination of the film without changing its temperature, i.e., by decreasing the rate of formation of LIM states responsible for the first process. Figure 2 shows typical plots of the σ_d relaxation kinetics for film No. 3 after its illumination with various intensities at a single temperature (curves *1* and *3*) and after illumination with a low intensity at different temperatures (curves *2–4*). It is evident from Fig. 2 that at $t=400$ K after illumination of the film by high-intensity light ($W=90$ mW/cm^2, $t_{ill}=10$ s) the relaxation of σ_d is nonmonotonic (curve *1*), and after low-intensity illumination ($W=4$ mW/cm^2, $t_{ill}=300$ s) the relaxation of σ_d is monotonic and corresponds to the gradual decrease of σ_d to the equilibrium value. This monotonic, slow relaxation of σ_d is

TABLE I.

No.	d, μm	T_s, °C	N_B, cm^{-3}	E_d, eV	σ_d, $\Omega^{-1}\cdot$cm^{-1} ($T=290$ K)	E_1, eV	ν_1, s^{-1}	E_2, eV	ν_2, s^{-1}
1	1	250	–	0.74	8×10^{-10}	1.00	4×10^{9}	1.05	5×10^{8}
2	1	290	1×10^{17}	0.83	2×10^{-10}	1.05	1×10^{11}	1.1	5×10^{9}
3	4	290	2×10^{17}	0.85	1.2×10^{-11}	1.13	2×10^{13}	1.27	1.3×10^{13}
4	1	300	2×10^{18}	0.66	2×10^{-9}	0.86	1×10^{9}	0.88	1×10^{8}

Note: Here d is the film thickness, T_s is the substrate temperature during film growth, N_B is the total Bohr concentration, E_d is the dark conductivity activation energy, σ_d is the dark conductivity at $T=290$ K, $E_{1,2}$ is the activation energy of $\tau_{1,2}$, and $\nu_{1,2}$ is the preexponential factor for $\tau_{1,2}$.

also described by a stretched exponential function, whose parameters τ and β depend on the temperature and the illumination time for each film.

Figure 3 shows the σ_d relaxation kinetics of the undoped film No. 1 after illumination at various temperatures by light of intensity $W=90$ mW/cm^2 for a duration $t_{ill}=15$ s. Clearly, two σ_d relaxation processes are observed in the undoped film after illumination at elevated temperatures, the rates of both processes increasing with the temperature. The behavior of $\log[\sigma_d(t)/\sigma_{d0}]$ is described by the sum of two stretched exponentials, whose parameters depend on the temperature, duration, and intensity of illumination. These parameters were determined as follows. The fast relaxation process was assumed to terminate at a time $t\gtrsim t_{max}$, where t_{max} is the time at which the maximum value of $\log(\sigma_d/\sigma_{d0})$ is observed. Initially, therefore, the parameters of the slow process were determined from the behavior of $\log[\sigma_d(t)/\sigma_{d0}]$ at $t>t_{max}$. The parameters of the fast process were determined from the sum of the two stretched exponentials describing the nonmonotonic relaxation of σ_d over the entire time interval of the measurements, taking into account the resulting parameters of the slow process.

The logarithm of the ratio $\sigma_d(t)/\sigma_{d0}$ determines the time variation of the position of the Fermi level (ΔE_F) in the band gap relative to the equilibrium value: $\log(\sigma_d/\sigma_{d0})=\Delta E_F/kT$. Assuming that the density of states is constant in the vicinity of the Fermi level during illumination, we can assume that $\Delta E_F(t)\sim N(t)$, where N is the density of LIM states above or below the Fermi level; the kinetic behavior of the density of LIM states $N(t)$ is thus described by stretched exponentials under the stated assumptions.

Temperature curves of the parameters of the stretched exponential functions τ_1,τ_2 and β_1,β_2 for the investigated films are shown in Fig. 4 and the insets to Figs. 2 and 3 (the indices 1 and 2 refer to the fast initial process and the slow terminal process, respectively). Note that values of τ_2 and β_2 determined from the monotonic relaxation of σ_d at a low illumination intensity ($W=4$ mW/cm^2) and from the nonmonotonic relaxation at a high intensity ($W=90$ mW/cm^2) have been used to plot the $\tau_2(T)$ and $\beta_2(T)$ curves in the inset to Fig. 2. It is evident that τ_1 and $d\tau_2$ depend exponentially on the temperature for all the films:

$$\tau_{1,2}=\nu_{1,2}^{-1}\exp(E_{1,2}/kT). \tag{2}$$

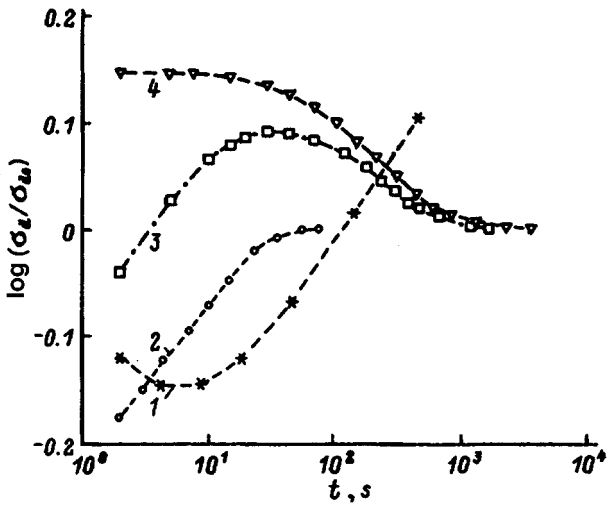

FIG. 1. Kinetic behavior of the normalized dark conductivity of film No. 4 at $T=415$ K. *1*) During illumination with $W=90$ mW/cm^2; *2–4*) after the cessation of illumination: *2*) $t_{ill}=3$ s, $T=415$ K; *3*) $t_{ill}=60$ s, $T=415$ K; *4*) $t_{ill}=60$ s, $T=430$ K.

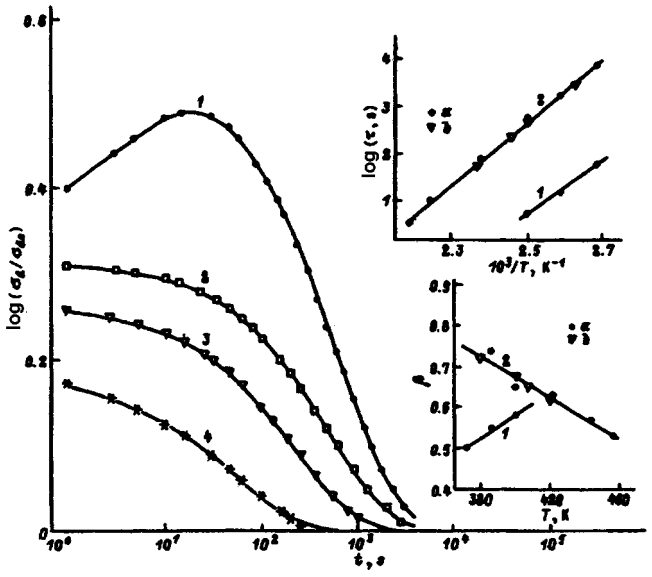

FIG. 2. Kinetic behavior of the normalized dark conductivity of film No. 3 after the cessation of illumination. *1*) $t_{ill}=5$ s, $W=90$ mW/cm^2, $T=400$ K; *2–4*) $t_{ill}=300$ s, $W=4$ mW/cm^2, $T=400$ K, 407 K, 420 K, respectively. Insets: temperature dependences of the parameters τ (upper inset) and β (lower inset): *1*) fast relaxation; *2*) slow relaxation; a) result of processing the nonmonotonic relaxation curves; b) result of processing the monotonic relaxation curves.

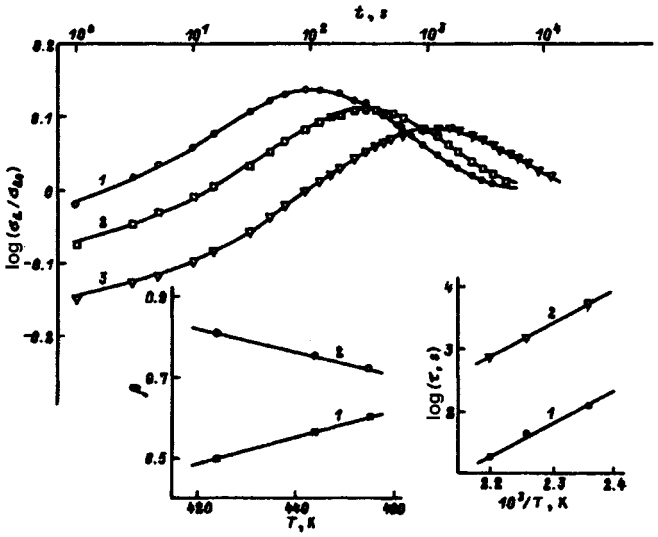

FIG. 3. Kinetic behavior of the normalized dark conductivity after the cessation of illumination for film No. 1 at various temperatures, $t_{ill}=15$ s, $W=90$ mW/cm^2: *1*) $T=423$ K; *2*) 443 K; *3*) 455 K. Insets: temperature dependences of the parameters β (left) and τ (right) of the stretched exponential functions describing the nonmonotonic relaxation curves: *1*) fast relaxation; *2*) slow relaxation.

The activation energies E_1 and E_2 of $\tau_{1,2}$ and the preexponential factors ν_1 and ν_2 are given in Table I. Clearly, they differ for different films, and in all the films $E_1<E_2$ and $\nu_1>\nu_2$, i.e., they violate the Meyer–Neldel rule. This fact suggests that the two processes differ in nature. The main difference between the fast and slow processes shows up in the temperature dependence of β. We observe that β_1 increases, while β_2 decreases with increasing temperature in all the investigated films in both the monotonic and the nonmonotonic σ_d relaxation regimes (see Fig. 2), i.e., irrespective of whether or not the fast process is present.

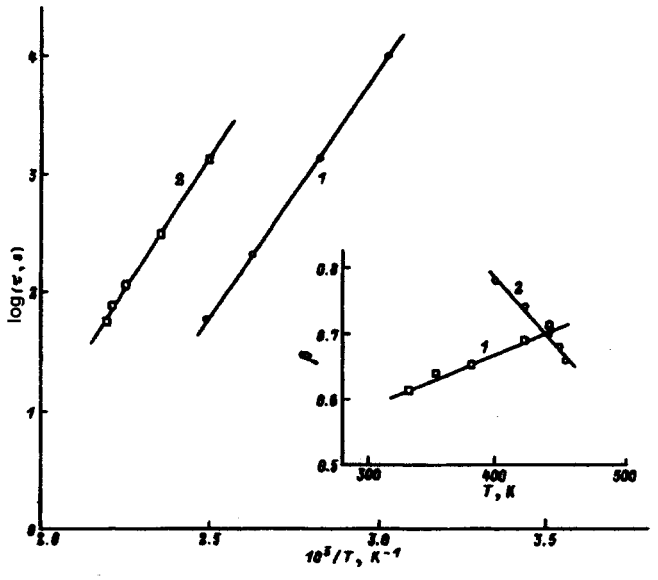

FIG. 4. Temperature dependences of the parameters τ and β (inset) for film No. 4 after illumination at the intensity $W=90$ mW/cm^2 and different exposure times. *1*) 5 s, fast relaxation; *2*) 60 s, slow relaxation.

An increase of β with increasing temperature has been observed in several studies during the annealing of LIM states identified as neutral dangling bonds,[8] whose annealing causes σ_d to increase in relaxation. A decrease of β with increasing temperature has been observed[9] in the relaxation of thermally induced metastable bonds in undoped films that had been grown at low temperatures $T_s\approx 100$ °C and had many voids as a result. The authors attributed this dependence of $\beta(T)$ to the relaxation of metastable dangling bonds on the surfaces of the voids, whose dimensions decrease as the temperature increases. In our investigated films grown at high temperatures ($T_s>250$ °C) the presence of a high concentration of voids is not very probable and, hence, the probability is low that the slow relaxation of σ_d is associated with the annealing of metastable dangling bonds on the void surfaces. On the other hand, the presence of the slow process with a characteristic dependence $\beta(T)$ in all the investigated films with both *n*-type and *p*-type conductivity leaves us no choice but to postulate a single mechanism for this process.

Previously[6,7] the slow σ_d relaxation process has been explained by the deactivation of light-induced, electrically active impurities after the cessation of illumination. In accordance with this hypothesis, the slow relaxation of the conductivity in our investigated *p*-type film (No. 4) is attributable to the deactivation of light-induced, metastable, electrically active boron atoms. For the *n*-type films (Nos. 1–3) not specially doped with a donor impurity, the presence of uncontrolled impurities must be assumed. Such impurities can be carbon, nitrogen, and oxygen, the introduction of which shifts the Fermi level toward the conduction band.[10] Consequently, the slow processes of variation of σ_d in films 1–3 during and after the cessation of illumination can be identified with processes of activation and deactivation of these impurities, and the observation of the nonmonotonic variation of σ_d in undoped films provides the potential basis of a method for determining the presence of uncontrolled impurities in them.

At the same time, other mechanisms are possible for the generation of LIM states during illumination in undoped and doped *a*-Si:H films. In particular, Crandall[11] has proposed the transfer of positively and negatively charged silicon dangling bonds formed during the growth of both doped and undoped *a*-Si:H films[12] as the mechanism underlying the generation of metastable dangling bonds during injection and illumination of the films. This mechanism has been invoked in an interpretation of the relaxation processes of metastable dangling bonds formed during carrier injection in *p*-type and *n*-type films.[13] Finally, the fast and slow variations of σ_d during and after the cessation of illumination can be identified with various regions of the film having different properties resulting from the nonuniform distribution of hydrogen and impurities, the types of bonds that they form with silicon, etc. It follows, therefore, that further investigations are needed to resolve the question of the nature of the slow variation of σ_d in *a*-Si:H films during and after the cessation of illumination.

The authors are grateful to I. P. Zvyagin and A. G. Kazanskiĭ for helpful discussions.

This work has received financial support from the State

Committee on Higher Education of the Russian Federation (Goskomvuz RF Grant 95-0-71-153 in Fundamental Natural Science) and the Scientific-Technical Program ''Universities of Russia.''

[1] M. Stutzmann, N. B. Jackson, and C. C. Tsai, Phys. Rev. B **32**, 23 (1985).
[2] E. Eser, J. Appl. Phys. **59**, 3508 (1986).
[3] P. Stradins and H. Fritzsche, Philos. Mag. B **69**, 121 (1994).
[4] B. Aker and H. Fritzsche, J. Appl. Phys. **54**, 6628 (1983).
[5] I. A. Kurova and D. A. Mochalova, Fiz. Tekh. Poluprovodn. **23**, 573 (1989) [Sov. Phys. Semicond. **23**, 359 (1989)].
[6] X. M. Dong and H. Fritzsche, Phys. Rev. B **36**, 9378 (1987).
[7] J. Jang, S. C. Park, S. C. Kim, and C. Lee, Appl. Phys. Lett. **51**, 1804 (1987).
[8] R. A. Street, Sol. Cells **24**, 211 (1988).
[9] K. Takeda, H. Hikita, Y. Kimura, H. Yokomichu, and K. Morigaki, J. Non-Cryst. Solids **198–300**, 486 (1996).
[10] P. E. Vanier, A. E. Delahoy, and R. W. Griffith, J. Appl. Phys. **52**, 5235 (1981).
[11] R. S. Crandall, Phys. Rev. B **43**, 4057 (1991).
[12] H. M. Branz and M. Silver, J. Non-Cryst. Solids **114**, 639 (1989).
[13] M. W. Carlen, Y. Xu, and R. S. Crandall, Phys. Rev. B **51**, 2173 (1995).

Translated by James S. Wood

Manifestation of percolation conductivity of short-channel field-effect transistors in the spectrum of shallow interface states

B. A. Aronzon, D. A. Bakaushin, A. S. Vedeneev, V. V. Ryl'kov, and V. E. Sizov

Kurchatov Institute (Russian Scientific Center), 123192 Moscow, Russia
(Submitted March 6, 1997; accepted for publication March 19, 1997)
Fiz. Tekh. Poluprovodn. **31**, 1460–1467 (December 1997)

The effective density of shallow interface states N_{ss} is investigated in the temperature range $T=77-300$ K using the field-effect method in short-channel (0.5–5 μm) Si-MNOS and GaAs-based FET's with high (greater than 10^{12} cm^{-2}) concentrations of built-in charge in the sub-gate insulator. A peculiarity of the density of electronic states N_{ss} was found having the form of a peak, which manifests itself more distinctly at lower temperatures, higher concentrations of built-in charge, and shorter gates. The peak was observed at the same values of the channel conductance $G\sim q^2/h$, regardless of variations in the above-enumerated parameters, the thickness of the sub-gate insulator, and the channel-length-to-width ratio. This means that the energy depth of the peak ($\sim$40–120 meV) varies in proportion to T, which contradicts the current understanding of the interface states caused by both the fluctuation potential (FP) and surface defects or traps. The results are interpreted within the framework of percolation theory applied to the conductivity of strongly disordered systems. The N_{ss} peculiarity is associated with a transition from the conductivity of a two-dimensional effective solid, which occurs when the fluctuation potential is strongly screened by surface electrons, to conductivity via a quasi-one-dimensional potential trough organized by local regions with reduced surface potential under conditions of a strong fluctuation potential. [S1063-7826(97)01212-X]

1. INTRODUCTION

The electronic properties of disordered systems, in particular, quasi-two-dimensional systems realized at semiconductor–semiconductor and semiconductor–insulator interfaces, continues to generate sustained scientific and technological interest. According to the present thinking on scaled miniaturization, decreasing the dimensions of the basic elements of integrated and microwave electronics, which reveal a need for transistors with submicron gate length, requires a radical increase in the dopant-impurity concentration in the active regions of the semiconductor layers up to $10^{18}-10^{19}$ cm^{-3}, e.g., in GaAs–AlGaAs-based transistors (of HEMT type) and structures with δ-doped layers.[1,2] In turn, increasing the doping level leads to an amplification of electrical inhomogeneity as a result of growth of the fluctuation potential (FP) induced by the randomly distributed ionized impurities.[3]

According to Refs. 4–7, it appears that the most striking manifestation of the surface fluctuation potential in MIS-type systems is electron (hole) localization in the vicinity of minima (maxima) of the random potential well and, as a consequence, the appearance near the edges of the semiconductor band gap of the so-called tails of the density of localized interface states with characteristic U-shaped energy spectrum. Spectra of such type, obtained by using the method of capacitance–voltage characteristics in MIS systems with high surface concentration of charged centers and generally uncontrollable, built-in charges in the insulator, have been described in detail (see, e.g., Refs. 8–10). In quasi-two-dimensional systems of semiconductor layers with enhanced impurity concentration these phenomena also take place,[11,12] with the difference that the nature of the fluctuation potential in this case is known and the main parameters of its sources (concentration and the average distribution relative to the inversion channel) are controlled during the fabrication process. In other words, systems of such type can be considered as controlled–disordered, allowing a description of their electronic characteristics within the scope of the familiar fluctuation potential theory.[5–7]

Turning now to the discussion of our study, we note that methods of capacitance–voltage spectroscopy have a very narrow region of applicability, limited to room temperature measurements and structures with relatively large area of the field electrode, exceeding the area of the gate of field-effect transistors by several orders of magnitude. At the same time, allowing for the particular features of the microelectronic devices associated with their small dimensions, in particular, the fundamental possibility of manifesting mesoscopic effects,[13,14] it may be expected that the electronic characteristics of short-channel transistors and large-area test structures can differ substantially. In this regard, the development of experimental methods for determining the spectra of shallow interface states formed by the fluctuation potential appears promising.[15] (A particular example of such approaches is the field-effect method, which is based on measurements of the dependence of the conductance of the surface channel of the transistors on the gate potential.) As the results of our

recent spectroscopic studies of GaAs–AlGaAs–HEMT's with a long gate $\sim 0.5\,\mu$m in the temperature interval $T=77-300$ K have shown,[12] the effective density of states exhibits a peak-like feature whose energy depth varies with temperature. This does not fit within the framework of classical theory of the interface states of ''fluctuational'' origin.[5] In the present paper we show that this feature is of a general character for short-channel transistor structures with high concentration of charged centers and is a consequence of the manifestation, under conditions of a strong fluctuation potential, of the percolation regime of conductivity in the early stages of formation of the surface electron channel.

2. EXPERIMENTAL TECHNIQUE

The formalism of the experimental approach to the analysis of the spectrum of interface electron states consists in the following. For a small longitudinal voltage $V_d \approx kT/q$ the conductance of the inversion channel of a field-effect transistor $G=I_d/V_d$ is measured as a function of the gate potential V_g (I_d is the current strength in the source–sink circuit, k is the Boltzmann constant, and q is the elementary charge). The gate potential is related to the surface charge concentration in the semiconductor by the equation[8,9]

$$C_0(V_g-\varphi_s)=q(n_s+n_d), \tag{1}$$

where C_0 is the sub-gate specific capacitance, φ_s is the surface potential of the semiconductor, $n_d \propto (\varphi_s N_0)^{1/2}$ is the charge density in the depleted layer of the semiconductor formed by the dopant impurity with concentration N_0, and n_s is the charge-carrier concentration in the surface channel. The effective density of electron states, including free and localized charge carriers, is given by $N_{ss}=dn_s/d(q\varphi_s)$ (Ref. 5). Differentiating Eq. (1) with respect to φ_s, we find

$$N_{ss}=(C_0/q^2)(dV_g/d\varphi_s-1)-dn_d/d(q\varphi_s), \tag{2}$$

where the term $dn_d/d(q\varphi_s)\propto(N_0/\varphi_s)^{1/2}\approx$ const is a known function. In the cases under consideration, of a strong fluctuation potential and low substrate doping level, this term makes an insignificant contribution to N_{ss} (Ref. 5); we therefore drop it and define the effective density of states by

$$N_{ss}=(C_0/q^2)(dV_g/d\varphi_s-1). \tag{2a}$$

Under conditions of a strong fluctuation potential ($\Delta \gg kT$, Δ is the energy scale of the fluctuations)[5–7] statistical fluctuations of the built-in charge density induce a random potential well in the skin layer of the semiconductor. Local (bound) states are formed in the region of the minima of this random potential well. The electrons filling these states are lower in energy than the percolation level determined by the average surface potential φ_s; therefore, they do not contribute to the conductance of the surface channel, and only those electrons remain free whose energy lies above the percolation level. In the absence of degeneracy (as long as the Fermi level does not intersect the average position of the bottom of the conduction band) the electrons in the channel are predominantly localized and only an insignificant fraction of them (with concentration $n_c \ll n_s$) determines the magnitude of $G \propto n_c$. In other words, under conditions of a strong fluctuation potential in the absence of degeneracy, N_{ss} is determined mainly by the localized electrons. Under these conditions the free-electron concentration in the channel varies according to the law $n_c \propto \exp(q\varphi_s/kT)$ (Refs. 5 and 6), which allows us to eliminate the unknown parameter from expression (2) and rewrite it in terms of measurable quantities: $G \propto n_c$ (to within the concentration dependence of the electron mobility) and V_g

$$N_{ss}\simeq(C_0/q^2)[(q/kT)dV_g/d(\ln G)-1]. \tag{3}$$

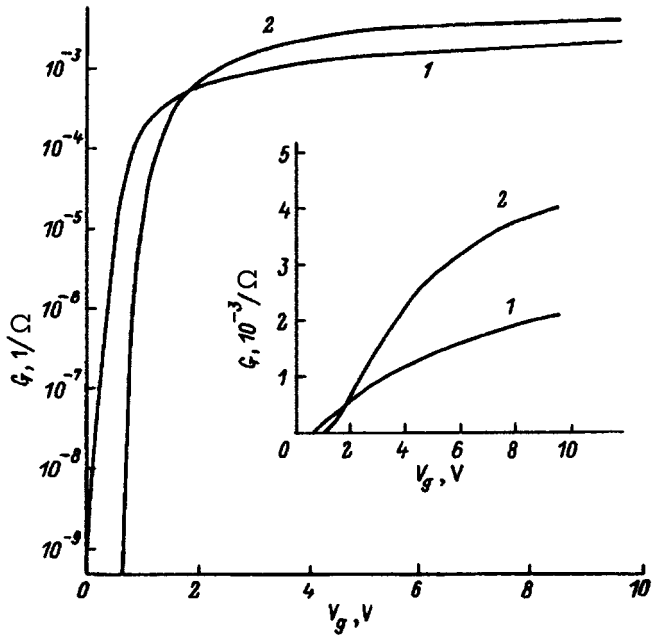

FIG. 1. Dependence of the conductance of the inversion n-channel G on the gate potential for a Si–MOS field-effect transistor, plotted both semilogarithmically and on a linear plot (inset). $T=300$ K (*1*) and 77 K (*2*).

The experimental setup realizing the given approach is described in Ref. 16. Results of validation of the method on a commercially fabricated transistor test structure with an n-type inversion channel (thickness of the sub-gate oxide 500 Å, gate length 5 μm, width 50 μm, substrate weakly doped p-Si of type KDB-12 with orientation (100)), are shown in Fig. 1. The field-effect curves (Fig. 1) demonstrate the classical mechanism of formation of the inversion channel:[8,9] for small V_g the conductance G varies as a function of V_g according to an exponential law, typical of the weak-inversion region (1); at higher values of V_g the dependence $G(V_g)$ becomes linear, which indicates a transition to strong inversion ($dn_c/dV_g=C_0/q$). The functional dependence $N_{ss}(G)$ (Fig. 2) at 300 K illustrates the contribution of the free electrons and impurities from the space-charge region of the semiconductor to the effective density of states (3), and at 77 K it also illustrates the appearance of the tail of the density of shallow localized states due to fluctuation-potential effects which grow as the temperature is lowered.

3. OBJECTS OF STUDY AND RESULTS

As our objects of study we chose structures of three types: Si-MNOS transistor structures, fabricated by integrated circuit technology (PPZU SBIS), selectively doped

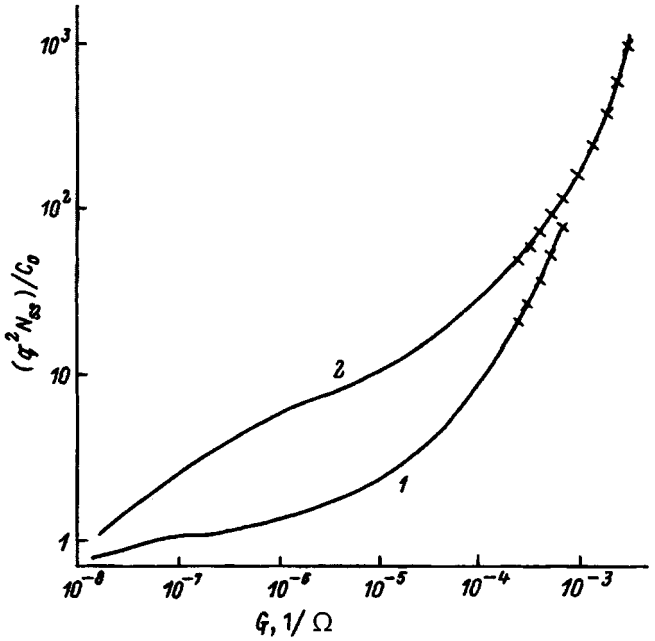

FIG. 2. Effective density of interface states as a function of G according to the data in Fig. 1. $T=300$ K (*1*) and 77 K (*2*).

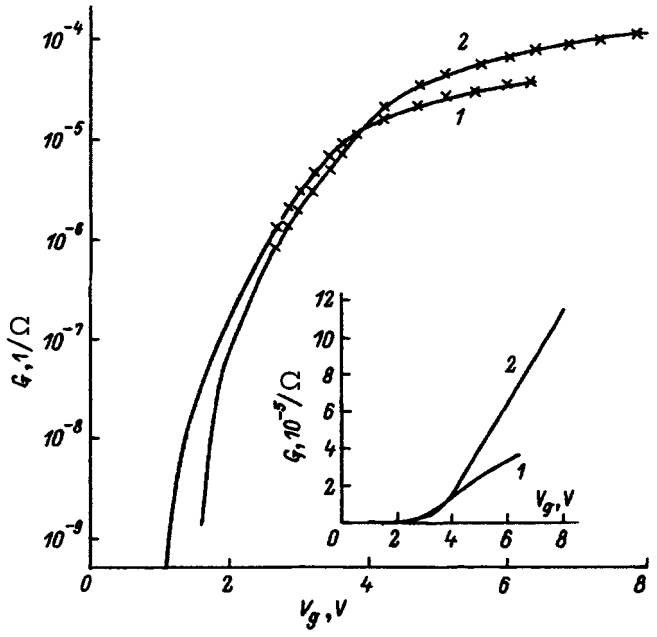

FIG. 3. Dependence on V_g of the conductance of the n-type inversion channel of a ''long'' ($150\times 20\ \mu m^2$) Si-MNOS transistor, plotted both semilogarithmically and on a linear plot (inset). $T=300$ K (*1*) and 77 K (*2*).

GaAs–AlGaAs-HEMT's, and GaAs-based Schottky-barrier-gate field-effect transistors (Schottky-gate FET's). A general feature of these systems is their high concentration of built-in charge—electrons captured by traps on the SiO_2–Si_3N_4 interface, and also ionized impurities in the AlGaAs-HEMT donor layer and in the barrier layer of the Schottky-gate FET. An advantage of Si-MNOS structures as model objects is that controllable electron injection can be used in them to modify the built-in charge concentration within wide limits. For all these systems the dependence $G(V_g)$ was measured in the temperature interval 77–300 K and the density of interface states (3) was determined as a function of G.

MNOS-systems (sub-gate insulator—layers of Si_3N_4 and SiO_2 of thickness 350 and 30 Å, respectively) with n-type inversion channel were built in the form of ''short'' (gate length 5 μm and width 50 μm) and ''long'' (length 150 μm and width 20 μm) transistors on the same substrates as the Si-MOS transistors (Figs. 1 and 2). Figures 3–6 plot the field dependences of the channel conductance, measured for a fixed charge state of the SiO_2–Si_3N_4 interface, and also the corresponding density of states for the long (Figs. 3 and 4) and short (Figs. 5 and 6) transistors.

Let us turn our attention first to the long transistor. Its field-effect curves (Fig. 3) are qualitatively similar to field-effect curves considered earlier for Si-MOS transistors (Fig. 2): in the weak-inversion region they have a segment of exponential growth of G, transitioning to a linear dependence in the strong-inversion region. At the same time, it can be seen by comparing the data in Figs. 1–4 that the charge built into the sub-gate insulator of the MNOS structure leads to a noticeable ''flattening out'' of the dependence $G(V_g)$ as a result of substantial localization of the electrons in the strong fluctuation potential of the Si–SiO_2 surface. Indeed, according to Refs. 4–7, the energy scale of the fluctuation potential is

$$\Delta=(q^2/\chi)(\pi n_t)^{1/2}, \tag{4}$$

where χ is the average dielectric constant of the semiconductor and sub-gate insulator, and n_t is the surface concentration of the built-in charge. For the experimental data (Fig. 3) the density of charge trapped at the SiO_2–Si_3N_4 interface, found

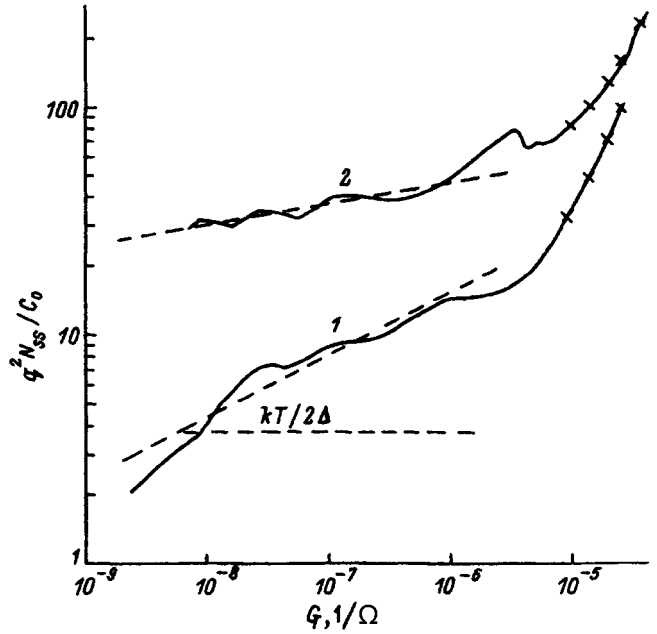

FIG. 4. Effective density of interface states N_{ss} as a function of G according to the data of Fig. 3. $T=300$ K (*1*) and 77 K (*2*).

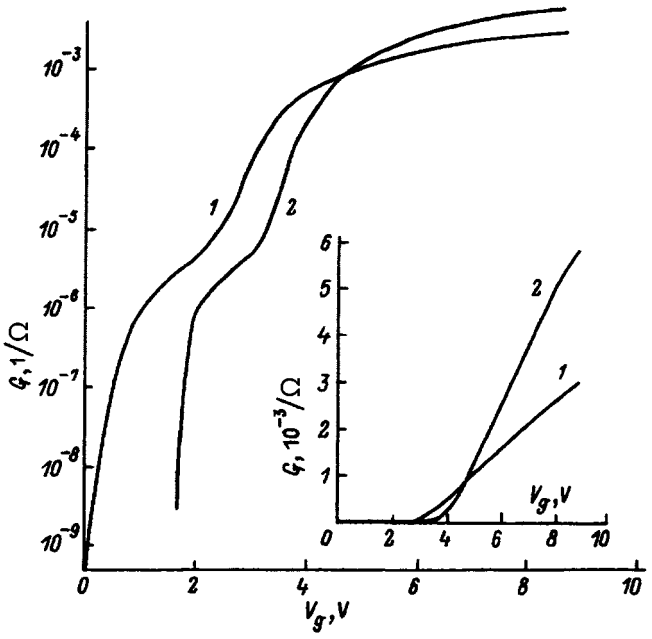

FIG. 5. Dependence on V_g of the conductance of the n-type inversion channel of a ''short'' ($5\times 50\ \mu m^2$) Si-MNOS transistor, plotted both semilogarithmically and on a linear plot (inset). $T=300$ K (*1*) and 77 K (*2*).

from the threshold bias voltage, is roughly $5\times 10^{12}\ cm^{-2}$, which corresponds to $\Delta\approx 40$ meV, a value which exceeds kT even at room temperature.

The character of the behavior of $N_{ss}(G)$ under conditions of a strong fluctuation potential ($\Delta \gg kT$) was considered in Refs. 5 and 6, where, in particular, it was shown that in cases of practical interest ($n_s \geqslant n_t^{1/2} d$, where d is the thickness of the sub-gate insulator), the regime of nonlinear electron screening is realized. In this regime we have

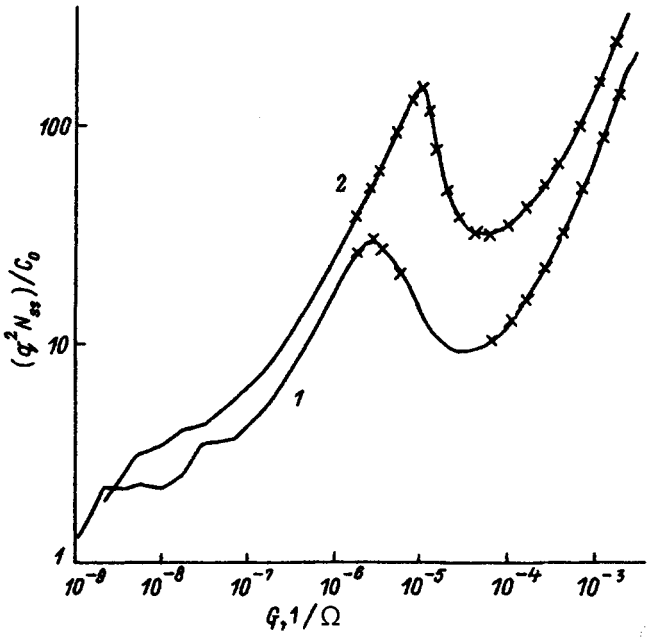

FIG. 6. Effective density of interface states N_{ss} as a function of G according to the data of Fig. 5. $T=300$ K (*1*) and 77 K (*2*).

$$n_s \propto \exp(q\varphi_s/2\Delta) \propto n_c^{kT/2\Delta}. \tag{5}$$

Noting that $N_{ss}=dn_s/d(q\varphi_s)$ and invoking relation (5), we have

$$N_{ss}=n_s/2\Delta \propto n_c^{kT/2\Delta} \propto G^{kT/2\Delta}. \tag{6}$$

Increasing the electron concentration increases the screening of the fluctuation potential; as a result, for $n_s \approx n_t$ it disappears. Under these conditions, the electrons in the channel are predominantly free ($n_c \approx n_s$) and, taking Boltzmann statistics into account, we have

$$N_{ss} \approx n_c/kT \propto G. \tag{7}$$

This segment, in particular, is distinctly noticeable in the graph of $N_{ss}(G)$ in Fig. 2. We may also note that expression (7) is a particular case of expression (3) for the strong-inversion region in which $dn_c/dV_g \approx C_0/q$.

Thus, according to existing ideas, N_{ss} varies with G according to a power law with an exponent $\alpha=kT/2\Delta \ll 1$ in the weakly opened channel region (the regime of nonlinear screening of the fluctuation potential) and $\alpha\approx 1$ in the regime in which the fluctuation potential is strongly screened.

The density of states in the considered Si-MNOS structure (Fig. 4) exceeds the value of N_{ss} in the case of the Si-MOS transistor (Fig. 2) by an order of magnitude and varies with G according to the expounded theory of the fluctuation potential: the exponent in the weak-inversion region is proportional to T and gives $\Delta\approx 38$ meV, in agreement with its estimate from the threshold bias voltage for charging of the traps on the SiO_2–Si_3N_4 interface.

As for the short MNOS transistors (Figs. 5 and 6), in them the field-effect curves and also the function $N_{ss}(G)$ in the weak-inversion region have a different character. In particular, the density of states reveals a distinct peak-like feature. It is remarkable that the position of the peak on the G axis is nearly temperature-independent. Under conditions in which Boltzmann statistics apply, this means that the energy position of the maximum of N_{ss} varies relative to the bottom of the conduction band in proportion to T; consequently, the peak cannot be associated with recharging under field-effect conditions of the interface traps or defects. Note that its appearance also cannot be caused by the concentration dependence of the electron mobility in the inversion channel $\mu_c(n_c)$, which we assume to be weak: measurements of the Hall effect have shown that at $T\geqslant 77$ K in the weak-inversion regime μ_c is determined by mixed scattering of electrons by phonons and charged surface centers and therefore varies weakly with n_c (Ref. 17). In other words, the feature of the density of states in short-channel MNOS transistors cannot be described in terms of interface states, either of ''fluctuational'' origin[5] or bound to concrete surface centers.[8] We especially stress the fact that an increase (by roughly a factor of 2) of the built-in charge concentration has hardly any effect on either the position of the peak of N_{ss} on the G axis or the nature of the dependence of the channel conductance on the gate potential, where this dependence in the weakly opened channel region is not exponential, but linear (see Fig. 7).

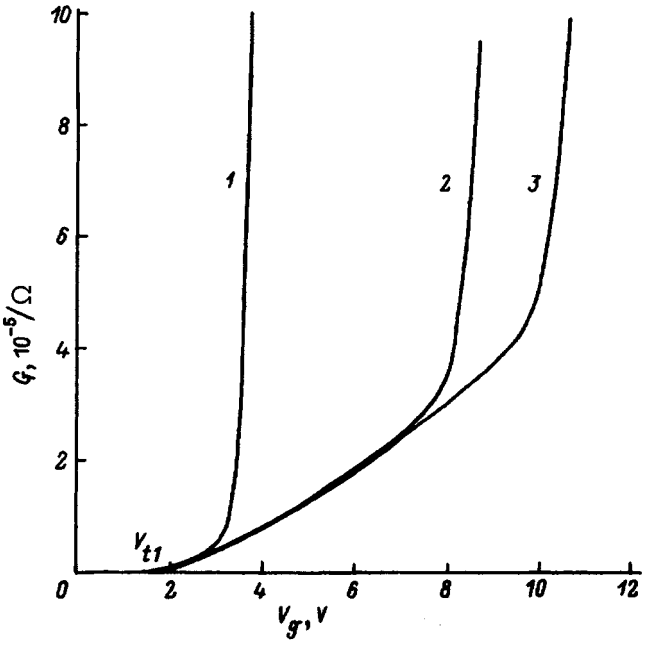

FIG. 7. The dependence $G(V_g)$ for a short Si-MNOS transistor at 77 K for different charge states of the SiO_2–Si_3N_4 interface for $n_t = 2.5\times10^{12}$ (*1*), 5.3×10^{12} (*2*), and 6.3×10^{12} cm^{-2} (*3*).

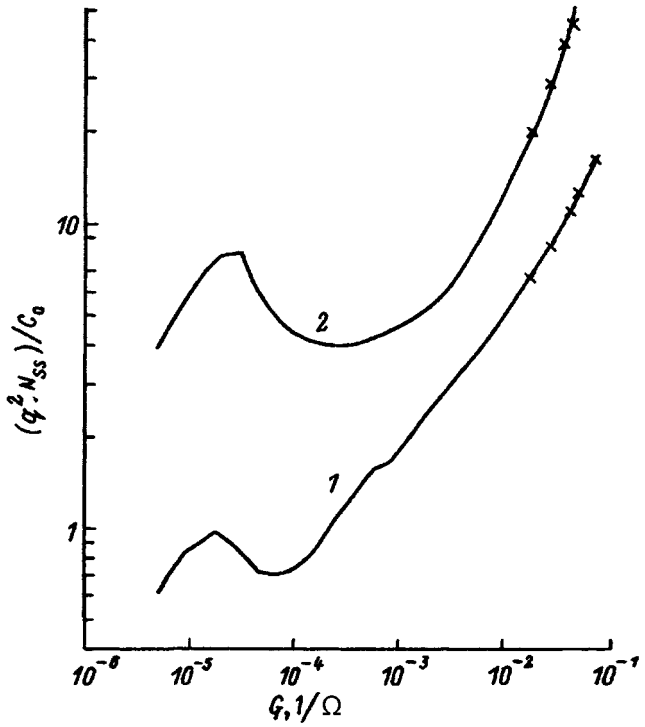

FIG. 8. Effective density of states N_{ss} as a function of G for a GaAs–AlGaAs-HEMT. $T = 300$ K (*1*) and 77 K (*2*).

Another example of short-channel transistors with enhanced concentration of charged centers near the electron channel is afforded by GaAs–AlGaAs-HEMT's with a thin ($\approx$30 Å) spacer, in which the surface fluctuation potential induces ionized donors in the *n*-AlGaAs layer (their typical concentration $N_d \approx 10^{18}$ cm^{-3}). Under the considered conditions $n_t \approx N_d^{2/3}$ (Ref. 11); hence, $\Delta \approx 18$ meV. Figure 8 plots the dependence of $N_{ss}(G)$ for a HEMT with gate length 0.6 μm (gate width 60 μm, distance between source and sink 3 μm), fabricated by molecular-beam epitaxy. As in the case of the Si-MNOS short-channel transistor, the density of states exhibits a peak in the same range of values, $G \approx 10^{-5}-10^{-4}\ \Omega^{-1}$, which is clearly evident at 77 K ($\Delta \gg kT$) and which is barely seen at room temperature ($\Delta \approx kT$).

Somewhat unexpected was the discovery of a similar feature in the effective density of states in the GaAs-based Schottky-gate FET's. In such transistors the channel is formed in the doped *n*-GaAs layer and the conductivity, in general, has a three-dimensional character. At the same time, a number of papers (see Ref. 2) have noted that for sufficiently high depleting voltages the sub-gate region of the channel layer is almost completely depleted of electrons, with the exception of its interface with the semi-insulating substrate in which a quasi-two-dimensional electron channel appears. In this case, electron transport is realized in the fluctuation potential of the ionized donors of the barrier layer, which at 77 K for small n_s satisfies the criterion of a strong fluctuation potential.[18] Figure 9 plots the dependence of the density of states $N_{ss}(G)$ for the GaAs-based Schottky-gate FET (thickness of the *n*-GaAs : Si channel layer 0.15 μm, donor concentration $N_d \approx 3\times10^{17}$ cm^{-3}, gate length 0.8 μm, width 200 μm, distance between source and sink 3 μm). At 77 K it exhibits the above-noted feature in the range $G \approx 10^{-5}-10^{-4}\ \Omega^{-1}$, which disappears at 300 K, reflecting the shift from a strong to a weak fluctuation potential.

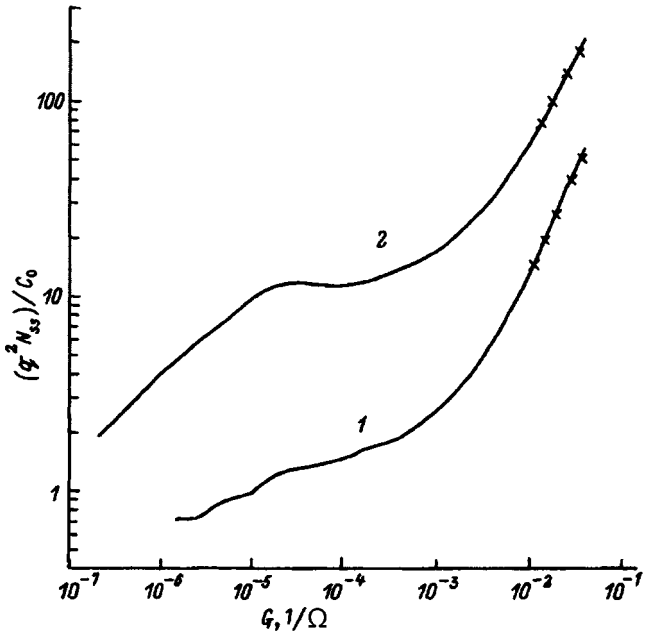

FIG. 9. The same as in Fig. 8, but for a GaAs-based field-effect transistor with a Schottky barrier. $T = 300$ K (*1*) and 77 K (*2*).

4. DISCUSSION AND CONCLUSIONS

Let us summarize what has been presented so far. With the exception of two cases—a weak fluctuation potential (Figs. 1 and 2) and structures with a large gate length (Figs. 3 and 4), in transistor structures with enhanced charge concentration in the sub-gate insulator a peak-like feature arises in the effective density of states. This feature becomes more pronounced as the temperature is lowered and with increasing built-in charge concentration and shortening of the channel. Regardless of variation of the enumerated parameters, of the thickness of the sub-gate insulator, and of the length-to-width ratio of the gate, this peak is observed in the same range of conductance values, $G \approx 10^{-5} - 10^{-4}\ \Omega^{-1} \simeq q^2/h$, which leads to the conclusion that this is a manifestation of the quantum nature of the conductivity of short-channel transistors under conditions of a strong fluctuation potential. Confirmation of this conclusion is provided, in particular, by the absence of a dependence of the conductance of the weakly opened inversion channel of Si-MNOS transistors on the built-in charge concentration (Fig. 7), whereas in the classical regime the conductance G is proportional to the electron mobility, which, because of scattering by surface charge centers, decreases with increasing n_t (Ref. 19). In other words, in this regime one should expect a decrease in the slope of the corresponding dependences in the weak-inversion region.

Let us consider the experimental data pertaining to the Si-MNOS transistor (Figs. 5 and 6), in which, due to the high concentration of built-in charge, the detected effects are manifested even at room temperature. The dependence of N_{ss} on the left side of the peak varies with G according to a power law with an exponent $\alpha \approx 1$ (i.e., $G \propto V_g + \text{const}$), which is characteristic of strong inversion, when the fluctuation potential is almost completely screened (7). In other words, the left side of the peak is, as it were, the dependence $N_{ss}(G)$ in the strong-inversion region ($G \geqslant 10^{-4}\ \Omega^{-1}$) rigidly shifted into the weak-inversion region ($G \leqslant 10^{-5}\Omega^{-1}$). Such a situation can be observed if two transistors with identical gate lengths are switched on in parallel, where the first transistor has a lower threshold voltage V_{t1} (Fig. 7) and a roughly 200 times narrower channel, according to the data in Figs. 5 and 6. The appearance of this additional channel with depressed threshold voltage is, in fact, responsible for the characteristic feature in the effective density of states, which becomes more distinct with increasing separation of the thresholds of these two channels.

The physical picture of the formation of the additional conductivity channel, in our view, looks as follows. In the presence of a strong fluctuation potential ($\Delta \gg kT$) the sub-gate surface of the semiconductor consists of a set of microscopic regions with dimensions on the order of the screening radius of the potential fluctuations, $R_s \approx \min\{d; (n_t/\pi)^{1/2} n_s\}$ (Refs. 5–7). Each of the regions is characterized by some value of the local potential, which fluctuates from region to region within the limits of the amplitude of the fluctuation potential, an estimate of which is given by the rms deviation of the potential from its mean value:

$$\delta\varphi = (\Delta/q)[\ln(1 + R_s^2 z^2)]^{1/2}, \tag{8}$$

where z is the mean distance between the electron channel plane and the built-in charge plane; for an MNOS system $z \approx 30$ Å (the thickness of the SiO_2 layer). In practice, for example, for small n_s, $R_s \approx d$ and exceeds the electron wavelength by several orders of magnitude; therefore, these regions can be characterized by the local conductivity σ, which has exponentially strong spread over the channel surface: $\delta(\ln \sigma) \approx q\delta\varphi/kT \gg 1$. Under these conditions the conductivity is percolational,[3] i.e., stationary trajectories of electron transport exist, which, in systems of unbounded dimensions, form the so-called infinite percolation cluster, in our case a two-dimensional network, whose characteristic cell size is determined by the correlation length

$$L_c \approx R_s(q\,\delta\varphi/kT) \gg R. \tag{9}$$

Obviously, the sample can be considered to be unbounded only when its dimensions are much greater than L_c. As estimate shows, the magnitude of L_c for MNOS structures approaches units of microns, which is commensurate with the gate length of transistors (5 μm). Consequently, their conductivity can manifest mesoscopic effects.

It is especially noteworthy that the width of the objects under consideration is much greater than their length. According to the results of studies which have addressed mesoscopic phenomena in semiconductor structures of small length,[1)] in this situation the dominant role in the conductivity is played by relatively rare, random, low-resistance circuits formed by neighboring regions with conductance substantially exceeding that of the unbounded sample. These low-resistance circuits short out the intermediate region between the current-delivering electrodes (the source and sink).

We believe that it is precisely this mechanism in our case that drives the conductivity of transistors under conditions of a strong fluctuation potential, in particular, the formation of an additional channel with low threshold voltage. It seems that the statistical fluctuations of the density of built-in charges form regions in the channels of transistors having depressed local potential which join together to form a low-resistance circuit—a potential trough. The nodes of this circuit are joined by passes located much lower in energy (in units of kT) than the level of the mean surface potential which determined the percolation level in an unbounded sample. In the early stages of formation of the inversion channel, when the electron concentration at the energy level corresponding to the mean surface potential is exponentially small, the conductance of such a trough exceeds that of the infinite percolation cluster by an order of magnitude. The electrons filling the deepest potential wells in the weakest possible inversion regime, including those that form the given trough, naturally increase its conductance, which is limited by the energy position of the highest region of the bottom of the trough. If the dimensions of this region are commensurate with the electron wavelength, then in the presence of degeneracy its conductance $G_* = 2q^2/h$ (Ref. 21), and in the absence of degeneracy its conductance is determined by the probability of population of the corresponding level and consequently has an activation character: $G \approx G_* \exp(-\varepsilon/kT)$, where ε is the energy separation be-

tween the given level and the Fermi level. In this situation, the dependence $G(V_g)$ is obviously in a certain sense universal.

With increase of V_g, the conductance of the trough grows, tending asymptotically to G_*, which is reached under conditions of degeneracy. In this situation, however, because of the growth of the electron concentration nonlinear screening effects come into play, causing an abrupt decrease of the screening radius R_s and amplitude of the fluctuation potential (8), which is accompanied by a decrease of the correlation length (9). As a result, the system gradually transforms from a percolation system into an effective system whose conductivity is determined by the electron concentration at the level of the mean surface potential,[5] which under the conditions of the experiments corresponds to the transition from the left growing branch of $N_{ss}(G)$ to the analogous right branch. In our opinion, this constitutes the main reason for the fact that the detected feature is observed in different samples in the same range $G \approx G_*$, regardless of their geometry, temperature, or the value of n_t.

We note in conclusion that the identical feature of the field-effect curves for the weakly opened channels (Fig. 7), i.e., the lack of any dependence of the function $G(V_g)$ on the built-in charge concentration, leads to the conclusion that it is possible, in principle, to create a new class of reproducible, radiation-hardened, short-channel transistors based on electron systems of diminished dimensionality with extremely strong fluctuation potential.

We are grateful to E. Z. Meĭlikhov and A. A. Snarskiĭ for helpful discussions.

The work was carried out with the support of the Interdisciplinary Scientific–Technical Program ''Physics of Solid-State Nanostructures'' (Grant No. 1-052), the international association INTAS (Grant No. 93-1403) and the Russian Fund for Fundamental Research (Grant No. 96-02-18429-a).

[1)] As a rule, in the hopping conductivity regime (see, e.g., Refs. 3, 13, 14, and 20 and the references cited there).

[1] A. A. Kal'fa and A. S. Tager, in *Multilayer Semiconductor Structures and Superlattices* [in Russian] (Gor'kiĭ, 1985).
[2] M. Shur, *GaAs Devices and Circuits* (Plenum Press, New York, 1987).
[3] B. I. Shklovskiĭ and A. L. Efros, *Electronic Properties of Doped Semiconductors* (Springer-Verlag, New York, 1984).
[4] J. R. Brews, J. Appl. Phys. **46**, 2181 (1975).
[5] V. A. Gergel' and R. A. Suris, Zh. Éksp. Teor. Fiz. **84**, 719 (1983) [Sov. Phys. JETP **57**, 415 (1983)].
[6] V. A. Gergel' and G. V. Shpatakovskaya, Zh. Éksp. Teor. Fiz. **102**, 640 (1992) [Sov. Phys. JETP **75**, 342 (1992)].
[7] A. L. Efros, F. G. Pikus, and V. G. Burnett, Phys. Rev. B **47**, 2233 (1993).
[8] E. N. Nicollian and J. R. Brews, MOS *Physics and Technology* (Wiley, New York, 1982).
[9] S. M. Sze, *Physics of Semiconductor Devices* (Wiley, New York, 1969).
[10] V. A. Gergel' and A. N. Solyakov, Fiz. Tekh. Poluprovodn. **17**, 1016 (1983) [Sov. Phys. Semicond. **17**, 641 (1983)].
[11] A. S. Vedeneev, V. A. Gergel', A. G. Zhdan, and V. E. Sizov, JETP Lett. **58**, 375 (1993).
[12] B. A. Aronzon, A. S. Vedeneev, A. G. Zhdan, and V. V. Ryl'kov, Mikroelektronika **24**, 452 (1995).
[13] A. O. Orlov, M. E. Raikh, I. M. Ruzin, and A. K. Savchenko, Solid State Commun. **72**, 169 (1989).
[14] A. S. Rylik, A. O. Orlov, and E. I. Laiko, Phys. Low-Dimens. Semicond. Struct. **3**, 67 (1994).
[15] A. S. Vedeneev, A. G. Gaĭvoronskiĭ, and A. G. Zhdan, Fiz. Tekh. Poluprovodn. **26**, 2017 (1992) [Sov. Phys. Semicond. **26**, 1135 (1992)].
[16] A. S. Vedeneev, A. G. Gaĭvoronskiĭ, and A. G. Zhdan, Prib. Tekh. Eksp. **2**, 246 (1992).
[17] M. A. Baĭramov, A. S. Vedeneev, A. G. Zhdan, and B. S. Shchamkhalova, Fiz. Tekh. Poluprovodn. **23**, 1618 (1989) [Sov. Phys. Semicond. **23**, 1001 (1989)].
[18] A. V. Orlov, A. K. Savchenko, and B. I. Shklovskiĭ, Fiz. Tekh. Poluprovodn. **23**, 1334 (1989) [Sov. Phys. Semicond. **23**, 830 (1989)].
[19] M. A. Baĭramov, A. S. Vedeneev, and A. G. Zhdan, Fiz. Tekh. Poluprovodn. **23**, 2122 (1989) [Sov. Phys. Semicond. **23**, 1314 (1989)].
[20] A. I. Yakimov, N. P. Stepina, and A. V. Dvurechenskii, Phys. Low-Dimens. Semicond. Struct. **6**, 75 (1994).
[21] L. I. Glazman, L. I. Lesovik, D. E. Khmel'nitskiĭ, and R. I. Shekhter, Pis'ma Zh. Éksp. Teor. Fiz. **48**, 239 (1988) [JETP Lett. **48**, 258 (1988)].

Translated by Paul F. Schippnick

Kinetics of ion depolarization of Si–MOS structures in the linear voltage sweep regime

A. G. Zhdan, E. I. Goldman, and G. V. Chucheva

Institute of Radio Engineering and Electronics, Russian Academy of Sciences, 141120 Fryazino, Moscow Region, Russia

(Submitted February 17, 1997; accepted for publication May 15, 1997)
Fiz. Tekh. Poluprovodn. **31**, 1468–1473 (December 1997)

A new approach is developed to describe isothermal ion depolarization of Si–MOS structures in the regime of linear variation of the gate electrode potential V_g. The approach is based on the experimentally proven fact of the substantially nonequilibrium nature of ion transport in such structures, with the ions initially localized on the SiO_2/Si interface in shallow bulk traps. Dynamic current–voltage characteristics of the depolarization are calculated on the basis of the thermal-emission mechanism of ion transport through the barrier formed by the polarizing voltage ($V_g>0$). The calculated results afford a good description of the experimental data: narrow current peaks with half-width $\sim kT$ localized near $V_g=0$, their temperature dependence, and the sweep rate and initial ion density at the SiO_2/Si interface. On this basis, the effective ion mobility $\mu\theta=(2.5-11)\times10^{-8}\text{cm}^2/(\text{V}\cdot\text{s})$ (θ is the sticking coefficient), activation energy μ ($E_\mu\cong0.6$ eV) and depth of the bulk traps (trap energy) in SiO_2 ($E_t\cong0.2$ eV) have been found in the temperature range 423–453 K. According to the available data, the values $E_\mu\cong0.6$ eV are characteristic of mobile Na^+ ions. © *1997 American Institute of Physics.* [S1063-7826(97)01312-4]

Isothermal studies of mobile-ion transport processes in the silicon-based metal–oxide–semiconductor (MOS) structure in the dynamic regime should yield extensive and valuable information about the kinetics of ion transport, which substantially influences the stability and duty cycle of MOS devices and integrated circuits.[1,2] Polarization (depolarization) of the insulator caused by varying the field electrode potential V_g at a constant rate $\beta_v=dV_g/dt=\text{const}$ (t is time) manifests itself in the dynamic current–voltage characteristics in a very suitable form for identification—as narrow current peaks, localized near $V_g=0$ (Ref. 3). The small half-width of the peaks ($\sim kT$, where k is the Boltzmann constant, T is absolute temperature) was previously interpreted solely within the context of the assumption of a quasi-equilibrium (Boltzmann) distribution of the ions in the insulator.[4,5] However, such an interpretation flies in the face of the known experimental results. Second, at intermediate temperatures ($T\leqslant500$ K) narrow peaks arise only in the depolarization current–voltage characteristics, while in the polarization regime for the same values of β_v the current describes relatively low, broad maxima, shifted somewhat in the direction of the polarizing voltages[3–5] (Fig. 1). This does not agree with the assumption of quasi-equilibrium, which requires rough equality of the ion fluxes from the Si/SiO_2 interface to the field electrode and in the opposite direction. Second, under quasi-equilibrium conditions the ion density at the Si/SiO_2 interface depends only on V_g, and therefore the current (time derivative of the surface charge) should be directly proportional to β_v, which is not observed in experiment (Fig. 1). The differences in the shape of the polarization and depolarization current–voltage characteristics are indicative not only of the absence of quasi-equilibrium in the ionic subsystem of the insulator, but also localization of the ions at the interface with the metal in states energetically deeper than in the bulk of the SiO_2 layer or in its contact with the Si wafer. Therefore, in the analysis of the depolarization kinetics we can ignore the presence of free ions in the metal electrode.

In this light, we developed, on the basis of the results of detailed experiments on the dynamic ion polarization of Si–MOS structures, develops new ideas about its mechanism, based on the substantially nonequilibrium nature of ion transport in such structures.

The measurements were performed under atmospheric conditions on Al structures (field electrode of area $S=2.4\times10^{-2}$ cm^2), SiO_2 (thermal oxide of thickness $h=1700$ Å, formed in dry oxygen at 1100 °C), and (100)Si (free electron concentration $n=1\times10^{13}$ cm^{-3} at $T=300$ K). Care was taken not to introduce mobile ions into the SiO_2 layer, and the samples chosen for study had positive flat-band voltages ($V_{FB}\geqslant1$ V). The sample was placed in the hermetically sealed chamber on a massive (diameter 110 mm, thickness 6 mm) copper washer with polished chrome-plated surface, which was mounted in a ring bushing of alundum ceramic to the housing of the measurement cell. The washer was heated by a 500-watt halogen lamp placed underneath it with a thyristor-regulated power source. The temperature of the sample was monitored by a copper–constantan thermocouple with an accuracy of ±0.2 °C. The field electrode was in contact with a spring-loaded probe of electrolytically tapered, gold-plated, tungsten wire of diameter 0.5 mm, ensuring electrical contact of the metallized rear face of the silicon wafer with the surface of the washer, which was coated with a thin layer of In–Ga alloy. A special waveform generator was used to produce triangular voltage pulses, which made it possible to assign β_v over a wide range of values. The chamber was hermetically sealed by a metal hood, which also served as an electrostatic screen. Radiation reflectors were placed inside it to ensure a uniform temperature of the working space. The sample was heated to

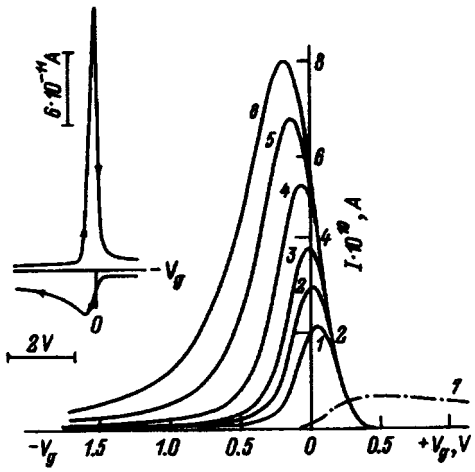

FIG. 1. Dependence of the depolarization current I on the sweep rate β_v for $T=423$ K for $N_{so}\cong 1\times 10^{12}$ cm^{-2}; β_v grows from curve *1* to curve *6* in the sequence 0.02, 0.03, 0.04, 0.06, 0.1, 0.2 V/s. Curve *7* plots the polarization current $[I\cdot(-1\times 10^{10})$, A] for $\beta_v=0.02$ V/s and $T=423$ K. The values of I are measured from the level of the quasi-constant capacitance current. The inset illustrates the substantial qualitative differences in the course of the depolarization (upper curve) and polarization processes (lower curve), $\beta_v\cong 0.02$ V/s, $T=423$ K (compare with the experimental data in Ref. 3.

a prescribed temperature $T_0\geqslant 150$ °C at a moderate depolarizing voltage $V_g\cong 1$ V to eliminate any effects of residual or random polarization. The initial ion density N_{so} at the Si/SiO_2 interface was varied by varying the polarization time ($t\leqslant 5$ min) and voltage ($V_g\leqslant +5$ V) for $T_0=$ const. The values of N_{so} were determined from the area of the depolarization current peaks. The quasi-constant component of the current $I=C_{SiO_2}\cdot\beta_v$ (C_{SiO_2} is the capacitance of the intermediate insulating layer of the MIS structure), which was distinctly manifested in the initial stage of variation of V_g, was subtracted from the total current.

Figures 1 and 2 show typical families of depolarization current–voltage characteristics at $T=423$ K for different values of β_v and N_{so}. It can be seen that for small $\beta<0.06$ V/s the peaks are nearly symmetric; the region of initial current growth coincides for all the curves; as β_v is increased, the amplitude of the current maximum increases and its position is shifted toward depolarizing voltages ($V_g<0$). As N_{so} is increased (Fig. 2), the shape of the peaks remains essentially fixed, their half-width grows somewhat, and the current maximum is shifted toward $V_g>0$.

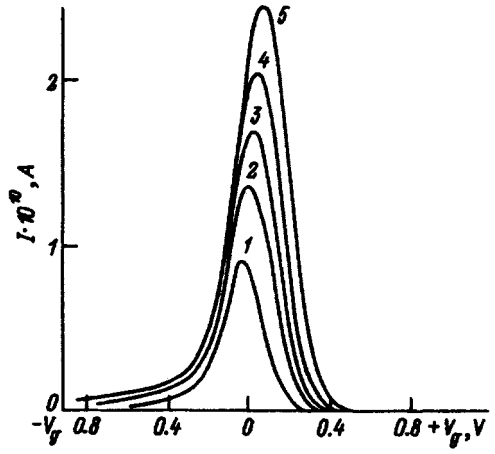

FIG. 2. Dependence of the depolarization current I for $\beta_v=0.02$ V/s on the initial ion density N_{so} at the Si/SiO_2 interface for $T=423$ K. N_{so} grows with curve number in the sequence $(2.8, 4.0, 6.2, 7.0, 8.0)\times 10^{11}$cm^{-2}.

Disregarding the reverse ion flux from the field electrode to the semiconductor on the basis of the above-indicated facts, and noting that in the region of sufficiently large polarizing fields ion depolarization is hindered by a barrier of height $U'=qV_g'$ (q is the elementary charge),[1)] based on the thermal-emission mechanism of transport, we have

$$I=qS\mu N_0\varepsilon_h e^{-qV_g'/kT}, \tag{1}$$

where I is the ion current, S is the area of the structure, μ is the ion mobility, N_0 is the three-dimensional concentration of free ions on the Si/SiO_2 interface, and ε_h is the electric field at the field electrode. Expression (1) remains valid in the presence of ion traps in the insulator or at its interface with the semiconductor, where these traps are at equilibrium with the free charge carriers. The variation of the ion density N_s with time at the Si/SiO_2 interface is governed by the kinetic equation

$$\frac{dN_s}{dt}=-\frac{I}{qS}. \tag{2}$$

We assume that ion traps are absent. Then, for intermediate electric fields ε_h in the oxide and at its interface with the metal ($\varepsilon_h\ll 2\pi qN_s/\varkappa$, where $\varkappa$ is the dielectric constant of the oxide) $N_0\cong 2\pi q^2N_S^2/\varkappa kT$, and it follows from Eqs. (1) and (2) that

$$I=\frac{q^2S\beta_v}{kT}N_{so}\left[\left(\frac{2\pi q\mu\varepsilon_h N_{so}}{\varkappa\beta_v}\right)^{1/2}e^{-\frac{qV_g'}{2kT}}+\left(\frac{2\pi q\mu\varepsilon_h N_{so}}{\varkappa\beta_v}\right)^{-1/2}e^{\frac{qV_g'}{2kT}}\right]^{-2}. \tag{3}$$

It is obvious that expression (3) describes a narrow, symmetric peak $I(V_g)$ with half-width $\Delta_{1/2}=(4kT/q)\ln(1+\sqrt{2})$.

Expression (3) coincides with the expression obtained in Refs. 4 and 5 in the equilibrium approximation to within reassignment of the constants. It would appear that this was the basis for the erroneous interpretation of the depolarization kinetics in the context of the quasi-equilibrium model.

At the current maximum ($I=I_m$, $V_g'=V_{gm}'$) we have

$$e^{\frac{qV_{gm}'}{kT}}=\frac{2\pi q\mu\varepsilon_{hm}N_{so}}{\varkappa\beta_v},\quad I_m=\frac{q^2S\beta_vN_{so}}{4kT}, \tag{4}$$

where ε_{hm} is the electric field for $V_g'=V_{gm}'$; $\varepsilon_{hm}\cong V_{gm}'/h$. As in the case of quasi-equilibrium,[4,5] the current at the maximum grows with increase of β_v and N_{so}; however, in the situation under consideration the position of the peak, V_{gm}', begins to depend on the sweep rate β_v and the initial polarization level N_{so}: as β_v is increased, V_{gm}' shifts toward depolarizing voltages, and as N_{so} is increased, it shifts in the opposite direction. In the region of initial growth $V_g'-V_{gm}'\gg kT/q$ the current is described by expression (1) with $N_0=3\pi q^2N_{so}^2/\varkappa kT$ and does not depend on β_v.

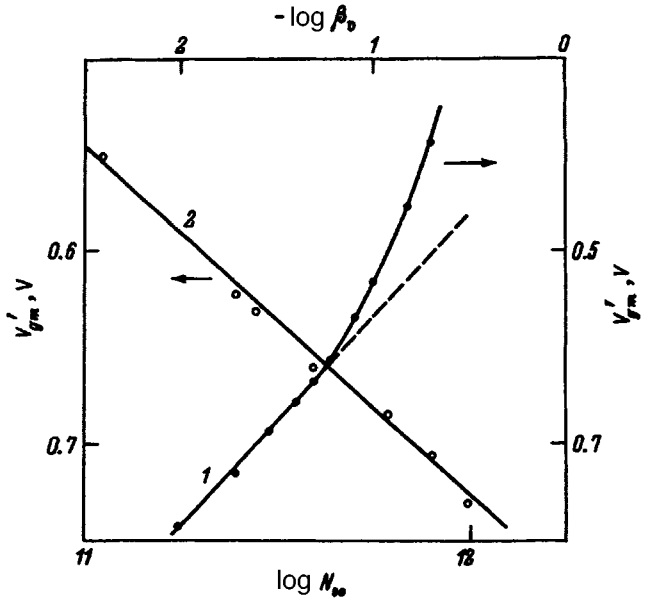

FIG. 3. Dependence of the positions of the maxima of the dynamic current–voltage characteristics $V'_{gm}=V_K+V_{gm}$ on the sweep rate β_v (V/s) for $N_{so}\cong 1\times 10^{12}$ cm^{-2} (*1*) and on the initial ion density N_{so} (cm^{-2}) for $\beta_v=0.02$ V/s (*2*) and $T=423$ K. For curve *1* the V'_{gm} axis is on the right, and for curve *2*, it is on the left.

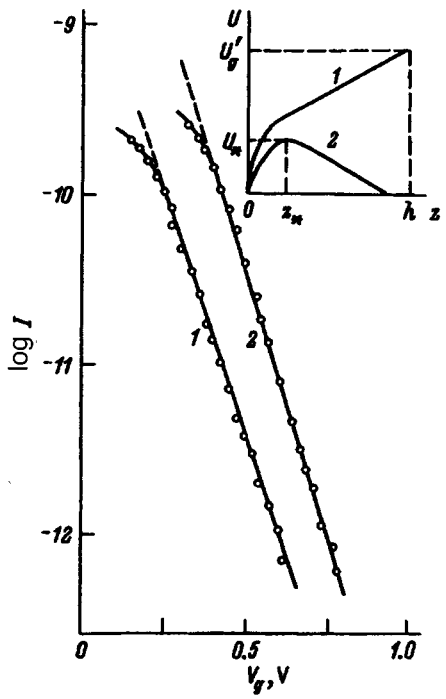

FIG. 4. Dynamic current–voltage characteristics $\log I-V_g$ in the initial growth region of the depolarization at 423 K (*1*) and 453 K (*2*) for $\beta_v=0.02$ V/s and $N_{so}\cong 1\times 10^{12}$ cm^{-2}. The inset shows the qualitative dependence of the potential energy of the ions U in the insulator intermediate layer in the absence (*1*) and presence (*2*) of a built-in barrier created by filling of the bulk ion traps in the SiO_2 surface layer at its interface with the silicon layer. The insulating layer occupies the region $0\leqslant z\leqslant h$, $z=0$ corresponds to the Si/SiO_2 interface and $z=h$, to the boundary of the field electrode.

As can be seen from Figs. 1–3, all the indicated consequences are distinctly manifested in experiment. Figure 3 plots the observed dependence of V'_{gm} on β_v and on N_{so}, which, in agreement with Eq. (4), are linear when plotted on the scales $V'_{gm}-\log\beta_v$ and $V'_{gm}-\log N_{so}$. According to Eq. (4), their slopes should be equal (in absolute value) to $kT/0.43q$. The actual values of these slopes are nearly equal, but approximately two times smaller than the calculated value (2.2 times smaller for curve *1* and 2.1 times smaller for curve *2*, Fig. 3). Correspondingly, the $\log I-V'_g$ curves in the region of initial current growth, $V'_g-V'_{gm}\gg kT/q$, are straight lines whose slopes are less than the theoretical value [see Eq. (1)] by a factor of $\nu=2.05$ (423 K) and $\nu=1.82$ (453 K), respectively (see Fig. 4). The appearance of a nonideality factor $\nu>1$, decreasing with increase of T, is characteristic of thermal-emission phenomena at contacts.[7] It is important to emphasize the closeness of the values of ν found by independent measurements at identical temperatures.

The good agreement between theory and experiment allows us to estimate the ion mobility and its activation energy E_μ. Introducing the coefficient ν into the argument of the exponential in Eq. (4), we obtain

$$\mu\equiv\mu_0 e^{-E_\mu/kT}=\frac{\varkappa\beta_v h}{2\pi q V_{gm}N_{so}}e^{\frac{qV'_{gm}}{\nu kT}}.$$

Substituting the experimental data in this expression [$\beta_v=0.02$ V/s, $h=1.7\times 10^{-5}$ cm, $N_{so}=1\times 10^{12}$ cm^{-2}, $V_K=0.64$ V, $V'_{gm}=0.7$ V (423 K); $N_{so}=0.8\times 10^{12}$ cm^{-2}, $V_K=0.67$ V, $V'_{gm}=0.765$ V (453 K)], and also the most reliable values for ν, found from the slopes of the current–voltage characteristics (Fig. 4) $\nu=2.05$ (423 K) and $\nu=1.82$ (453 K), we find for $\varkappa_{SiO_2}=3.9$: $\mu(423\text{ K})\cong 2.5\times 10^{-8}$, $\mu(453\text{ K})\cong 1.1\times 10^{-7}$ cm^2/(V·s), and $E_\mu\cong 0.8$ eV.

The situation under consideration is realized only for small β_v ($\beta_v<0.06$ V/s, $T=423$ K, Figs. 1–4). As β_v is increased, the nature of the peaks changes radically: they become increasingly more asymmetric, and following the maxima strongly shifted in the direction of $V_g<0$, ''tails'' of a slowly decaying current appear on the curves, and finally the current in the tails generally ceases to depend on V_g, becoming only a function of time t (Fig. 5). The $I(V'_g)$ curves in the region of current growth and the dependence of the voltage positions of their maxima $V'_{gm}(\beta_v)$ ceases to obey relations (1) and (4). These facts point unambiguously to the presence in the SiO_2 layer of ion traps which do not have enough time, for large sweep rates β_v, to empty themselves during the thermal-emission times of free ions through the barrier U'_g and are the reason for the appearance of the classical exponential relaxation law $I\sim e^{-t/\tau_t}$ in the tails of the depolarization curves, τ_t is the lifetime of the ions in the traps (see the insets to Figs. 5 and 6). In this case it is necessary to assume that at the start of the experiment (for large polarizing voltages) essentially all of the ionic charge is concentrated in the traps since for the very fastest sweep rates ($\beta_v>0.2$ V/s) the main contribution to the area of the depolarization peak comes specifically from the exponential tail of the relaxation curves.[2)] This state of affairs is manifested (clearly observed) in the increase with increasing sweep rate β_v of the half-width of the falling branch of the current. The filling of the traps cannot be assumed to have reached its

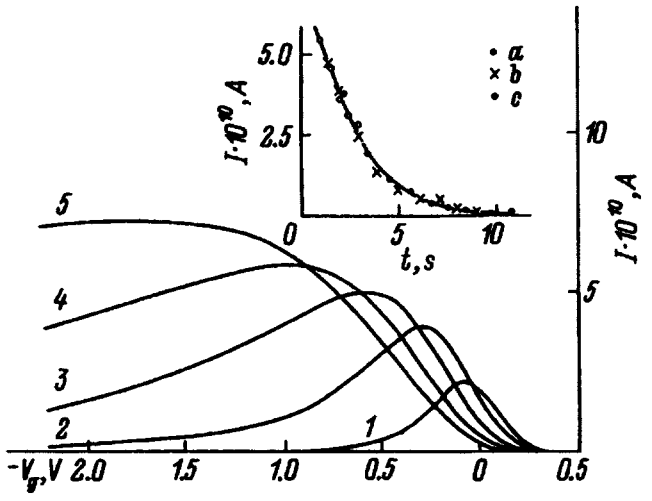

FIG. 5. Dynamic current–voltage characteristics at high sweep rates $I(V_g)$ for $T=423$ K and $N_{so}\cong 7.4\times 10^{11}$ cm^{-2}. β_v grows with curve number in the sequence 0.06, 0.2, 0.5, 1.0, 2.0 V/s. The inset plots the time dependence of the current in the tails of the depolarization curves for $\beta_v=0.5$ (a), 1.0 (b) and 2.0 V/s (c).

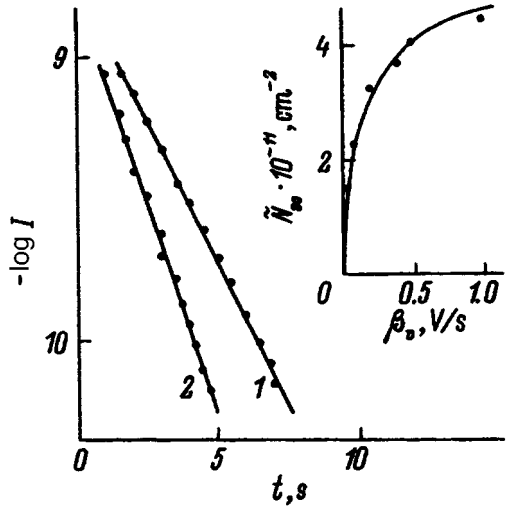

FIG. 6. Semilog plot of the time dependence of the current in the tails of the depolarization curves for $\beta_v=0.5$ V/s: 1) $T=423$ K, 2) $T=453$ K. Curve *2* lies near curve *1* since the relative contribution of the exponential tail to the area of the depolarization peak decreases with increasing temperature. The inset graph plots the ion density $\tilde{N}_{so}$, calculated from the amount of charge passed through the insulator intermediate layer during ''exponential'' relaxation at $T=423$ K, as a function of the sweep rate β_v ($N_{so}\cong 7.4\times 10^{11}$ cm^{-2}).

maximum value, at least not for the values of N_{so} achieved in our experiments: $N_{so}\leqslant 2\times 10^{12}$ cm^{-2}. Otherwise, for large β_v the thermal-emission law of the depolarization kinetics of the free ions (1) should be obeyed on the growing branch of the current for values of N_0 corresponding to the initial polarization state, which contradicts the results of experiment (Fig. 5). Thus, for large U_g', as long as the characteristic thermal-emission time $\tau_e\sim\exp(-U_g'/kT)$ exceeds τ_t, the traps are able to come into equilibrium with the free ions and depolarization of SiO_2 is governed by ion transport through a barrier of height U_g' (the inset in Fig. 4). As U_g' is decreased, the relationship between τ_e and τ_t inverts, depolarization ceases to be limited by the barrier, and as β_v is increased, a continually shrinking part of the polarization charge runs off via the thermal-emission mechanism.

The linearity of the $\log I-t$ curves (Fig. 6) testifies to the single-energy character of the ion traps. This allows us to find the values of $\tau_t\equiv\tau_0 e^{E_t/kT}$ and from their temperature dependence to determine the trap activation energy E_t. On the basis of the data (Fig. 6) we have $\tau_t\cong 2$ s (423 K), 1.4 s (453 K), and $E_t\cong 0.2$ eV.

Two important questions arise: where are these traps located (on the SiO_2 surface of the interface or in the bulk of the SiO_2) and how does the fact of their existence affect the results obtained above within the context of a purely free state of the ions on the SiO_2/Si interface? By analogy with equilibrium electron phenomena in semi-insulators[8] we have for surface traps with concentration N_{st} the result $N_0=N_{1/2}(N_s/N_{st})$, where $N_{1/2}$ is the characteristic concentration of free ions at which the traps are half-filled. Therefore, for small β_v relations (1) and (2) describe an asymmetric peak, which is characteristic of relaxation spectroscopy, with half-width of the growing branch approximately 1.4 times greater than the half-width of the falling branch.[9] Since experiment shows the peaks to be symmetric (Figs. 1 and 2), the traps should be assumed to be distributed in the bulk of the SiO_2 boundary layer adjoining the Si/SiO_2 interface. Assuming that this distribution is uniform, the volume concentration of the traps is equal to N_t, the free and localized ions are at equilibrium, and the potential incursion into the layer of filled traps $(2\pi q^2N_s^2/\varkappa N_t)\leqslant kT$,[3] we have $N_0=\theta\cdot(2\pi q^2N_s^2/\varkappa kT)$, where $\theta=N_{1/2}/N_t$ is the sticking coefficient. Consequently, for small enough N_s and β_v or large enough N_t (in the situation under consideration $N_t\geqslant 6\times 10^{18}$ cm^{-3} is sufficient), as in the case of purely free ions, depolarization should take place as prescribed by Eqs. (1)–(4), but with a renormalized value of the mobility, and the values of μ and E_μ obtained previously should be changed to reflect the actual values of θ and the trap activation energy; i.e., $\mu\to\theta\cdot\mu$ and $E_\mu\to E_\mu+E_t$. This gives the true value $E_\mu\cong 0.6$ eV, which is very close to the activation energy of mobility of Na^+ ions determined by the collision time method for very high $N_{so}(\geqslant 5\times 10^{13}\text{cm}^{-2})$, i.e., for what appears to be maximum filling of the traps (Refs. 1 and 11.[4]) This fact, like the dependence of the shape of the depolarization current peaks on β_v (which are symmetric for small β_v and which exhibits an exponential tail for large β_v), confirms the concept of bulk traps. The maximum sweep rate at which the growing branch of the current can still be described by the ''stationary'' relation (1) is bounded by the rate at which the diffusion-drift equilibrium is set up, the Maxwellian time $\tau_M\sim qh^2/\mu kT$. At 423 K $[\mu=2.5\times 10^{-8}\text{cm}^2/(\text{V}\cdot\text{s})]$ this time is ~ 0.3 s and for $\beta_v>0.05$ V/s is of the order of the characteristic depolarization current growth time. Precisely such a signal delay is observed experimentally, as clearly shown in Fig. 3 (curve *1*) in the form of an abrupt departure of the dependence $\log\beta_v-V_{gm}'$ from the linear law of Eq. (4). The experimental values of V_{gm}' at large values of β_v become noticeably smaller than the theoretical values. Here the delay increases

with increasing value of β_v; i.e., the rate at which the current maximum shifts in the direction of $V_g<0$ increases. As $\beta_v\to\infty$, a progressively increasing fraction of the ions migrates toward the SiO_2/metal interface in an increasingly stronger depolarizing field for $V_g'<0$. Under such conditions, one should see evidence of the well-known effects of space-charge-limited currents, the front fly-by effect,[8,12] dispersive transport,[13,14] etc. It is natural to attempt to observe such effects not in the dynamic sweep regime, but with stepped voltage signals, i.e., for $U_g'=\text{const}$, both in the isothermal and thermally stimulated relaxation regimes.

In summary, the qualitative picture of the kinetics of ion depolarization in the $\beta_v=\text{const}$ regime is extremely simple. In the dielectric interlayer at the silicon surface the ions are localized in shallow bulk traps, where the width of the localization region is less than its maximum corresponding to potential incursion into the layer of filled traps, on the order of E_t/q. For intermediate values of β_v, the depolarization rate is determined by two characteristic times: the time of thermal emission τ_e through the natural barrier created by the polarizing charge ($V_g'>0$), and the lifetime of the ions τ_t in the bulk traps. Therefore, either the quasi-stationary regime of ion transport through a barrier of height U_g' (small β_v) or the classical kinetics of trap emptying (large β_v) is realized, depending on the value of β_v.

The good agreement between the experimental data which we obtained and the results of independent experimental studies testifies not only to the possibilities of inferring the presence of mobile ions in the insulator from the dynamic current–voltage characteristics, and estimating their density, but also to the possibility of determining the leading parameters of ion transport by applying extraordinarily simple methods.

We are grateful to N. F. Kukharskaya and N. I. Tulyakova for constructive assistance on many levels.

[1)]Here and below, the quantity V_g' should be understood as the sum of the applied voltage V_g and V_K, the Al–Si contact potential difference. According to Ref. 6, $qV_k\cong 0.38+\{kT\ln[N_c(T)/n]\}-\{[kT\ln N_c/10^{14}]_{T=300\text{ K}}\}$ eV, where N_c is the effective density of states in the conduction band of Si at the temperature T for $n=10^{13}$ cm^{-3}. For the data plotted in Figs. 1 and 2, $V_K=0.64$ V.

[2)]This is clear from the dependence on β_v of the ion density $\tilde{N}_{so}=\tilde{I}\cdot\tau_t/qS$ ($\tilde{I}$ is the current at the time t corresponding to the transition to the exponential relaxation law). The given dependence has a distinct tendency to saturate at a level near the original value of N_{so} (the inset in Fig. 6).

[3)]If the concentration N_t of the bulk traps is not too large $(2\pi q^2N_s^2)/\varkappa N_t\gg kT$, then a built-in barrier of height U_*' (curve *2* in the inset in Fig. 4) can arise in the surface layer of the insulator adjoining the semiconductor. In this case, the depolarization kinetics becomes different, and emptying of the traps is delayed since delocalization of the ions and their migration to the SiO_2/metal interface become possible only in the region $z>z^*$ (Fig. 4). Such a delay should lead to a non-exponential time dependence of the depolarization current.[10]

[4)]Determination of the trap concentration N_t and, consequently θ, is possible only for values of N_{so} ensuring maximum filling,[8] which we were not able to achieve in our experiments.

[1] J. F. Verwey, E. A. Amerasekera, and J. Bisschop, Rep. Prog. Phys. **53**, 1297 (1990).
[2] G. S. Horner, M. Kleefstra, T. G. Miller, and M. A. Peters, Solid State Technol. **79**, (June, 1995).
[3] M. Kuhn and D. J. Silversmith, J. Electrochem. Soc.: Solid State Science **118**, 966 (1971).
[4] A. G. Tangena, J. Middelhoek, and N. F. de Rooij, J. Appl. Phys. **49**, 2876 (1978).
[5] A. G. Tangena, N. F. de Rooij, and J. Middelhoek, J. Appl. Phys. **49**, 5576 (1978).
[6] S. M. Sze, *Physics of Semiconductor Devices* (Wiley, New York, 1969).
[7] M. Shur, *GaAs Devices and Circuits* (Plenum Press, New York, 1987).
[8] M. Lampert and P. Mark, *Current Injection in Solids* (Academic Press, New York, 1970).
[9] E. I. Goldman and A. G. Zhdan, Semicond. Sci. Technol. **5**, 675 (1990).
[10] E. I. Gol'dman, Fiz. Tekh. Poluprovodn. **31** (in press) (1997).
[11] R. J. Krieger and T. F. Devenyi, Thin Solid Films **36**, 435 (1976).
[12] K. C. Kao and W. Hwang, *Electrical Transport in Solids* (Pergamon Press, Oxford, 1981).
[13] E. W. Montroll and G. Weiss, J. Math. Phys. **6**, 167 (1965).
[14] I. P. Zvyagin, *Kinetic Phenomena in Disordered Semiconductors* [in Russian] (Moscow State Univ. Press, Moscow, 1984).

Translated by Paul F. Schippnick

Characteristics of a far-infrared germanium hot-hole laser in the Voigt and Faraday field configurations

L. E. Vorob'ev, S. N. Danilov, Yu. V. Kochegarov, and D. A. Firsov

St. Petersburg State Technical University, 195251 St. Petersburg, Russia

V. N. Tulupenko

Donbass State Mechanical Engineering Academy, 343916 Kramatorsk, Ukraine
(Submitted November 18, 1996; accepted for publication February 25, 1997)
Fiz. Tekh. Poluprovodn. **31**, 1474–1481 (December 1997)

A far-infrared laser utilizing intersubband transitions of hot holes in germanium with a hole density of 2.5×10^{14} cm^{-3} is investigated in the Voigt and Faraday field configurations. New comparative data for both configurations are given on the field ranges in which lasing takes place, the emission intensity and spectra, and their dependence on the temperature of the crystal. The Voigt configuration is shown to be preferable, having a broader lasing field range, a higher working temperature, a richer emission spectrum, and a higher intensity. Prominent details of the laser characteristics are discussed, and a comparison is made with calculations.
 [S1063-7826(97)02711-7]

INTRODUCTION

Hole population inversion and lasing in the presence of direct transitions of hot holes between the subbands of light holes (LH) and heavy holes (HH) are possible in Ge by virtue of the different dynamics governing the motion of heavy and light holes in momentum space in crossed electric (**E**) and magnetic (**B**) fields (**E**$\perp$**B**) (by virtue of stronger heating of heavy holes compared with light holes in **E**$\perp$**B** fields) (Ref. 1; Fig. 1a).

Many studies of lasers operating on hot holes in germanium[1] and their applications in scientific research have appeared since the 1982 discovery of the stimulated emission of far-infrared radiation from germanium in fields **E**$\perp$**B**, and the number of papers continues to grow both in Russia and in other countries. By far the majority of investigations have been conducted in the Faraday field configuration ($\boldsymbol{\chi}\parallel\mathbf{B}$, where $\boldsymbol{\chi}$ is the light wave vector; Fig. 1b) at liquid-helium temperature. However, it has been remarked, first in Ref. 2 and subsequently in Refs. 3 and 4 that the Voigt configuration ($\boldsymbol{\chi}\perp\mathbf{B}$, Fig. 1b) is more efficient.

An important problem governing the domain of practical application of a laser is how to raise the operating temperature of the crystal. The maximum laser operating temperature in the Faraday field configuration has been estimated on the basis of investigations of the dependence of the emission intensity on the duration of the current pulse: $T=20$ K–30K (Ref. 5). In the Voigt field configuration, however, lasing at liquid-nitrogen temperature has been observed.[2,6,7]

In the present study our objective is to carry out a comparative investigation of the characteristics of a laser utilizing hot holes in germanium in the Voigt and Faraday configurations and to discuss the results in relation to the latter.

1. SAMPLES AND EXPERIMENTAL PROCEDURE

The same *p*-type germanium sample with a hole density $N_p\simeq2.5\times10^{14}$ cm^{-3} (see Fig. 1b) was investigated in the Voigt and Faraday geometries using a semiconfocal resonator. Diffraction by a plane mirror created the radiation output. A mesh of criss-cross grooves was formed on the side faces of the crystal (35×6 mm^2) to exclude total-internal-reflection modes.

The electric field was measured with point probes in the Voigt configuration (Fig. 1b). The field E was found to be approximately 1.6 times smaller than $E_{\text{appl}}=V/h$ in strong magnetic fields (Fig. 1b). For the given sample in the Voigt configuration, in contrast with the Faraday version, the Hall field is zero essentially throughout the entire sample, because it is shorted out by the contacts. In the Faraday configuration the two fields E and V/h almost coincide. The duration of the field pulse was equal to 2 μs.

In the Voigt geometry the sample and heater were placed in a vacuum cavity with a templen (poly-4-methyl-pentene-1 plastic, a counterpart of TPX) window immersed in liquid helium. The sample temperature was measured with a carbon resistor.

The emission spectra were recorded either by means of a diffraction spectrometer or (at temperatures above 4.2 K, when the emission intensity J was small) by means of a novel miniature tunable interferometer with mirrors in the form of floating metal meshes. The contrast was $J_{\max}/J_{\min}\approx8$.

2. RESULTS AND DISCUSSION

A. Range of the Lasing Fields and Emission Intensity

The electric and magnetic field ranges wherein lasing is observed in a germanium sample with $N_p\simeq2.5\times10^{14}$ cm^{-3} are shown in Fig. 2. In contrast with the results of Ref. 3, in which an investigation of a sample with $N_p\simeq6\times10^{13}$ cm^{-3} only at $T=4.2$ K is reported, the lasing range for our samples at $T=4.2$ K is shifted toward higher values of E and B, owing to the higher impurity concentration. As the temperature is raised, the lasing range becomes narrower and shifts toward higher fields. The maximum working temperature attained 28 K for the Faraday configuration and 68 K for the

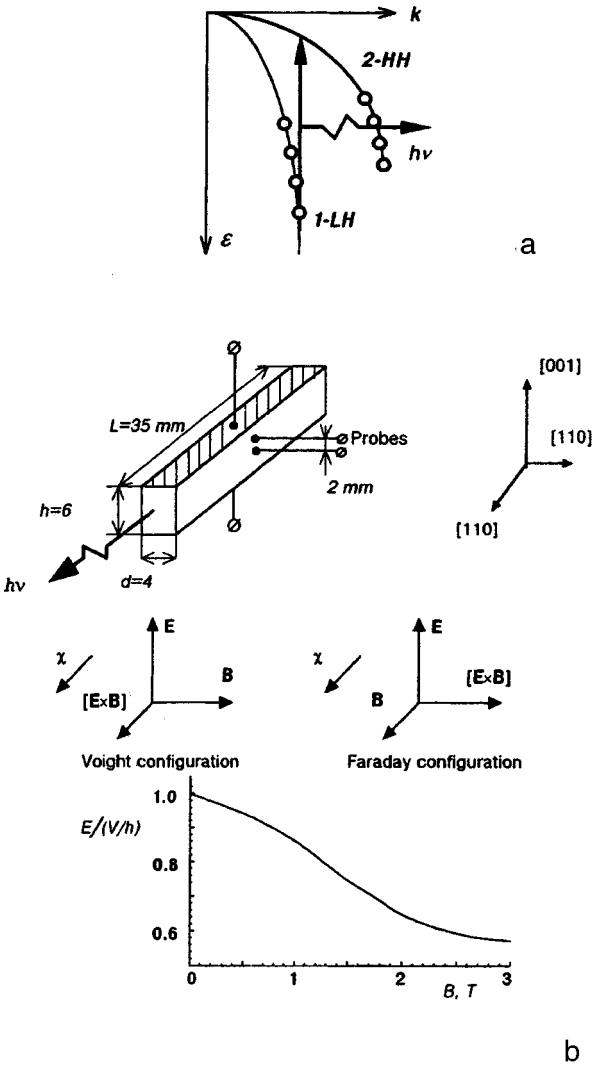

FIG. 1. a) Diagram of direct intersubband hole transitions with the emission of a photon from the light-hole (LH) band 2 to the heavy-hole (HH) band 1. b) Geometry of the *p*-type germanium sample, crystallographic directions, and relative orientations of the electric and magnetic fields; the graph shows the ratio of the electric field measured between probes in the middle section of the sample to the applied field $E_{\text{appl}}=V/h$ as a function of the magnetic field.

Voigt configuration. Lasing in the Voigt configuration at a higher temperature is reported in Refs. 6,7, and 2. It should be noted, however, that both the working temperature and the emission intensity depend on the quality of the crystal (the presence of dislocations, doping homogeneity, and the degree of compensation), the geometry of the sample, and properties of the resonator, the directions of the field relative to the crystallographic axes, and other factors.

The inset to Fig. 2 shows the dependence of the maximum (in the range of lasing fields at a certain temperature) laser emission intensity on the temperature of the crystal. The absolute value of the emission intensity attained several watts. It will be evident below that the spectral range of the emission in the vicinity of the intensity maximum varies only slightly as T increases in the Voigt configuration, obviating the need to correct for the spectral sensitivity of the photodetector.

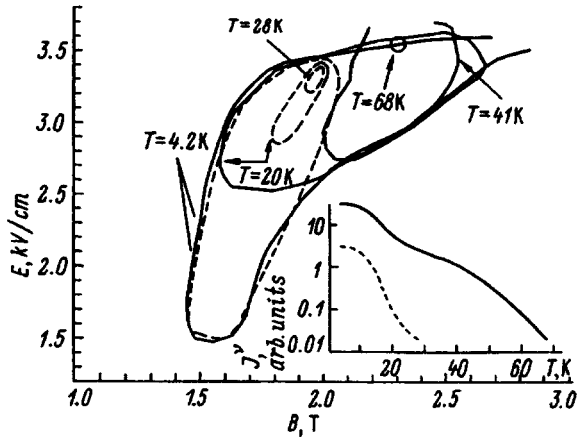

FIG. 2. Field ranges in which far-IR lasing is observed in the Voigt (solid curve) and Faraday (dashed curve) field configurations at various temperatures. Hole concentration $N_p=2.5\times10^{14}$ cm^{-3}. Inset: emission intensity measured by a Ge⟨Ga⟩ photodetector versus crystal temperature for the Voigt and Faraday configurations; the maximum absolute value of the intensity is several watts.

Two main causes are responsible for the decrease in the emission intensity as the temperature increases: a reduction in the amplification of light by free hot holes and an increase in the absorption of radiation by lattice vibrations.

Below we carry out a simplified calculation of the coefficient of absorption of far-IR radiation by hot holes.

The coefficient of absorption (gain for $g<0$) of light by hot holes is

$$g=\alpha_{21}+\alpha_{\text{indir}}, \tag{1}$$

where α_{21} is the absorption coefficient (values of $\alpha_{21}<0$ can lead to light amplification) for direct LH transitions into the HH band $(2\rightarrow1)$, and α_{indir} is the absorption coefficient for indirect intrasubband and intersubband hot-LH and HH transitions involving optical (O) and acoustic (A) phonons and impurities (I). According to Ref. 8,

$$\alpha_{21}=\frac{e^2}{\pi c m_0^2 n\omega}\int_{\mathbf{k}}|\mathbf{e}_\omega\cdot\mathbf{p}_{21}|^2[f_1(\mathbf{k})-f_2(\mathbf{k})] \times\delta[\varepsilon_2(\mathbf{k})-\varepsilon(\mathbf{k})-\hbar\omega]d\mathbf{k}, \tag{2}$$

where m_0 is the free-electron mass, n is the refractive index, $f_2(\mathbf{k})$ and $f_1(\mathbf{k})$ are the distribution functions of hot LH and HH [if $f_2(\mathbf{k})>f_1(\mathbf{k})$, we have $\alpha_{21}<0$, and the amplification of radiation is possible], $\mathbf{e}_\omega$ is the unit vector in the direction of the electric field of the electromagnetic wave, and $\mathbf{p}_{21}$ is the matrix element of the momentum operator. For small values of the quasimomentum k (Ref. 9)

$$|\mathbf{e}_\omega\mathbf{p}_{21}|^2\approx\frac{1}{3}N^2\frac{m_0^2}{\hbar^2}k^2\sin^2(\widehat{\mathbf{e}_\omega\mathbf{k}}), \tag{3}$$

where N is a parameter determined by the band structure. The matrix element averaged over all directions can be written in the form

$$\langle|\mathbf{e}_\omega\mathbf{p}_{21}|^2\rangle=\frac{2}{9}\frac{m_0^2}{\hbar^2}N^2k^2=\hbar^2k^2A_{12}^2. \tag{4}$$

According to Ref. 10, for spherical bands and a parabolic dispersion law

$$A_{12}^2=\frac{1}{8}\left(\frac{m_0}{m_2}-\frac{m_0}{m_1}\right)^2, \tag{5}$$

where m_2 and m_1 are the effective masses of LH and HH.

Equation (2) is transformed as follows for isotropic hot-LH and HH distribution functions:

$$\alpha_{21}=\frac{e^2(m_2^{-1}-m_1^{-1})}{2cn}\,\frac{k^3[f_1(\varepsilon_1)-f_2(\varepsilon_2)]}{\omega}, \tag{6}$$

where $\varepsilon_2(\mathbf{k})=\varepsilon_1(\mathbf{k})+\hbar\omega$.

For indirect transitions involving phonons and impurities the resultant absorption probability is characterized by the difference in the probabilities of induced absorption and emission of photons:

$$w=w^a-w^e, \tag{7}$$

$$w^a=\frac{2\pi}{\hbar}\sum_{\mathbf{k}_0}\sum_{\mathbf{k}_f}\sum_{i,j}|M_{f0}^{ij}|^2 f_i(\mathbf{k}_0)\times[1-f_j(\mathbf{k}_f)]\delta(\varepsilon_f-\varepsilon_0),$$

$$\varepsilon_f-\varepsilon_0=\varepsilon(\mathbf{k}_0)-h\nu\pm\varepsilon_{\rm ph},\quad i,j=1,2. \tag{8}$$

Here $\mathbf{k}_0$ and $\mathbf{k}_f$ are the electron wave vectors in the initial and final states, $\varepsilon_{\rm ph}$ is the phonon energy, and M_{f0} is a composite matrix element incorporating the matrix elements of interaction of an electron with lattice vibrations $H_s^{a,e}$ [with the emission (e) and absorption (a) of phonons] or with impurities H_s and with electromagnetic radiation H_ν,

$$H_\nu=\frac{ie}{n\sqrt{\hbar}}\,\frac{1}{(\nu V)^{1/2}}\left(\mathbf{e}_\omega\cdot\frac{\partial\varepsilon}{\partial\mathbf{k}}\right), \tag{9}$$

where V is the volume of the crystal. For HH transitions within the same band ($1\to1$) and into the LH band ($1\to2$), taking into account intermediate states in bands 1 and 2, we have

$$M_{f0}^{1\to1}=-(H_s^{a,e})^{1\to1}\frac{e\hbar^{1/2}}{2\pi n m_1\nu^{3/2}}\mathbf{e}_\omega\cdot(\mathbf{k}_f-\mathbf{k}_0), \tag{10}$$

$$M_{f0}^{1\to2}=-(H_s^{a,e})^{1\to2}\frac{e\hbar^{1/2}}{2\pi n\nu^{3/2}}\mathbf{e}_\omega\cdot\left(\frac{\mathbf{k}_f}{m_2}-\frac{\mathbf{k}_0}{m_1}\right). \tag{11}$$

To determine the interaction matrix elements for intraband LH transitions $M_{f0}^{2\to2}$ and intersubband LH transitions into the HH band $M_{f0}^{2\to2}$, it is sufficient to replace m_1 by m_2 in Eqs. (10) and (11). From now on, assuming that holes are nondegenerate, we replace $1-f_j(\mathbf{k}_f)$ by 1 in Eq. (8).

The probability of induced photon emission w^e can be calculated analogously. It can also be obtained by making the substitution $h\nu\to-h\nu$ in Eq. (8). The absorption coefficient $\alpha_{\rm indir}=w/(c/n)$.

Calculations show that the main absorption contribution at low temperatures $k_BT\ll\varepsilon_0$ (ε_0 is the optical phonon energy, and k_B is the Boltzmann constant) is from intraband HH $1\to1$ transitions with the emission of optical phonons and with scattering by impurities.

To simplify the calculations, we assume that the hot-HH and LH distribution functions $f_2(\mathbf{k})$ and $f_1(\mathbf{k})$ with respect to the momenta $p=\hbar k$ in fields $\mathbf{E}\perp\mathbf{B}$ are biased Boltzmann distributions,

$$f_i(\mathbf{p})=A_i\exp\frac{(\mathbf{p}-\mathbf{p}_{{\rm dr}\,i})^2}{2m_ik_BT_i},A_i=\frac{\sqrt{2}\pi^{3/2}\hbar^3N_i}{m_i^{3/2}(k_BT_i)^{3/2}},\quad i=1,2, \tag{12}$$

where $\mathbf{p}_{{\rm dr}\,i}$ and T_i are the drift momentum and temperature of hot HH ($i=1$) and LH ($i=2$). The representation of the distribution functions in the form (12) is valid when hole-hole collisions control the rate of dissipation of the energy pulse in both the passive ($\varepsilon<\varepsilon_0$) and the active ($\varepsilon>\varepsilon_0$) energy ranges. The frequency of hole-hole collisions ν_{hh} in germanium at $T_2\approx200$ K for $N_p\approx10^{16}$ cm^{-3} is approximately equal to the reciprocal time constant of optical phonon emission τ_0^{-1}. Consequently, the representation of the distribution functions in the biased Boltzmann form (12) for $n_p\approx2.5\times10^{14}$ cm^{-3} is not entirely correct. Nonetheless, the final results of the calculations using the distribution functions (12) give results qualitatively and even quantitatively closer to those obtained using the exact hole distribution function determined by the Monte Carlo method.

To determine T_i and $\mathbf{p}_{{\rm dr}\,i}$, we use the balance equations for the momentum, power, and number of particles:

$$\mathbf{p}_{{\rm dr}\,i}\left\langle\frac{1}{\tau_i}\right\rangle=e\mathbf{E}+\frac{e}{m_ic}[\mathbf{p}_{{\rm dr}\,i}\times\mathbf{B}]; \tag{13}$$

$$N_i\frac{e}{m_i}\mathbf{p}_{{\rm dr}\,i}\mathbf{E}=N_i\left\langle\left(\frac{d\varepsilon}{dt}\right)_{A+O}^{i\to i}\right\rangle+N_i\left\langle\left(\frac{d\varepsilon}{dt}\right)_{A+O}^{i\to j}\right\rangle-N_j\left\langle\left(\frac{d\varepsilon}{dt}\right)_{A+O}^{j\to i}\right\rangle; \tag{14}$$

$$N_i\left\langle\frac{1}{\tau_{i\to j}}\right\rangle=N_j\left\langle\frac{1}{\tau_{j\to i}}\right\rangle, \tag{15}$$

where the angle brackets signify averaging over the HH distribution function. In Eq. (13)

$$\left\langle\frac{1}{\tau_i}\right\rangle=\frac{4}{3\sqrt{\pi}}\int{\rm e}^{-x_i}\tau_i^{-1}(x_i)x_i^{3/2}dx_i;\quad x_i=\varepsilon/(k_BT_i). \tag{16}$$

In Eqs. (14) and (15) the energy dissipation rate and the frequency of intersubband hole transfers are averaged as follows:

$$\langle\varphi\rangle=\frac{2}{\sqrt{\pi}}\int{\rm e}^{-x_i}\varphi(x_i)x_i^{1/2}dx_i;$$

$$x_i=\varepsilon/(k_BT_i);\quad \varphi(\varepsilon)=\tau_{i\to j}^{-1}(\varepsilon)\ \text{ or }\ d\varepsilon/dt. \tag{17}$$

Solving Eq. (13), we obtain

$$\mathbf{p}_{{\rm dr}i}=m_i\frac{\mu_i\mathbf{E}+\mu_i^2[\mathbf{E}\times\mathbf{B}]/c}{1+\mu_i^2B^2/c^2};\quad \mu_i=\frac{e}{m_i}\left[\left\langle\frac{1}{\tau_i}\right\rangle\right]^{-1}. \tag{18}$$

The left-hand side of Eq. (14), which describes the buildup rate of hole energy in crossed fields $\mathbf{E}$ and $\mathbf{B}$, is now equal to

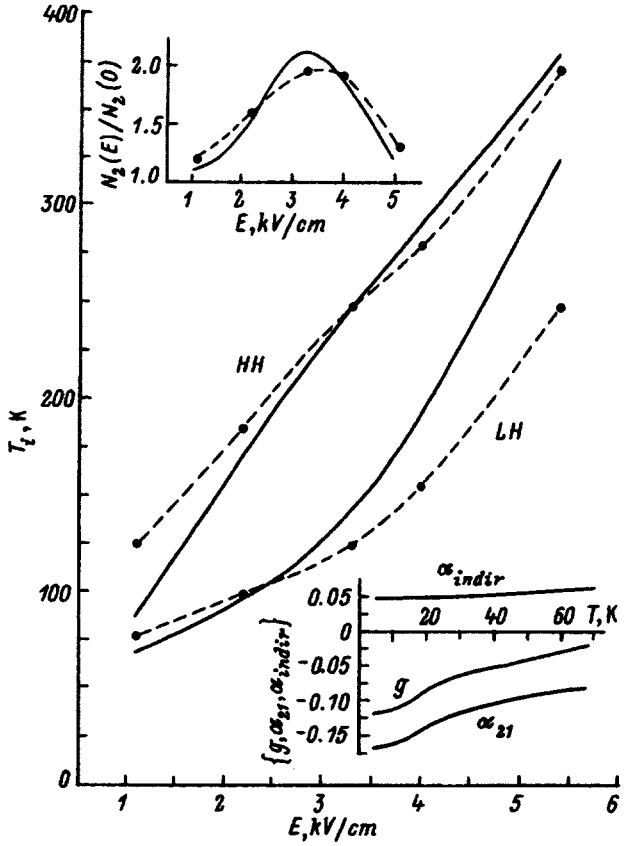

FIG. 3. Temperatures of hot holes (HH) and light holes (LH), calculated from the balance equations for the momentum, power, and number of particles, $T=4.2$ K, $N_p=2.5\times10^{14}$ cm^{-3}, $B=2.2$ T. The points represent experimental values determined from the equation $(3/2)k_BT_i=\langle\varepsilon_i\rangle$, where the average HH ($i=1$) and LH ($i=2$) energies are obtained from experimentally determined hole energy distribution functions.[11] Upper inset: field variation of the LH density; the points represent the density ratio obtained from the experimentally determined LH distribution function.[11]. Lower inset: temperature variation of the light absorption coefficient g (gain for $g<0$) at the maximum of $|g(\lambda,E)|$ for the range of lasing fields in the Voigt configuration (Fig. 2); parameters used in the calculations: $N_p=2.5\times10^{14}$ cm^{-3}, $\lambda\approx100$–120 μm, $B=2.2$ T; also shown are the temperature dependences of α_{21} and α_{indir}.

$$N_i\frac{e}{m_i}\mathbf{E}\cdot\mathbf{p}_{\text{dri}}=N_ie\frac{\mu_iE^2}{1+\mu_i^2B^2/c^2}. \tag{19}$$

It follows from Eq. (19) that in a certain interval of E and B, wherein $\mu_1B/c\leqslant1$ and $\mu_2B/c>1$, the HH energy buildup rate is higher than the LH rate, and $T_1>T_2$, despite the strong intersubband scattering of holes during the emission of optical phonons and scattering by acoustic phonons and impurities. The more pronounced increase in intersubband HH scattering in comparison with LH in a field $\mathbf{E}\perp\mathbf{B}$ (due to the higher average HH energy) causes the LH density N_2 to increase and, accordingly, the HH density N_1 to decrease.

To illustrate the foregoing, Fig. 3 shows calculated curves of T_1, T_2, and $N_2(E)/N_2(0)$ [$N_2(0)$ is the LH density at $E=B=0$] as functions of E in crossed fields $\mathbf{E}$ and $\mathbf{B}$. Also shown for comparison are the HH temperatures and the ratio $N_2(E)/N_2(0)$ obtained from experimentally determined HH and LH distribution functions.[11] Good agreement is noted between the experimental and calculated results.

The light absorption coefficient (gain) g ($g<0$ corresponds to amplification) is also calculated by the above-described scheme. the lower inset in Fig. 3 shows a graph of $g(T)$ for those values of $h\nu$, E, and B from the lasing ranges in the Voigt configuration (Fig. 2) at which $|g|$ is a maximum. Clearly, $|g(T)|$ decreases as T increases, owing to the increase in scattering by acoustic phonons as T increases and, accordingly, to the decrease in α_{21} (α_{indir} is almost totally independent of T).

The experimentally determined emission intensity (see the inset to Fig. 2) decays far more rapidly. Even though J^ν is not directly proportional to g in the linear regime,[12] it still follows from a comparison of the data in the inset to Fig. 2 and the lower inset to Fig. 3 that other factors influence the $g(T)$ curve as well. One such factor might be the sharp increase of the multiphonon light absorption coefficient α_{lat} as T increases.[13] In this event we have in place of Eq. (1)

$$g=\alpha_{21}+\alpha_{\text{indir}}+\alpha_{\text{lat}}. \tag{20}$$

The following two-phonon and three-phonon light absorption processes contributing to α_{lat} are possible at wavelengths $\lambda\approx100$ μm in germanium: TO–LA, LA–TA, TO + TA–LO (Ref. 13). For two-phonon processes $\hbar\omega=\hbar\omega_{q_1}-\hbar\omega_{q_2}$, and the temperature dependence is expressed as $\alpha_{\text{lat}(T)}\sim n_{q_2}-n_{q_1}$, where $n_{q_i}=[\exp(\hbar\omega_{q_i}/k_BT)-1]^{-1}$. For the three-phonon process we have $\hbar\omega=\hbar\omega_{q_1}+\hbar\omega_{q_2}-\hbar\omega_{q_3}$ and $\alpha_{\text{lat}}(T)\sim n_{q_3}(1+n_{q_2}+n_{q_1})-n_{q_1}n_{q_3}$. In all these cases the temperature dependence $\alpha_{\text{lat}}(T)$ is fairly strong, as observed experimentally.[14] Four-phonon and higher-order processes can also contribute significantly to light absorption by virtue of the large number of distinct combinations of phonons with various wave vectors $\mathbf{q}_i$ near the boundary of the Brillouin zone.

Comparing the numerical values of $\alpha_{21}+\alpha_{\text{indir}}$ and α_{lat} from Ref. 14, we conclude that the working temperature of the laser is restricted primarily by the sharp increase in α_{lat} with increasing temperature T.

B. Emission Spectra

The emission spectra of the hot-hole laser has been investigated by various authors in the past.[1] Almost all the spectra have been obtained in the Faraday configuration and mainly for relatively pure germanium samples ($N_p<10^{14}$ cm^{-3}). In such samples the details of the inversion mechanism and the principal characteristics of stimulated emission near liquid-helium temperature can be described qualitatively by analyzing the almost ballistic (collisionless) motion of heavy and light holes in the passive energy range $\varepsilon<\varepsilon_0$ (Ref. 15). At high hole (and impurity) concentrations or at higher lattice temperatures it is more practical to approach the qualitative description in the diffusion-drift model,[16] as reflected in the system of equations (13)–(16).

The emission spectra of pure samples in the Faraday configuration have two lasing ranges, a short-wavelength range $\lambda\approx70$–120 μm and a long-wavelength range $\lambda\approx170$–210 μm (Ref. 1). Lasing usually does not occur in the interval between these ranges, possibly because light is

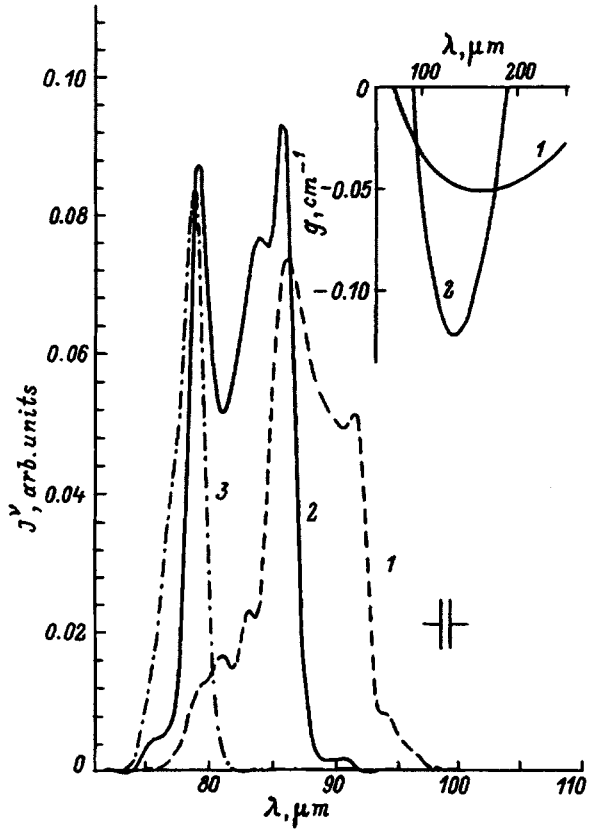

FIG. 4. Emission spectra of a Ge hot-hole laser in the Faraday geometry, Here J^{ν} denotes the signal recorded by the detector, $T=4.2$ K, $N_p=2.5\times10^{14}$ cm^{-3}. *1)* $B=1.5$ T, $E=2.4$ kV/cm; *2)* $B=1.8$ T, $E=2.9$ kV/cm; *3)* $B=2.1$ T, $E=3.2$ kV/cm. Inset: calculated spectral dependence of the light absorption coefficient for two samples with different hole and impurity concentrations, $T=4.2$ K, $B=1.54$ T, $E=2.4$ kV/cm. *1)* $N_p=6\times10^{13}$ cm^{-3}, $N_I=1.2\times10^{14}$ cm^{-3}; *2)* $N_p=4.8\times10^{14}$ cm^{-3}, $N_I=9.6\times10^{14}$ cm^{-3}.

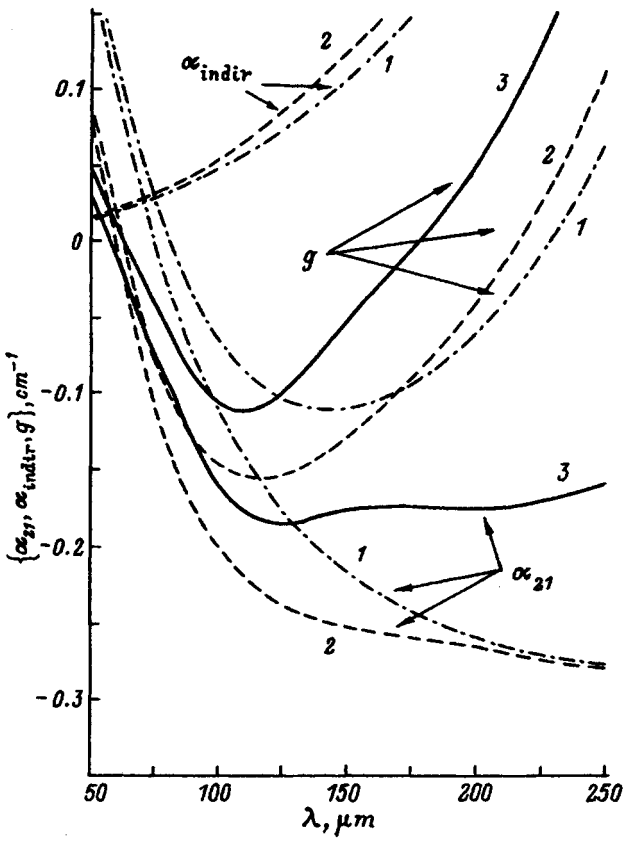

FIG. 5. Spectral dependence of the absorption coefficient (gain for $\alpha_{21}<0$ and $g<0$) for various electric and magnetic fields. The dotted and dashed curves represent the results of calculations using the Boltzmann energy distribution functions of heavy and light holes (12), $T=4.2$ K, $N_p=2.5\times10^{14}$ cm^{-3}, $N_I=5\times10^{14}$ cm^{-3}. *1)* $B=1.5$ T, $E=2.4$ kV/cm; *2)* $B=2.2$ T, $E=3.3$ kV/cm. The solid curves give the results of calculations of α_{21} and g using experimentally determined distribution functions[11], $T=4.2$ K, $N_p=2.5\times10^{14}$ cm^{-3}, $B=2.2$ T, $E=3.3$ kV/cm.

absorbed by impurities, some of which remain filled with holes in a strong field.[17,18] The long-wavelength range does not exist in more highly doped regions (Fig. 4). Its absence is probably attributable to the abrupt increase in the absorption coefficient in the presence of indirect transitions involving impurities, which increases as $\alpha_{\text{indir}}\sim N_I N_p \lambda^m$ (N_I is the concentration of ionized impurities, including acceptors and donors: $N_I=N_A+N_D$). A calculation shows that $m\approx3.5$ in the long-wavelength IR range ($\lambda\approx70$–250 μm). For absorption involving optical phonons $\alpha_{\text{indir}}\sim N_p\lambda^m$, and $m\approx2$ for the same range. The $g(\lambda)$ curves for samples with two different hole densities (see the inset to Fig. 4) exhibit a sudden drop in the gain in the long-wavelength spectral range for a sample having a high impurity concentration.

As mentioned earlier (for pure samples),[1] the emission spectrum shifts into the short-wavelength region when the electric and magnetic fields are increased (Fig. 4). This behavior is consistent with the calculations (Fig. 5). It is evident from Fig. 5 that the maximum gain shifts into the short-wavelength range as E and B increase. The same figure shows curves of α_{21} and $g=\alpha_{21}+\alpha_{\text{indir}}$, for which the absorption coefficient (gain) α_{21} associated with direct intersubband transitions has been found from Eq. (5) using experimental values[11] of $f_2(\varepsilon_2)$ and $f_1(\varepsilon_1)$, rather than the Boltzmann distribution functions (12). Clearly, qualitative agreement prevails for the $g(\lambda)$ curves obtained using both the experimentally determined distribution functions and those approximated by Boltzmann distributions (12) with the calculated values of T_i and $\mathbf{v}_{\text{dr}\,i}$.

Figure 6 shows the emission spectra of the same sample that had been investigated in the Faraday geometry (Fig. 4), but now for the Voigt configuration. As in the Faraday geometry, the spectra shift toward the short-wavelength end as E and B are increased. In addition to the higher emission intensity relative to the Faraday configuration (cf. Fig. 4), we also observe a flareup of the long-wavelength lasing range. This range has not been observed before in samples with $N_p>10^{14}$ cm^{-3}. Its occurrence implies an increase in the gain in the Voigt configuration over the Faraday configuration.

The emission intensity falls off abruptly as the temperature of the crystal increases. The emission spectra were therefore investigated by means of a high-transmission, tunable Fabry-Perot interferometer. The inset to Fig. 6 shows one of the interferograms, from which the emission spectrum is found by forming the inverse Fourier transform. Figure 7

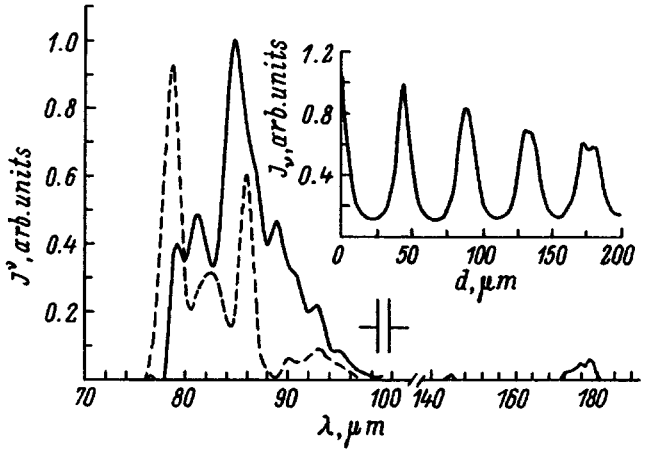

FIG. 6. Emission spectra of a Voigt-configured laser for the same sample as that investigated in the Faraday geometry (see Fig. 4). Here J^ν denotes the signal recorded by the detector, $T=4.2$ K, $N_p=2.5\times10^{14}$ cm^{-3}. *1)* $B=1.54$ T, $E=3$ kV/cm; *2)* $B=1.71$ T, $E=4$ kV/cm. Inset: intensity of laser radiation transmitted through the interferometer versus distance d between the interferometer mirrors; the semitransparent mirrors are flat metal meshes with a reflection coefficient $R\approx0.68$; the temperature of the laser crystal is $T=4.2$ K, $N_p=2.5\times10^{14}$ cm^{-3}, $B=1.54$ T, $E=3$ kV/cm; Voigt geometry.

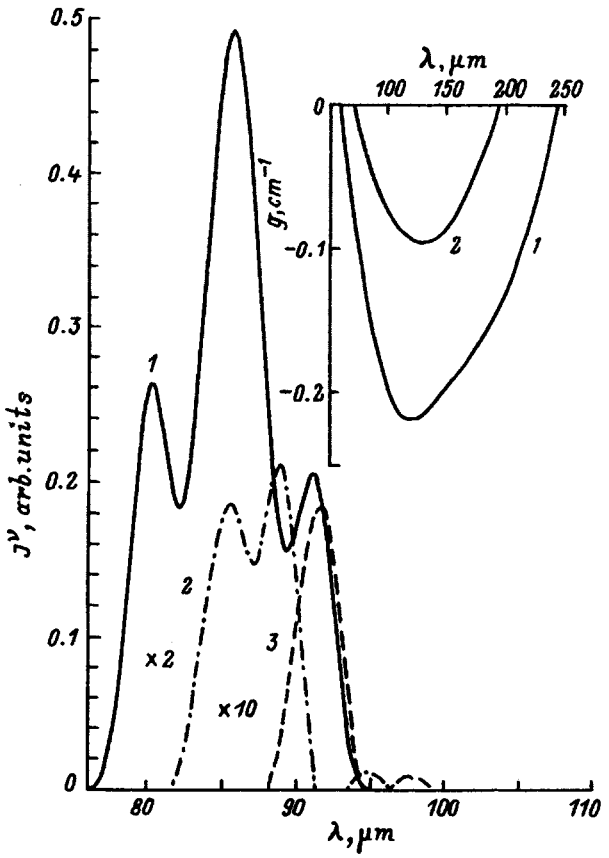

FIG. 7. Laser emission spectra in the Voigt configuration, determined from an analysis of interferograms similar to the one in the inset to Fig. 6, $N_p=2.5\times10^{14}$ cm^{-3}. *1)* $T=4.2$ K, $B=1.54$ T, $E=3$ kV/cm; *2)* $T=24$ K, $B=2.3$ T, $E=3.5$ kV/cm; *3)* $T=43$ K, $B=2.3$ T, $E=3.5$ kV/cm. Inset: absorption coefficient versus light wavelength at two temperatures, calculated for a sample with $N_p=2.5\times10^{14}$ cm^{-3} and $N_I=5\times10^{14}$ cm^{-3}. *1)* $T=4.2$ K, $B=1.54$ T, $E=3$ kV/cm; *2)* $T=43$ K, $B=2.3$ T, $E=3.5$ kV/cm.

shows the resulting emission spectra. The electric and magnetic fields were chosen to maximize the emission intensity at a given temperature.

We see at once that the spectra obtained at $T=4.2$ K for the same fields, using the spectrometer and the tunable interferometer, are similar (Figs. 6 and 7). Not only does the emission intensity decrease with increasing temperature, but there is also a noticeable shift of the emission spectrum into the long-wavelength range. The inset to Fig. 7 shows the spectral dependence of the gain g, calculated for the same values of T, E, and B as those used in finding the emission spectra (Fig. 7). It is evident that the maximum of $|g|$ shifts slightly toward longer wavelengths as T increases. Most likely, however, a more important cause of the shift of the emission spectrum is the decrease in the light absorption coefficient by lattice vibrations at higher values of λ, a trend that is especially conspicuous at $T>30$ K (Ref. 14). We also note that lasing takes place in a narrow spectral interval at $T>40$ K in the Voigt configuration. In this case the lasing frequency is equal to twice the light-hole cyclotron frequency. Lasing at twice the cyclotron frequency has been observed previously in pure samples in the Faraday configuration.[19] It was reasonable to assume that light amplification in hole transitions between the LH and HH bands and between LH Landau levels produces the narrow emission line in the Voigt geometry at $T>40$ K. It follows from calculations of the gain of polarized light in hole transitions between the LH and HH subbands[20] that the gain is a maximum in the short-wavelength range for light with polarization $\mathbf{e}_\omega\|\mathbf{B}$, which is impossible in the Faraday configuration. It should be noted, however, that radiation with this polarization is not active in cyclotron resonance.

This work has received support from the Russian Fund for Fundamental Research (RFFI Grant 96-02017404), a joint grant from RFFI and the International Association for the Promotion of Cooperation with Scientists from the Independent States of the Former Soviet Union (RFFI-INTAS Grant 00615), and from the State Committee on Science and Technology of the Russian Federation (GKNT RF Grant 1-093/4).

[1] Opt. Quantum Electron. **23**, 2 (1991) (Special Issue on Far-Infrared Semiconductor Lasers).
[2] L. E. Vorobiev, S. N. Danilov, and V. I. Stafeev, Opt. Quantum Electron. **23**, S221 (1991).
[3] I. Hosako and S. Komiyama, Semicond. Sci. Technol. **7**, B645 (1992).
[4] L. E. Vorobjev, S. N. Danilov, D. V. Donetsky, D. A. Firsov, Yu. V. Kochegarov, and V. I. Stafeev, Semicond. Sci. Technol. **9**, 641 (1994).
[5] A. A. Andronov, A. M. Belyantsev, E. P. Dodin, V. I. Gavrilenko, Yu. L. Ivanov, V. A. Kozlov, Z. F. Krasinik, L. S. Mazov, A. V. Muravjov, I. M. Nefedov, V. V. Nikonorov, Yu. N. Nozdrin, S. A. Pavlov, V. N. Shastin, V. A. Valov, and Yu. B. Vasil'ev, Physica B **134**, 210 (1985).
[6] L. E. Vorob'ev, F. I. Osokin, V. I. Stafeev, and V. N. Tulupenko, JETP Lett. **35**, 440 (1982).
[7] L. E. Vorob'ev, S. N. Danilov, and V. I. Stafeev, Fiz. Tekh. Poluprovodn. **21**, 1271 (1987) [Sov. Phys. Semicond. **21**, 770 (1987)].
[8] E. O. Kane, J. Phys. Chem. Solids **1**, 82 (1956).
[9] A. H. Kahn, Phys. Rev. **97**, 1647 (1955).
[10] Yu. T. Rebane, Fiz. Tekh. Poluprovodn. **14**, 289 (1980) [Sov. Phys. Semicond. **14**, 169 (1980)].
[11] L. E. Vorob'ev, V. I. Stafeev, V. N. Tulupenko, Yu. K. Pozhela, E. V. Starikov, and P. N. Shiktorov, Fiz. Tekh. Poluprovodn. **19**, 62 (1985)

[Sov. Phys. Semicond. **19**, 37 (1985)]; Fiz. Tekh. Poluprovodn. **19**, 708 (1985) [Sov. Phys. Semicond. **19**, 435 (1985)].
[12] L. E. Vorob'ev, S. N. Danilov, and V. I. Stafeev, Fiz. Tekh. Poluprovodn. **21**, 1707 (1987) [Sov. Phys. Semicond. **21**, 1032 (1987)].
[13] *Semiconductors and Semimetals*, Vol. 3: *Optical Properties of III-V Compounds*, edited by R. K. Willardson and A. C. Beer (Academic Press, New York, 1967) [Russ. trans., Mir, Moscow, 1970)].
[14] R. Brazis and F. Keilmann, Solid State Commun. **70**, 1109 (1989).
[15] A. A. Andronov, V. A. Kozlov, L. S. Mazov, and V. N. Shastin, JETP Lett. **30**, 551 (1979).
[16] L. E. Vorob'ev, S. N. Danilov, V. I. Stafeev, and V. N. Tulupenko, Fiz. Tekh. Poluprovodn. **21**, 1600 (1987) [Sov. Phys. Semicond. **21**, 969 (1987)].
[17] C. Kremser, W. Heiss, K. Unterrainer, E. Gornick, E. E. Haller, and W. L. Hansen, Appl. Phys. Lett. **60**, 1785 (1992).
[18] W. Heiss, K. Unterrainer, E. Gornick, W. L. Hansen, and E. E. Haller, Semicond. Sci. Technol. **9**, S638 (1994).
[19] A. V. Murav'ev, Yu. N. Nozdrin, and V. N. Shastin, JETP Lett. **48**, 261 (1988).
[20] E. V. Starikov and P. N. Shiktorov, Opt. Quantum Electron. **23**, S177 (1991).

Translated by James S. Wood

Amplification of radiation in the far infrared range by hot holes in germanium in crossed electric and magnetic fields

L. E. Vorob'ev, S. N. Danilov, Yu. V. Kochegarov, and D. A. Firsov

St. Petersburg State Technical University, 195251 St. Petersburg, Russia

V. N. Tulupenko

Donbass State Mechanical Engineering Academy, 343916 Kramatorsk, Ukraine
(Submitted January 13, 1997; accepted for publication February 25, 1997)
Fiz. Tekh. Poluprovodn. **31**, 1482–1486 (December 1997)

The results of direct gain measurements are reported for the amplification of polarized and unpolarized, long-wavelength, infrared radiation by hot holes in germanium in crossed electric and magnetic fields in the Voigt and Faraday configurations. The experimental data are compared with gain calculations. © *1997 American Institute of Physics.* [S1063-7826(97)02811-1]

INTRODUCTION

Since 1982, when stimulated radiation in the far-infrared range was observed for the first time, studies of far-IR lasers utilizing intersubband transitions of hot holes in germanium have been reported in many papers (see Ref. 1). Interest in such lasers and their applications have not waned in recent times among scientists either in Russia or elsewhere in the world. To date, however, the optical gain g[1)] has not been measured by direct means. Various authors' calculations of g for light wavelengths in the vicinity of $\lambda=100\ \mu$m in an electric field $E=2$ kV/cm and in a magnetic field $B=2$ T at a hole density $N_p=10^{14}\ \text{cm}^{-3}$ and at a temperature $T=20$ K give an approximate value of the amplification cross section $\sigma_{\text{amp}}=g/N_p=-(5-6)\times10^{-16}\ \text{cm}^2$ (Ref. 1). The calculated value $\sigma_{\text{amp}}\approx-2\times10^{-15}\ \text{cm}^2$ is given in Ref. 2. Only one experimental paper[3] has been published.[2)] In this study[3] the gain has been determined experimentally in the Faraday field configuration ($\boldsymbol{\chi}\|\mathbf{B}$, where $\boldsymbol{\chi}$ is the light wave vector) for samples with hole densities $N_p\approx4.5\times10^{13}\ \text{cm}^{-3}$ and $1.7\times10^{14}\ \text{cm}^{-3}$ at $T=4.2$ K, in this case from the transient-rise kinetics of the intensity of stimulated emission. According to Ref. 3, the gain is $g=-7.4\times10^{-3}\text{cm}^{-1}$ at $E=1.2$ kV/cm and $B=0.77\ T$ for the first density, and $g=-2.7\times10^{-2}\text{cm}^{-1}$ at $E=1.6$ kV/cm and $B=1.14\ T$ for the second density (the corresponding amplification cross sections are $\sigma_{\text{amp}}\approx-1.64\times10^{-16}\ \text{cm}^2$ and $-1.59\times10^{-16}\ \text{cm}^2$). These values are lower than the calculated results.

A high emission intensity and broadening of the lasing range in the Voigt field configuration ($\boldsymbol{\chi}\perp\mathbf{B}$) relative to the Faraday configuration has been reported in Refs. 5–7. However, the optical gains have yet to be determined directly for either configuration.

The objective of the present study is to determine by direct means (from the amplification of radiation in the far-IR range) the optical gains of hot holes in germanium in fields $\mathbf{E}\perp\mathbf{B}$ for the Voigt and Faraday geometries.

A diagram of the hole transitions responsible for the amplification of light is shown in Fig. 1. The population inversion of hot holes is possible in crossed electric and magnetic fields within a bounded domain of $\mathbf{E}$ and $\mathbf{B}$ (Ref. 1). Under these conditions the optical gain at low lattice temperatures, when light absorption by lattice vibrations in multiphonon processes can be ignored, is

$$g=\alpha_{21}+\alpha_{\text{indir}}, \tag{1}$$

where α_{21} is the absorption (for $\alpha_{21}>0$) or gain (for $\alpha_{21}<0$) of radiation in direct transitions between the light-hole (LH, curve *1*) and heavy-hole (HH, curve *2*) subbands, and α_{indir} is the light absorption coefficient in indirect intrasubband and intersubband hot-hole transitions involving acoustic and optical phonons and impurities. The coefficients α_{21} and α_{indir} are functions of E and B.

SAMPLES AND EXPERIMENTAL PROCEDURE

Germanium samples with hole densities $N_p\approx2.5\times10^{14}\ \text{cm}^{-3}$ and $6\times10^{13}\ \text{cm}^{-3}$ were used. The shape and dimensions of the samples are shown in Fig. 1. In the Voigt geometry the electric field was determined from the voltage drop between probes in the middle of the sample. The spacing of the probes was equal to 2 mm. The field in the middle part of the sample, measured by this procedure, was approximately 1.6 times lower than the ratio U/h, where U is the voltage applied to the sample. The electric field pulse had a duration $\Delta t=1.8\ \mu$s.

The gain was measured as follows. The beam from a far-IR hot-hole laser emitting approximately at the wavelength $\lambda\approx92\ \mu$m was transmitted through an iris with dimensions smaller than the area of the face on which the beam was incident. This scheme prevented the measurement of g from being influenced by the geometrical dimensions of the crystal. To preclude the influence of multiple reflections and other undesirable effects, the faces through which the beam entered and exited the sample were out of parallel by as much as 3°. The intensity J of the radiation transmitted through the sample (of thickness L) was compared with the intensity J_0 of radiation transmitted through a thin, high-resistance germanium wafer (of thickness $l\ll L$). The intensity ratio is

$$J/J_0\approx\exp(-gL). \tag{2}$$

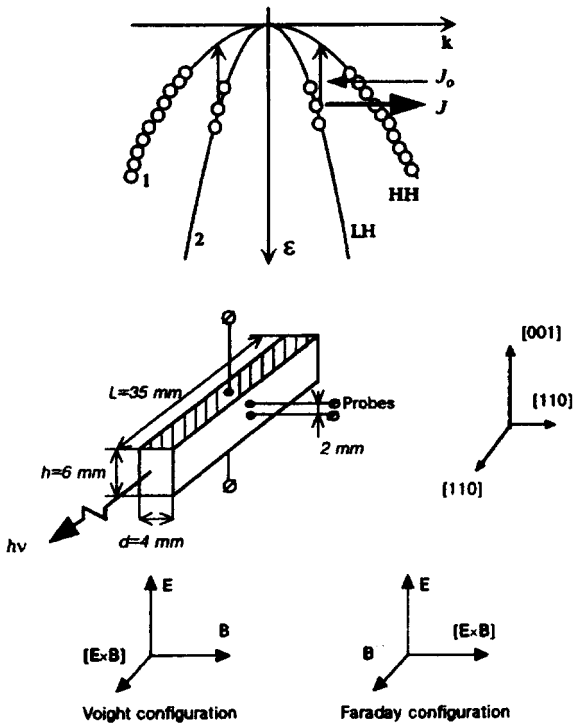

FIG. 1. a) Schematic diagram of hole transitions between subbands in light amplification; b) shape and dimensions of the sample plus crystallographic directions and field orientations in the Voigt and Faraday configurations.

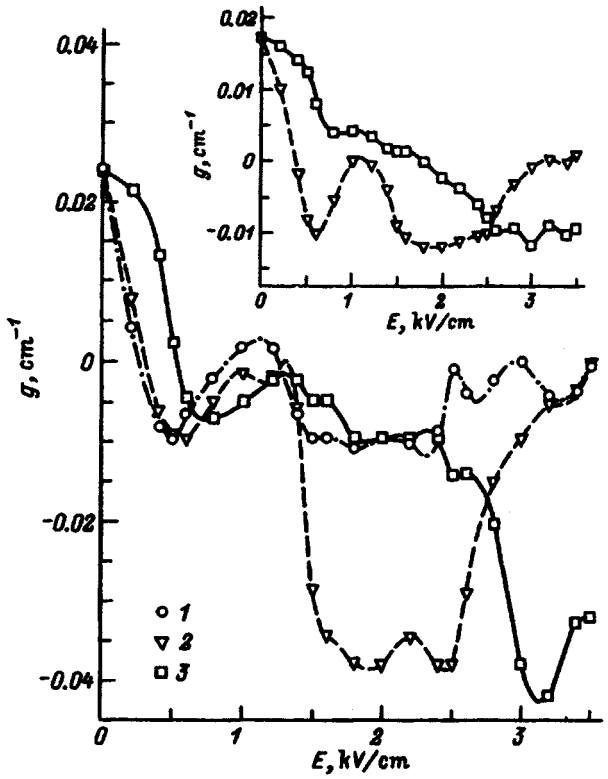

FIG. 2. Gain g (absorption coefficient for $g>0$) of unpolarized radiation versus electric field for a sample with hole density $N_p=2.5\times10^{14}$ cm^{-3} at $T=4.2$ K in the Faraday configuration. *1)* $B=0.6$ *T*; *2)* 1.5 *T*; *3)* 2 *T*. Inset: the same, but for a sample with hole density $N_p=6\times10^{13}$ cm^{-3}.

RESULTS AND DISCUSSION

The experimental results in the form of the electric field dependence of the gain at a wavelength of 92 μm in the Faraday and Voigt geometries are shown in Figs. 2–4.

The most notable observation is that the ratio of the gains for two samples with different densities is approximately equal to the density ratio (Fig. 2). For the Faraday configuration with $B=2$ T the amplification cross section attains values $\sigma_{\text{amp}}=-1.9\times10^{-16}$ cm^2 and -2×10^{-16} cm^2 for samples having high and low densities, respectively. It is evident from a comparison of Figs. 2 and 3 that the gain at the maximum of $|g|$ for the Voigt configuration is approximately three times higher than for the Faraday configuration. At $B=2.3$ T and $E=3.4$ kV/cm in the Voigt configuration g attains the value $g=-0.12$ cm^{-1} (or $\sigma_{\text{amp}}=-4.8\times10^{-16}$ cm^2).

The ranges of E and B in which lasing is possible have been determined previously[8] for a sample with $N_p\approx2.5\times10^{14}$ cm^{-3}. If we assume that lasing occurs for $|g|>0.02$ cm^{-1}, the bounds of the function $g(E)$ for this critical value of g correlate with the lasing ranges (a direct functional dependence does not exist, because the lasing wavelength shifts slightly as E and B are varied). The maximum of the $|g(E)|$ curve shifts toward higher values of E as B is increased, consistent with the calculated behavior. The ratio E/B is approximately equal to 1.5–1.7 kV/T·cm at the maximum. This means that in fields $\mathbf{E}\perp\mathbf{B}$ with $\mu_2B/c>1$ (μ_2 is the LH mobility) the radius vector of the center of the LH cyclotron paths $p_{B2}=m_2cE/B$ is 0.7–0.8 times the quantity $p_{02}/2$ (p_{02} is the LH momentum corresponding to the optical phonon energy $\varepsilon_{\text{ph}}=p_{02}^2/2m_2$). Consequently, the center of the LH paths lies inside the passive domain for LHs ($\varepsilon_2<\varepsilon_{\text{ph}}$), whereas the center of the HH paths for the same ratio $E/B=1.5$–1.7 $kV/T\cdot$cm is situated close to the boundary between the passive and active domains $\varepsilon_1=\varepsilon_{\text{ph}}$).

Figure 5 shows the results of calculations of the function $g(E)$ (1). According to Refs. 9–11,

$$\alpha_{21}=\frac{e^2}{\pi cm_0^2n\omega}\int_{\mathbf{k}}|\mathbf{e}_\omega\mathbf{p}_{21}|^2[f_2(\mathbf{k})-f_1(\mathbf{k})]\times\delta[\varepsilon_2(\mathbf{k})-\varepsilon_1(\mathbf{k})-\hbar\omega]d\mathbf{k}, \tag{3}$$

where m_0 is the free-electron mass, n is the refractive index, $f_2(\mathbf{k})$ and $f_1(\mathbf{k})$ are the distribution functions of light holes and heavy holes with respect to the momenta $\mathbf{p}=\hbar\mathbf{k}$ [for $f_2(\mathbf{k})>f_1(\mathbf{k})$ we have $\alpha_{21}<0$, and light amplification is also possible], which we assume to be biased Boltzmann distributions for simplification of the calculations, $\mathbf{e}_\omega$ is the unit vector in the direction of the electric field of the electromagnetic wave, and $\mathbf{p}_{21}$ is the matrix element of the momentum operator. The drift velocities, temperatures, and densities of heavy and light holes in the fields $\mathbf{E}\perp\mathbf{B}$ can be determined from the balance equations for the momentum, power, and number of particles (see Ref. 8 for a more detailed discussion).

The absorption coefficient α_{indir} for indirect transitions is determined using the second approximation of perturbation theory. Scattering by acoustic and optical phonons and impurities is taken into account. The results of calculations of g

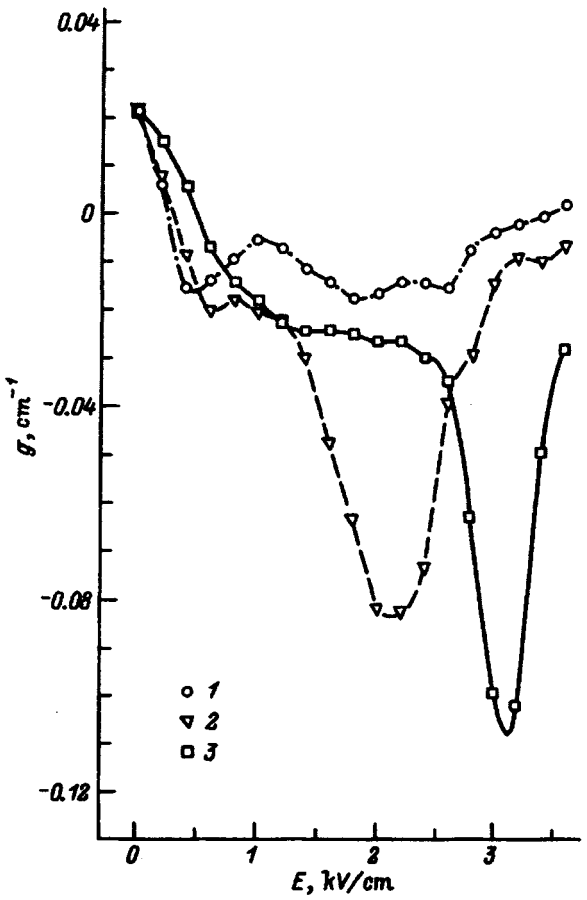

FIG. 3. Gain g (absorption coefficient for $g>0$) of polarized radiation ($\mathbf{e}_\omega \| \mathbf{B}$) versus electric field for a sample with hole density $N_p = 2.5\times 10^{14}$ cm^{-3} at $T = 4.2$ K in the Voigt configuration. *1*) $B = 0.6\ T$; *2*) 1.5 T; *3*) 2 T.

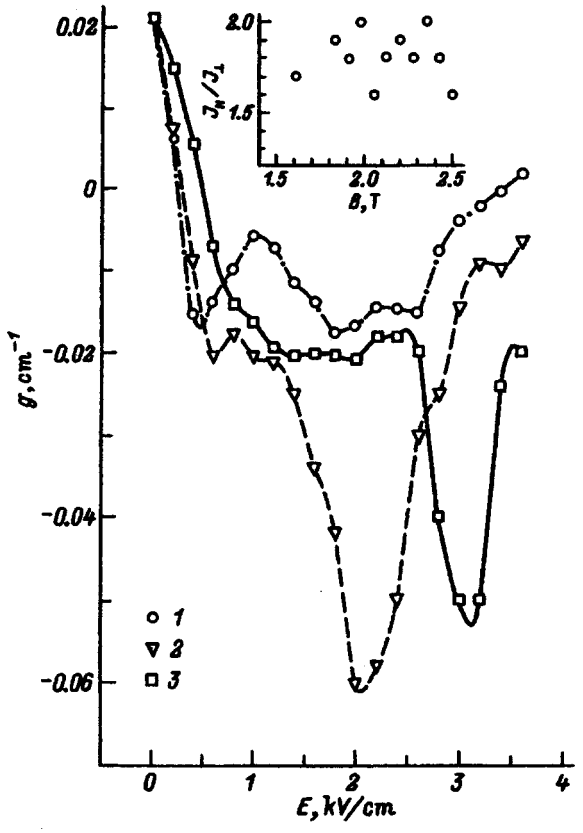

FIG. 4. The same as Fig. 3, but for the light polarization $\mathbf{e}_\omega \| \mathbf{E}$. Inset: intensity ratio of the laser beam versus magnetic field in the Voigt configuration for two polarizations: $J_\parallel$ ($\mathbf{e}_\omega \| \mathbf{B}$) and $J_\perp$ ($\mathbf{e}_\omega \| \mathbf{E}$), $E = 2.5$ kV/cm.

without anisotropy of the HH and LH distribution functions in an electric field are shown in Fig. 5. The points represents the results of calculations according to Eq. (3), with $f_1(\varepsilon)$ and $f_2(\varepsilon)$ determined experimentally. We note good agreement between the values of α_{21} determined using the patently crude approximation by a biased Boltzmann distribution function and the value obtained from the experimentally determined LH and HH distribution functions.

The calculated $g(E)$ curve is similar in form to the experimentally determined plot. The decrease in $|g|$ for large E is attributable to the increase in α_{indir} primarily due to intraband HH transitions with the emission of optical phonons. For this kind of light absorption the coefficient $\alpha_{\text{indir}} \sim \exp\{-(\varepsilon_{\text{ph}} - h\nu)/k_B T_1\}$ and increases rapidly with the temperature T_1, since $k_B T_1 \ll \varepsilon_{\text{ph}}$ in the pertinent ranges of the fields E and B (Ref. 8). In the low-field range $|g|$ is small by virtue of insufficient hole population inversion (i.e., a small value of $|\alpha_{21}|$).

It follows from a comparison of the data in Figs. 3 and 4 that the gain depends on the light polarization. The probability of direct $2 \to 1$ transitions is $w_{21} \sim \sin^2(\widehat{\mathbf{k}} \cdot \mathbf{e}_\omega)$ (Ref. 10). Consequently, if the HH and LH distribution functions are anisotropic (the hole drift velocity is comparable with the thermal velocity in a strong field at low temperatures), then w_{21} depends on the direction of $\mathbf{e}_\omega$ relative to the directions of **E** and **B**. An expression for the HH and LH drift momenta $\mathbf{p}_{dri}$ is given in Ref. 8. Moreover, for light-absorption processes involving phonons and impurities the main contribution is from intraband HH transitions. In this case $\alpha_{\text{indir}} \sim [\mathbf{e}_\omega \cdot (\mathbf{k}_f - \mathbf{k}_0)]^2$, where $\mathbf{k}_0$ and $\mathbf{k}_f$ are the initial and final hole states. After the emission of an optical phonon we have $\mathbf{k}_f \approx 0$ and $\alpha_{\text{indir}} \sim \mathbf{e}_\omega \cdot \mathbf{k}_0$, where $\hbar k_0 \approx p_{01}$ (p_{01} is the HH momentum corresponding to the optical phonon energy). In the case of almost-collisionless motion of HHs in the passive domain in fields $\mathbf{E} \perp \mathbf{B}$ the wave vector $\mathbf{k}_0$ is almost parallel to **E**, so that the absorption must be acutely anisotropic: for $\mathbf{e}_\omega \perp \mathbf{k}_0$ (or in the Voigt geometry $\mathbf{e}_\omega \| \mathbf{B}$) the coefficient α_{indir} must be smaller than for $\mathbf{e}_\omega \| \mathbf{k}_0$ (or $\mathbf{e}_\omega \| \mathbf{E}$). Similar anisotropy of light absorption by heavy holes in indirect transitions has been mentioned previously.[11] In our samples with impurity concentrations $N_I \equiv N_A + N_D \approx 5\times 10^{14}$ cm^{-3} (N_A and N_D are the densities of donors and acceptors) the motion of HHs in the passive domain is not collisionless. According to experimental data,[12,13] however, the anisotropy of the HH distribution function is quite pronounced.

The results of calculations of $g(h\nu)$, with allowance for the anisotropy of the LH and HH distribution functions, are shown in Fig. 6. It is evident that the main factor contributing to the anisotropy of g in the long-wavelength range is anisotropy of the light absorption coefficient α_{indir} for indirect transitions. Our calculations with simplified HH and LH distribution functions yield approximately the same results as

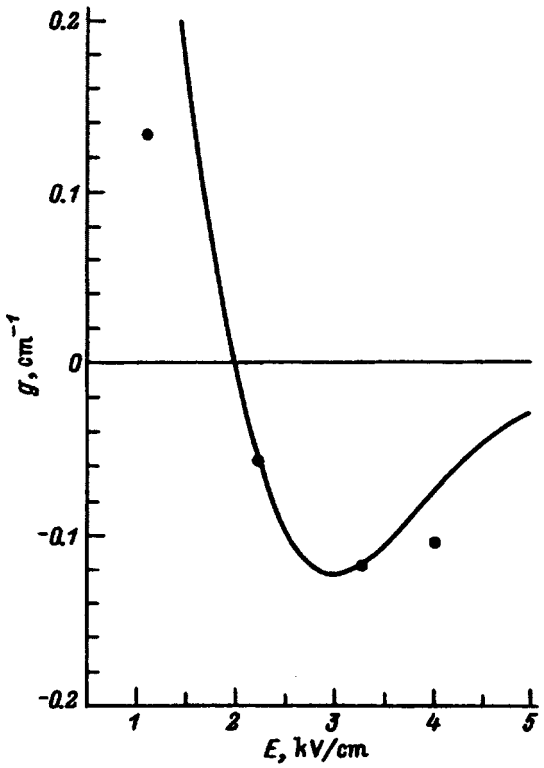

FIG. 5. Gain g (absorption coefficient for $g>0$) of unpolarized radiation having a wavelength $\lambda \approx 100\ \mu$m versus electric field. The solid curve is calculated for $T=42$. K, $N_p=2.5\times10^{14}$ cm^{-3}, $N_I=N_A+N_D=5\times10^{15}$ cm^{-3}, and $B=2.2$ T. The dots represent the values of g obtained using experimentally determined heavy-hole and light-hole distribution functions.

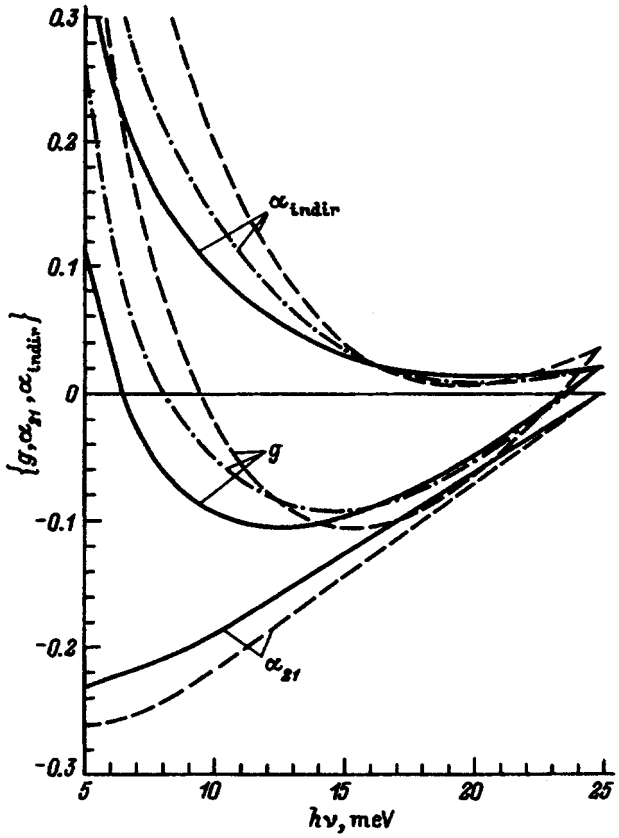

FIG. 6. Gain α_{21} (absorption coefficient for $\alpha_{21}>0$) of polarized light in direct hole transitions, absorption coefficient α_{indir} in indirect transitions, and gain $g=\alpha_{21}+\alpha_{\text{indir}}$ (absorption coefficient for $g>0$) versus photon energy. The calculations have been carried out for $T=4.2$ K, $N_p=2.5\times10^{14}$ cm^{-3}, $N_I=N_A+N_D=5\times10^{14}$ cm^{-3}, $B=2.2$ T, and $E=3.3$ kV/cm. The solid curves correspond to $\mathbf{e}_\omega\|\mathbf{B}$, the dashed curves to $\mathbf{e}_\omega\|\mathbf{E}$, and the dot-dash curves to $\mathbf{e}_\omega\|[\mathbf{E}\times\mathbf{B}]$.

calculations using anisotropic distribution functions found by the Monte Carlo method.[14]

It follows from the experimental data (Figs. 3 and 4) and from the calculations (Fig. 6) that the optical gain g for light with a wavelength in the vicinity of $\lambda=100\ \mu$m in the Voigt configuration with the polarization $\mathbf{e}_\omega\|\mathbf{B}$ is higher than for the polarization $\mathbf{e}_\omega\|\mathbf{E}$. Consequently, the intensity of emission of light with the two polarizations should be expected to differ, as has indeed been confirmed experimentally (see the inset to Fig. 4). In contrast with Ref. 6, for our samples in the Voigt configuration the intensity ratio between the two light polarization is greater than unity for all magnetic fields.

This work has received support from the Russian Fund for Fundamental Research (RFFI Grant 96-02-17404), jointly from RFFI and the International Association for the Promotion of Cooperation with Scientists from the Independent States of the Former Soviet Union (RFFI-INTAS Grant 00615), and from the State Committee for Science and Technology of the Russian Federation (GKNT RF Grant 1-093/4).

[1)]Actually the quantity g can be either negative or positive. We call g the gain for $g<0$ and the absorption coefficient for $g>0$.

[2)]Gain measurements have also been reported in Ref. 4 for the amplification of radiation having a wavelength in the vicinity of 300 μm by hot holes in germanium in crossed fields **E** and **B** in the Faraday geometry. There, however, amplification is associated with hot-hole transitions between Landau levels of light holes. This mechanism of amplification and lasing has been investigated earlier[1] and is not the object of the present investigation.

[1] Opt. Quantum Electron. **23**(2) (1991) (Special Issue on Far-Infrared Semiconductor Lasers).
[2] R. C. Strijbos, J. G. S. Lok, and W. T. Wenkenbach, J. Phys.: Condens. Matter **6**, 7461 (1994).
[3] S. Komiyama and S. Kuroda, Solid State Commun. **59**, 167 (1986).
[4] Yu. B. Vasil'ev and Yu. L. Ivanov, Pis'ma Zh. Tekh. Fiz. **12**, 250 (1986) [Sov. Tech. Phys. Lett. **12**, 103 (1986)].
[5] L. E. Vorobjev, S. N. Danilov, and V. I. Stafeev,Opt. Quantum Electron. **23**, S221 (1991).
[6] I. Hosako and S. Komiyama, Semicond. Sci. Technol. **7**, B645 (1992).
[7] L. E. Vorobjev, S. N. Danilov, D. V. Donetsky, D. Firsov, Yu. V. Kochegarov, and V. I. Stafeev, Semicond. Sci. Technol. **9**, 641 (1994).
[8] L. E. Vorob'ev, S. N. Danilov, Yu. V. Kochegarov, and D. A. Firsov, Fiz. Tekh. Poluprovodn. **31** (1997) (in press).
[9] E. O. Kane, J. Phys. Chem. Solids **1**, 82 (1956).
[10] A. H. Kahn, Phys. Rev. **97**, 1647 (1955).
[11] Yu. T. Rebane, Fiz. Tekh. Poluprovodn. **14**, 289 (1980) [Sov. Phys. Semicond. **14**, 169 (1980)].
[12] A. C. Baynham and W. Pinson, Phys. Rev. Lett. **11**, 268 (1963).
[13] L. E. Vorob'ev, Yu. K. Pozhela, A. S. Reklaĭtis, E. S. Smirnitskaya, V. I. Stafeev, and A. B. Fedortsov, Fiz. Tekh. Poluprovodn. **12**, 742 (1978) [Semiconductors **12**, 433 (1978)].
[14] E. V. Starikov and P. N. Shiktorov, Opt. Quantum Electron. **23**, S177 (1991).

Translated by James S. Wood